Node Generation on Surfaces and Bounds on Minimal Riesz Energy

By

Timothy Michaels

Dissertation

Submitted to the Faculty of the

Graduate School of Vanderbilt University

in partial fulfillment of the requirements

for the degree of

DOCTOR OF PHILOSOPHY

in

Mathematics

December 16, 2017

Nashville, Tennessee

Approved:

Ed Saff, Ph.D

Doug Hardin, Ph.D

Akram Aldroubi, Ph.D

Alex Powell, Ph.D

Eric Barth, Ph.D

To my mother and father, who taught me the joy of learning

ACKNOWLEDGMENTS

First and foremost I am grateful to my advisers Dr. Ed Saff and Dr. Doug Hardin for their guidance and support. They are giants in several fields of applied analysis as well as superb lecturers, and they have taught me much about how to be a mathematician. I hope to work with them on many projects in the future. I would also like to thank the other members of my committee, Dr. Akram Aldroubi, Dr. Alex Powell, and Dr. Eric Barth for their advice and encouragement the past few years. I am indebted to Dr. Natasha Flyer and Dr. Bengt Fornberg for their exceptional hospitality and a fruitful collaboration.

I am grateful to the department at Vanderbilt which has educated me in a great variety of mathematics. In particular I would like to thank Drs. Gieri Simonett, Larry Schumaker, Dietmar Bisch, and Brian Simenak for their wonderful classes. In addition, I would not have pursued mathematics in the first place without the inspirational teaching of Dr. Jim Conant and Mrs. Carolyn Lawhorn.

The graduate student community has made Vanderbilt a truly rewarding place to do mathematics. In no particular order I would like to thank Sandeepan Parekh, Alex Vlasiuk, Zach Gaslowitz, Kelly O'Connell, Ryan Solava, Corey Jones, Wes Camp, and Chang Hsin-Lee for their friendship and mathematical conversations.

I am also thankful for the gymnastics communities at Harpeth Gymnastics, the NAIGC, and the NGJA for their camaraderie and their support in many forms.

I would lastly like to thank my family without whom I would I would have accomplished nothing. My parents Dr. Robin Michaels and Dr. Tom Michaels have worked tirelessly to prepare and support me in all endeavors. My sister Amelia Michaels is a perpetual well of joy and inspiration and I am grateful for her boundless friendship. Finally, my adoptive family Rose Kennedy is a source of perspective and advice in all situations.

TABLE OF CONTENTS

Page

DEDICATION ii

ACKNOWLEDGMENTS iii

LIST OF TABLES vi

LIST OF FIGURES vii

1 INTRODUCTION 1

1.1 Distributing Points on a Sphere and in Space 1

1.2 Minimizing Energy as a Method of Point Distribution 4

1.3 Lattice Packings and $C_{s,d}$ 8

1.4 Organization and Results 11

2 POINT GENERATION ON $\mathbb{S}^2$ 13

2.1 Spiral Points 13

2.2 Low Discrepancy Nodes 20

2.3 Equal Area Partitions 21

2.4 Polyhedral Nodes and Area Preserving Maps 28

2.4.1 Equidistributed mesh icosahedral nodes 32

2.5 Nodes via Optimization 37

2.6 Random Points 40

2.7 Summary of Properties 41

2.8 A Riesz Energy Comparison 42

2.9 Proofs of Equidistribution and Mesh Ratios 44

3 NODE GENERATION ON OTHER MANIFOLDS 61

3.1 Torus Configurations 61

3.2 Configurations on $\mathbb{S}^3$ 64

3.3 Variable Density Node Generation in $\mathbb{R}^d$ 66
3.3.1 Radial basis functions 66
3.3.2 Choice of method 68
3.3.3 The algorithm 70
3.3.4 Sample applications 74
3.3.4.1 Spherical shell 74
3.3.4.2 Atmospheric node distribution using surface data 76
3.3.4.3 A pair of Gaussians 79
3.4 Concluding remarks 80
3.4.1 Separation distances of tiled irrational lattices 81
4 ASYMPTOTIC LINEAR PROGRAMMING BOUNDS FOR MINIMAL ENERGY NODES 84
4.1 Introduction 84
4.2 Linear Programming Bounds 87
4.2.1 Levenshtein $1/N$ quadrature rules 92
4.3 Proofs of Theorems 4.1.3, 4.1.4, and 4.1.6 99
4.4 Numerics 109
BIBLIOGRAPHY 114

LIST OF TABLES

Table Page

2.1 Mesh Ratios for Generalized Spiral Nodes 15
2.2 Mesh Ratios for Fibonacci Nodes 19
2.3 Mesh Ratios for Zonal Equal Area Nodes 25
2.4 Mesh Ratios for HEALPix nodes 27
2.5 Mesh Ratios for Radial Icosahedral Nodes 29
2.6 Mesh Ratios for Cubed Sphere Points 30
2.7 Mesh Ratios for Octahedral Nodes 32
2.8 Mesh Ratios for Coulomb and Log Energy Points 39
2.9 Mesh Ratios for Maximal Determinant Nodes 40
2.10 Summary of Point Set Properties 41
2.11 Comparison of Separation and Mesh Ratio Constants 42

4.1 Upper Bounds on B_d 110

LIST OF FIGURES

Figure Page

1.1 Approximately minimal energy nodes on $\mathbb{S}^2$ for $N = 1000$ and $s = 2$. 8

2.1 Plot of $N = 700$ generalized spiral points and their Voronoi decomposition. 14

2.2 Fibonacci nodes for $N = 1001$ and corresponding Voronoi decomposition. . 16

2.3 Irrational lattice points on the square with labeled basis vectors. 17

2.4 Triangulation of $N = 3001$ Fibonacci nodes. 18

2.5 Hammersley nodes for $N = 1000$ and corresponding Voronoi decomposition. 20

2.6 Zonal equal area partition of the sphere into 100 cells. 23

2.7 Zonal equal area points for $N = 700$ and corresponding Voronoi decomposition. 24

2.8 Base tessellation of the sphere into 12 equal area pixels. 26

2.9 HEALPix nodes and Voronoi decomposition for $N = 1200$, $k = 10$. 26

2.10 Radial icosahedral nodes $N = 642$. 28

2.11 Plot of $N = 1016$ cubed sphere points and Voronoi decomposition. 29

2.12 Equal area octahedral points for $k = 15$ and $N = 902$. 31

2.13 Planar icosahedral mesh for $(m,n) = (5,4)$. 33

2.14 Illustration of area preserving map Φ defined piecewise on each triangle bounded by two altitudes of an icosahedral face. 34

2.15 Equidistributed mesh icosahedral nodes for $(m,n) = (7,2)$. 35

2.16 Plot of mesh ratios for radial and equidistributed icosahedral nodes sampled along the subsequences $(m,0)$ and (m,m). 36

2.17 Coulomb points (top) and log energy points (bottom) and their Voronoi decomposition for $N = 1024$. 37

2.18 Maximal determinant nodes for $N = 961$. 38

2.19 Random points for $N = 700$ and their Voronoi decomposition. 40

2.20 Comparison of Riesz energies in the hypersingular case 43
2.21 Limiting form of Voronoi cell for each $x_i \in K_h \cap \omega_N$. 47

3.1 6765 equidistributed Fibonacci torus nodes 62
3.2 The vertices which the algorithm tests to be in the density support. 73
3.3 Left: Distribution of radii of the spherical shell node set. Right: Ratios of expected separation to nearest neighbor distances. 75
3.4 Left: a general view of a uniform node distribution in an atmospheric-like shell. Right: zoomed in Americas. 77
3.5 A fragment of the Western coast of South America. The nodes on the right are color-coded using heights. 78
3.6 The effects of the repel procedure and hole radii. Left: distribution of the nearest-neighbor distances in the atmospheric node set, before (blue) and after (red) executing the repel subroutine. Right: distribution of distances to the 12 nearest neighbors for the whole configuration (color only), for the surface subset (contours), the hole radii (black dashed contour). 78
3.7 Distribution of distances to the 12 nearest neighbors for the atmospheric node configuration. Left: the surface subset. Right: the whole set. Scales are the same in both subplots. 79
3.8 Left: the node set from Section 3.3.4.3. Right: distribution of the nearest neighbor distances, before (blue) and after (red) executing the repel subroutine. 80
3.9 Ratios of the values of radial density function ρ to nearest neighbor distance, evaluated for the node set from Section 3.3.4.3. 81
3.10 Dependence of the separation distance of the 3-dimensional lattice on the number of nodes in a single cube. 82

4.1 Graphs of $f(s) = (\widetilde{C}_{s,d}/A_{s,d})^{1/s}$ for $d = 2, 4, 8$ and 24. 111
4.2 Graph of $g(s) = (\widetilde{C}_{s,d}/\max\left\{\Theta_{s,d}, \xi_{s,d}\right\})^{1/s}$ for $d = 2$, $3 \leq s \leq 50$. 112

CHAPTER 1

INTRODUCTION

1.1 Distributing Points on a Sphere and in Space

Point generation on a manifold is a far reaching subject throughout the mathematical and physical sciences. In representing a manifold as a discrete configuration for data storage, network and sensor development, modeling functions with finite element or radial basis function methods, approximating integrals using quasi-Monte Carlo methods, statistical sampling, graphic design, molecular modeling, or determining ground states of matter, good node sets need to be constructed with certain properties and constraints. Of particular interest is point generation on the unit sphere,

$$\mathbb{S}^d := \left\{ x \in \mathbb{R}^{d+1} | \|x\| = 1 \right\}$$

where $\|\cdot\|$ denotes the standard Euclidean norm. Modeling of the Earth, night sky, or the cosmic microwave background radiation often requires large and computationally efficient data sets on $\mathbb{S}^2$. Sampling on higher dimensional spheres is intimately related to error correcting codes and communication theory.

In distributing points (nodes), we must consider the question, "What makes a good node set?" One criterion is that they model a given distribution on the manifold. On a d-dimensional, compact Riemannian manifold $A \subset \mathbb{R}^n$, a sequence $\{\omega_N\}_{N=1}^{\infty} \subset A$ of point sets with ω_N having cardinality N is called *equidistributed* if the sequence of normalized counting measures,

$$\nu_N(B) := \frac{1}{N}|B \cap \omega_N|, \qquad B \text{ a Borel set}, \tag{1.1}$$

associated with the ω_N's converges in the weak-star sense to $\sigma_A := \mathcal{H}_d(\cdot \cap A)/\mathcal{H}_d(A)$, the normalized d-dimensional Hausdorff measure on A, as $N \to \infty$. That is, for all continuous

functions $f : A \to \mathbb{R}$,

$$\lim_{N\to\infty} \int_A f \, \mathrm{d}\nu_N = \int_A f \, \mathrm{d}\sigma_A.$$

An equivalent definition is that the discrepancy

$$D(\omega_N) := \sup_{x\in A,\ r>0} \left| \frac{|B(x,r) \cap \omega_N|}{N} - \sigma_A(B(x,r)) \right| \to 0, \qquad N \to \infty,$$

where $B(x,r)$ denotes the ball of radius r around x. Finding low discrepancy sequences is of particular importance in quasi-Monte Carlo methods. Further challenges arise when we wish to place nodes according to a certain non-uniform density, as a method of local refinement, for example, or along the boundary of A or when we deal with non-smooth manifolds. When using meshless methods for solving PDE's, the desired distribution is often non-uniform, in which case we can replace σ_A with a general probability measure μ on A and measure equidistribution and discrepancy with respect to μ.

For the study of local statistics, separation and covering properties play an important role. The *separation* of a configuration $\omega_N \subset A$ is

$$\delta(\omega_N) := \min_{\substack{x,y\in\omega_N \\ x\neq y}} \|x-y\|,$$

and a sequence of N-point configurations is said to be *well-separated* if for some $c > 0$ and all $N \geq 2$,

$$\delta(\omega_N) \geq cN^{-1/d}. \tag{1.2}$$

The *covering radius* of ω_N with respect to A is defined to be

$$\eta(\omega_N) := \max_{y\in A} \min_{x\in\omega_N} \|x-y\|,$$

and a sequence of N-point configurations is a *good-covering* if for some $C > 0$ and all $N \geq 2$,

$$\eta(\omega_N) \leq CN^{-1/d}. \tag{1.3}$$

A sequence of configurations $\{\omega_N\}_{N=2}^{\infty}$ is said to be *quasi-uniform* if the sequence

$$\left\{\gamma(\omega_N) := \frac{\eta(\omega_N)}{\delta(\omega_N)}\right\}_{N\geq 2}$$

is bounded as $N \to \infty$. The quantity $\gamma(\omega_N)$ is called the *mesh ratio* of ω_N. Note that some authors define the mesh ratio as $2\gamma(\omega_N)$. A sequence of N-point configurations is quasi-uniform if it is well-separated and a good-covering. We remark that equidistribution does not imply quasi-uniformity or vice versa. In applications involving radial basis functions, "1-bit" sensing, and finite element methods ([50], [72], [85], and [95]), there is interest in precise bounds on $D(\omega_N)$, $\delta(\omega_N), \eta(\omega_N)$, and $\gamma(\omega_N)$. A trivial lower bound is $\gamma(\omega_N) \geq 1/2$ for any configuration. Asymptotically, as proved in [12], for any sequence of configurations $\{\omega_N\}_{N=2}^{\infty} \subset \mathbb{S}^2$

$$\gamma(\omega_N) \geq \frac{1}{2\cos \pi/5} + o(1) = \frac{\sqrt{5}-1}{2} + o(1), \quad N \to \infty,$$

Part of our emphasis in discussing equidistributed configurations on $\mathbb{S}^2$ in Chapter 2 will be on generating sequences with low mesh ratio.

Yet another property advantageous to certain sequences is that they are approximately optimal configurations with regards to some quantity. The best packing problem, known as the Tammes problem when $A = \mathbb{S}^2$, asks for the largest separation distance possible for a given N-point configuration on A, i.e. determine

$$\delta(N,A) := \sup_{\omega_N \subset A} \delta(\omega_N). \tag{1.4}$$

In information theory [88], error correcting codes on the sphere are engineered by finding nodes which are near optimal packing configurations. On the other hand, the best covering problem asks for the minimal covering radius achieved by an N-point configuration, that is

$$\eta(N,A) := \inf_{\omega_N \subset A} \eta(\omega_N). \tag{1.5}$$

The *Voronoi cell* of a point $x \in \omega_N \subset A$ is the polytope

$$V_x(\omega_N) := \{y \in A : \ \|y-x\| \leq \|y-z\|, \forall\, z \in \omega_N \setminus \{x\}\}. \tag{1.6}$$

The *Voronoi decomposition* of a configuration is

$$V(\omega_N) := \{V_x(\omega_N)\}_{x\in\omega_N}$$

which partitions A. In this context, the best packing problem asks for the Voronoi decomposition with the largest possible minimal inradius of a cell while the best covering problem asks for the smallest possible maximal circumradius of a cell. However, solutions to the best packing problem are only known for a handful of manifolds A and points N. On the sphere $\mathbb{S}^2$, the only optimal packings known are for $N = 2, 3, \ldots 14$, and 24. We can instead generalize the packing problem by asking for a suitable pairwise potential whose minimal configurations are close to best packing points. This is of particular interest for this thesis.

1.2 Minimizing Energy as a Method of Point Distribution

The problem of minimizing point energies on the sphere dates to at least the beginning of the 20$^{\text{th}}$ century when Thomson put forth a model of the ground state configurations of electrons in [100]. Given a lower-semicontinuous, symmetric kernel $K : A \times A \to (-\infty, \infty]$, and a configuration $\omega_N \subset A$, the K-energy of ω_N is defined to be

$$\mathrm{E}_K(\omega_N) := \sum_{\substack{x,y\in\omega_N \\ x\neq y}} K(x,y). \tag{1.7}$$

If A is compact, the infimum of $\mathrm{E}_K(\omega_N)$ over all N-point configurations is attained and is denoted by $\mathcal{E}_K(N,A)$. We will restrict our attention to the class of Riesz kernels defined by

$$
\begin{aligned}
K_s(x,y) &= \frac{1}{\|x-y\|^s}, \qquad s>0 \\
K_{\log}(x,y) &= \log\frac{1}{\|x-y\|}, \\
K_s(x,y) &= -\|x-y\|^{-s}, \qquad s<0.
\end{aligned} \tag{1.8}
$$

For brevity, the energy and minimal energy quantities for the Riesz s-kernel and log kernel will be denoted by $\mathrm{E}_s(\omega_N)$, $\mathrm{E}_{\log}(\omega_N)$, $\mathcal{E}_s(N,A)$, and $\mathcal{E}_{\log}(N,A)$ respectively. The latter two quantities are related by

$$
\frac{\mathrm{d}}{\mathrm{d}s}\mathcal{E}_s(N,A)\bigg|_{s\to 0^+} = \mathcal{E}_{\log}(N,A),
$$

On the other hand, as $s\to\infty$, the energy in (1.7) is dominated by the terms which represent the smallest pairwise distances, and in this sense the minimal energy problem becomes the best-packing problem. More precisely [13]:

Proposition 1.2.1. *For a fixed $N\geq 2$ and any $A\subset\mathbb{R}^d$,*

$$
\lim_{s\to\infty}\mathcal{E}_s(N,A)^{1/s} = \frac{1}{\delta(N,A)}. \tag{1.9}
$$

Proof. Denote by $\omega_N^s=\{x_1^s,\dots x_N^s\}$ an N-point s-energy minimizing configuration on A and $\omega_N^\infty=\{x_1^\infty,\dots x_N^\infty\}$ an N-point best packing. Then

$$
\mathcal{E}_s(N,A)^{1/s} = E_s(\omega_N^s)^{1/s} \geq \frac{1}{\delta(\omega_N^s)} \geq \frac{1}{\delta(N,A)}
$$

by discarding all but the largest term in (1.7). On the other hand,

$$
\mathcal{E}_s(A,N)^{1/s} \leq E_s(\omega_N^\infty)^{1/s} = \frac{1}{\delta(N,A)}\left(\sum_{i\neq j}\left(\frac{\delta(N,A)}{\|x_i^\infty-x_j^\infty\|}\right)^s\right)^{1/s} \leq \frac{1}{\delta(N,A)}(N(N-1))^{1/s},
$$

and thus

$$\limsup_{s\to\infty} \mathcal{E}_s(A,N)^{1/s} \leq \frac{1}{\delta(N,A)}.$$

□

Determining an exact minimal configuration for a fixed N and s is a highly nonlinear optimization problem complicated by the fact that the number of local minima appears to grow exponentially with N. In practice, gradient descent and Newton methods are used to arrive at approximate global minima [27]; however, there is substantial interest in generating nearly optimal points more quickly. Smale's 7$^{\text{th}}$ problem for the 21$^{\text{st}}$ century asks for an algorithm in polynomial time to generate N-point configurations $\omega_N \subset \mathbb{S}^2$ such that

$$E_{\log}(\omega_N) \leq \mathcal{E}_{\log}(N,\mathbb{S}^2) + c\log N.$$

for some constant c independent of N [90]. While a long way from a solution to Smale's problem, several fast algorithms for generating equidistributed points on $\mathbb{S}^2$ have been put forth and are analyzed in Chapter 2.

A solution to Smale's problem requires an asymptotic expansion of $\mathcal{E}_{\log}(N,\mathbb{S}^2)$ to order $\log N$. As $N\to\infty$, minimal energy configurations will approximate some distribution on A. We define the *continuous Riesz energy* for a probability measure μ on A by

$$\mathcal{I}_s[\mu] := \int\int \frac{1}{|\mathbf{x}-\mathbf{y}|^s} \mathrm{d}\mu(\mathbf{x})\mathrm{d}\mu(\mathbf{y}), \qquad s\neq 0$$

$$\mathcal{I}_{\log}[\mu] := \int\int \log\frac{1}{|\mathbf{x}-\mathbf{y}|} \mathrm{d}\mu(\mathbf{x})\mathrm{d}\mu(\mathbf{y}).$$

For a d-dimensional set A, when $s<d$ and $s=\log$, $\mathcal{I}_s[\mu]$ is minimized by a unique probability measure, denoted $\mu_{A,s}$, called the *equilibrium measure* which is in general non uniform. As $N\to\infty$, the counting measures of the s-energy minimizing configurations

converge in the weak-star sense to $\mu_{A,s}$, and moreover, classical potential theory gives

$$\lim_{N\to\infty} \frac{\mathcal{E}_s(N,A)}{N^2} = \mathcal{I}_s[\mu_{A,s}]. \tag{1.10}$$

Furthermore, the following expansion is known [7] for log energy on $\mathbb{S}^2$:

Theorem 1.2.2. *There exists a constant $C \neq 0$, independent of N, such that*

$$\mathcal{E}_{\log}(N,\mathbb{S}^2) = \mathcal{I}_{\log}[\sigma_{\mathbb{S}^2}]N^2 - \frac{N\log N}{2} + CN + o(N), \qquad N\to\infty,$$

$$-0.22553754 \leq C \leq \widehat{C} := 2\log 2 + \frac{1}{2}\log\frac{2}{3} + 3\log\frac{\sqrt{\pi}}{\Gamma(1/3)} = -0.05560530...$$

The following extension of Theorem 1.2.2 is conjectured in [21]:

Conjecture 1.2.3.

$$\mathcal{E}_{\log}(N,\mathbb{S}^2) = \mathcal{I}_{\log}[\sigma_{\mathbb{S}^2}]N^2 - \frac{N\log N}{2} + \widehat{C}N + D\log N + O(1), \qquad N\to\infty.$$

When s is larger than the dimension of the set, which we call the *hypersingular* case, $\mathcal{I}_s[\mu] = \infty$ for any probability measure μ. Thus the continuous energy problem on A is ill-posed, and the standard methods of potential theory do not apply. In this case local interactions dominate the energy sum, and the authors in [57] proved that the resulting distribution is not dependent on the underlying set A for a large class of sets.

Theorem 1.2.4 ("Poppy Seed Bagel Theorem")**.** *Let $A \subset \mathbb{R}^p$ be the Lipschitz image of a bounded set in $\mathbb{R}^d$. For all $s > d$, there exists a constant $C_{s,d}$, independent of A such that*

$$\lim_{N\to\infty} \frac{\mathcal{E}_s(A,N)}{N^{1+s/d}} = \frac{C_{s,d}}{\mathcal{H}_d(A)^{s/d}}. \tag{1.11}$$

Moreover, any sequence of minimal s-energy configurations is equidistributed.

In dimension $d = 1$, it is known that $C_{s,1} = 2\zeta(s)$, twice the Riemann zeta function [71],

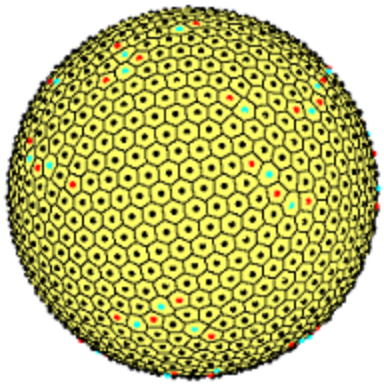

Figure 1.1: Approximately minimal energy nodes on $\mathbb{S}^2$ for $N = 1000$ and $s = 2$.

but for all other dimensions the exact value of $C_{s,d}$ remains an open question. Heuristically, minimal energy configurations in this regime appear to locally resemble best packing configurations. For example, on $\mathbb{S}^2$, it has been observed that the Voronoi cell decomposition of approximately optimal energy points appears to consist primarily of nearly regular spherical hexagons mixed with "scars" of spherical heptagons and pentagons as shown in Figure 1.1. Cells with black points are hexagonal, but not necessarily regular. Cells with red points are pentagonal and cells with cyan points are heptagonal. We discuss this formally in the next section.

1.3 Lattice Packings and $C_{s,d}$

The *density* of a collection $\mathcal{B}$ of non overlapping equal sized balls in $\mathbb{R}^d$ is defined to be:

$$\rho(\mathcal{B}) := \lim_{r\to\infty} \frac{\mathcal{H}_d(\mathcal{B}\cap[-r,r]^d)}{(2r)^d} \tag{1.12}$$

provided the limit exists. The *packing density* of $\mathbb{R}^d$ is then

$$\Delta_d := \sup_{\mathcal{B}} \rho(\mathcal{B}). \tag{1.13}$$

Like the packing problem for a finite number of points on a compact set A, determining the packing density is a notoroiusly difficult problem. The only dimensions for which Δ_d is known are $d = 1,2,3$ and more recently $d = 8$ and $d = 24$ (see [101] and [33]). In these dimensions, Δ_d is obtained by packings where the centers of the balls in $\mathcal{B}$ are given by a lattice which is a set of the form

$$\Lambda = \{A \cdot x \mid x \in \mathbb{Z}^d\} \tag{1.14}$$

for some $d \times d$ generator matrix A. The *covolume* of the lattice $|\Lambda|$ is defined to be $\mathrm{Det}(A)$. For $d = 1$, the integer lattice shows that $\Delta_1 = 1$. For $d = 2$ the triangular lattice which is given by the basis vectors $e_1 = (1,0)$ and $e_2 = (1/2, \sqrt{3}/2)$ was shown to be optimal by Fejes-Toth [45]. In dimension 3, there are uncountably many non isometric packings which produce a density of $\pi/3\sqrt{2}$ which are constructed by taking alternating layers of the triangular lattice. The face centered cubic lattice given by the generator matrix

$$A = \begin{bmatrix} -1 & -1 & 0 \\ 1 & -1 & 0 \\ 0 & 1 & -1 \end{bmatrix}$$

is one such construction. Proving that this is the optimal packing density is known as Kepler's conjecture and was an open problem for nearly 400 years until a massive computer aided proof was given by Hales [54].

The E_8 lattice is the unique even unimodular lattice in dimension 8. That is, its generator matrix has determinant 1 and the squared norm of every vector is an even integer. It consists of all vectors $v = \{x_1, \ldots, x_8\}$ such that

$$\text{all} \quad x_i \in \mathbb{Z} \qquad \text{or all} \quad x_i \in \mathbb{Z} + 1/2, \quad \text{and}$$

$$\sum x_i \equiv 0 \pmod 2.$$

The Leech lattice is the unique even unimodular lattice in dimension 24 with minimal norm 2. Multiple constructions are given in [36]. Both the E_8 and Leech lattices have a number of remarkable properties that make them solutions to other optimization problems [36].

In $d = 4$, the D_4 lattice, also known as the "checkerboard" lattice is conjectured to have optimal packing density. It is defined by

$$D_4 := \{\{x_1, \ldots, x_4\} \in \mathbb{Z}^4 \mid \sum x_i \equiv 0 \pmod 2\} \tag{1.15}$$

In general it is not true that Δ_d can be obtained by a lattice packing, and in large dimensions disordered packings appear to beat lattice packings [32].

The proofs of Δ_8 and Δ_{24} utilize the linear programming techniques developed in [32] for bounding sphere packings. These methods have been successfully used in a number of optimization problems to bound spherical designs [41] and error-correcting codes [40]. In chapter 4, we will adapt this technique to obtain lower bounds on $C_{s,d}$. The following relation between $C_{s,d}$ and the packing density is shown in [14]:

$$\lim_{s\to\infty} [C_{s,d}]^{1/s} = \frac{1}{C_{\infty,d}} \qquad C_{\infty,d} := 2\left[\frac{\Delta_d}{\mathcal{H}_d(\mathbb{B}^d)}\right]^{1/d} \tag{1.16}$$

where $\mathbb{B}^d \subset \mathbb{R}^d$ is the unit ball.

Any sequence of configurations on a set A provides an upper bound for $C_{s,d}$, as does any lattice $\Lambda \subset \mathbb{R}^d$. The *Epstein zeta function* for a lattice is defined to be

$$\zeta_\Lambda(s) := \sum_{0 \neq x \in \Lambda} \|x\|^{-s} \tag{1.17}$$

Then we have the following bound [21].

Proposition 1.3.1.

$$C_{s,d} \leq \min_{\Lambda \subset \mathbb{R}^d} |\Lambda|^{s/d} \zeta_\Lambda(s), \tag{1.18}$$

where the minimum is taken over all lattices $\Lambda \subset \mathbb{R}^d$ with covolume $|\Lambda| > 0$.

Proof. Fix $\Lambda \subset \mathbb{R}^d$ with $|\Lambda| > 0$, and let Ω be the fundamental cell of Λ, that is, if e_i, $i = 1, \ldots, d$ are the columns of the generator matrix A,

$$\Omega := \{\sum t_i e_i \mid 0 \leq t_i \leq 1\}.$$

For an $n \in \mathbb{N}$, consider the configuration ω_N which is the scaled lattice $(1/n)\Lambda$ intersected with Ω. Then $N = n^d$, and

$$\begin{aligned} E_s(\omega_N) = \sum_{x \in \omega_N} \sum_{\substack{x \neq y \\ y \in \omega_N}} \frac{1}{\|x-y\|^s} &\leq \sum_{x \in \omega_N} \sum_{\substack{x \neq y \\ y \in (1/n)\Lambda}} \frac{1}{\|x-y\|^s} \\ &= \sum_{x \in \omega_N} n^s \zeta_\Lambda(s) = n^{d+s} \zeta_\Lambda(s) = N^{1+s/d} \zeta_\Lambda(s). \end{aligned}$$

Substituting into (1.11) with $A = \Omega$ yields (1.18). □

Furthermore, the following conjecture is well known [21]:

Conjecture 1.3.2. *For $d = 2, 4, 8,$ and 24,*

$$C_{s,d} = \widetilde{C}_{s,d} := |\Lambda_d|^{s/d} \zeta_{\Lambda_d}(s)$$

where Λ_2 is the hexagonal lattice, Λ_4 the D_4 lattice, Λ_8 the E_8 lattice, and Λ_{24} the Leech lattice.

1.4 Organization and Results

This thesis has two principal foci. In Chapters 2 and 3 we present and analyze a variety of algorithms for generating point configurations on $\mathbb{S}^d$ and the torus $\mathbb{T} \subset \mathbb{R}^3$, as well introduce a generic strategy for generating locally quasi-uniform points of variable density on any full dimensional subset of $\mathbb{R}^d$. The methods and algorithms are concentrated on construction

and computation, though we also prove some of the theoretical properties above. With the notable exception of the variable density points, we do not discuss particular applications. We define and prove any necessary theorems as needed. Updated Matlab code for the algorithms presented is available at the author's Github: *https://github.com/michaetj*

In chapter 4, we prove a lower bound on $C_{s,d}$ based off of the linear programming method. This general framework for obtaining lower bounds for minimal energy configurations on the sphere $\mathbb{S}^d$ was developed by Yudin [106] based on the Delsart-Goethals-Seidel bounds on spherical designs [41]. The technique involves maximizing a function $f(t) \leq h(t)$ over certain constraints. Combining these methods with Levenshtein's work on maximal spherical codes, the authors in [20] establish explicit universal lower bounds depending only on the potential function h for absolutely monotone potentials, and we extend this to the asymptotic case as $N \to \infty$. The prerequisite theory is developed at the beginning of the chapter.

CHAPTER 2

POINT GENERATION ON $\mathbb{S}^2$

This chapter is based on the papers [56] and [73]. We survey some of the popular point configurations on the sphere $\mathbb{S}^2$, and prove results about their equidistribution, separation and mesh ratios. In Section 2.4.1, we introduce a new series of equidistributed icosahedral configurations, which improves on the best known mesh ratios and energies for some potentials. The proofs are collected at the end of the chapter.

2.1 Spiral Points

Generalized Spiral Points

A spherical spiral on $\mathbb{S}^2$ is a path in spherical coordinates of the form

$$r = 1, \quad \theta = L\phi, \quad 0 \leq \phi \leq \pi,$$

where ϕ denotes the polar angle and θ the azimuth. Modifying a construction by Rakhmanov, Saff, and Zhou [81], Bauer [4] defines a sequence of N points lying on a generating spherical spiral, S_N:

$$L = \sqrt{N\pi}, \quad h_k = 1 - \frac{2k-1}{N}, \quad \phi_k = \cos^{-1}(h_k), \quad \theta_k = L\phi_k, \quad k = 1, ..., N. \tag{2.1}$$

The slope L is chosen such that for large N, the distance between adjacent points on the same level of the curve is similar to the distance between adjacent levels which differ by 2π in θ. Indeed, the geodesic spacing between turns of the spiral is given by $2\pi/L = \sqrt{4\pi/N}$. Meanwhile, the total arc length is

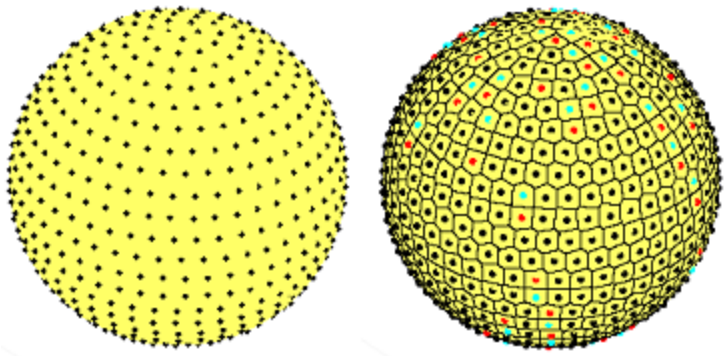

Figure 2.1: Plot of $N = 700$ generalized spiral points and their Voronoi decomposition.

$$T = \int_{S_N} \sqrt{d\phi^2 + d\theta^2 \sin^2\phi} = \int_0^{\pi} \sqrt{1 + L^2 \sin^2\phi}\, d\phi = 2\sqrt{1+L^2}\,\mathrm{E}\big(L/\sqrt{1+L^2}\big),$$

where $\mathrm{E}(\cdot)$ is the complete elliptic integral of the second kind. For large N, $T \approx 2L$, and the spiral is divided into nearly equal length segments of approximately $2L/N = \sqrt{4\pi/N}$. We refer to these points as the *generalized spiral points*.

Theorem 2.1.1. *The sequence $\{\omega_N\}_{N=1}^{\infty}$ of generalized spiral point configurations is equidistributed on $\mathbb{S}^2$, quasi-uniform, and has the following asymptotic separation property:*

$$\lim_{N\to\infty} \sqrt{N}\delta(\omega_N) = \sqrt{8 - 4\sqrt{3}\cos(\sqrt{2\pi}(1-\sqrt{3}))} = 3.131948.... \tag{2.2}$$

As shown in the proof of Theorem 2.1.1, the Voronoi cells of ω_n are asymptotically equal area (defined in (2.15) below), but do not approach regular hexagons. Indeed, a typical decomposition is shown in Figure 2.1. A comparison of the mesh ratios for several values of N is shown in Table 2.1. Numerically, the mesh ratio appears to converge to 0.8099....

Fibonacci Nodes

Another set of spiral points is modeled after nodes appearing in nature such as the seed

Table 2.1: Mesh Ratios for Generalized Spiral Nodes

N	$\gamma(\omega_N)$	N	$\gamma(\omega_N)$	N	$\gamma(\omega_N)$
10	0.897131	400	0.816007	20000	0.809510
20	0.827821	500	0.810128	30000	0.809629
30	0.814383	1000	0.805465	40000	0.809689
40	0.826281	2000	0.806411	50000	0.809725
50	0.834799	3000	0.807510	100000	0.809797
100	0.803901	4000	0.808077	200000	0.809832
200	0.806020	5000	0.808435	300000	0.809844
300	0.809226	10000	0.809151	500000	0.809854

distribution on the head of a sunflower or a pine cone, a phenomenon known as spiral phyllotaxis [42]. Coxeter [37] demonstrated these arrangements are fundamentally related to the Fibonacci sequence, $\{F_k\} = \{1,1,2,3,5,8,13,...\}$ and the golden ratio $\varphi = (1+\sqrt{5})/2$. There are two similar definitions of the spherical point set in the literature. Both are defined as lattices on the square $[0,1)^2$ and then mapped to the sphere by the Lambert cylindrical equal area projection, denoted by Λ. In Cartesian coordinates, Λ is defined by

$$\Lambda(x,y) := \left(\sqrt{1-(2y-1)^2}\cos 2\pi x, \sqrt{1-(2y-1)^2}\sin 2\pi x, 2y-1\right) \tag{2.3}$$

and, in spherical coordinates, by

$$\Lambda(x,y) := (\cos^{-1}(2y-1), 2\pi x) = (\phi,\theta). \tag{2.4}$$

Define a rational lattice on $[0,1)^2$, with total points F_k by

$$\widetilde{\omega}_{F_k} := \left(\left\{\frac{iF_{k-1}}{F_k}\right\}, \frac{i}{F_k}\right), \quad 0 \le i \le F_k, \tag{2.5}$$

where $\{x\} = x - \lfloor x \rfloor$ denotes the fractional part of x. On the other hand, an irrational lattice can be formed similarly for all values of total points N by replacing F_{k-1}/F_k in (2.5) by $\lim_{k\to\infty} F_{k-1}/F_k = \varphi^{-1}$:

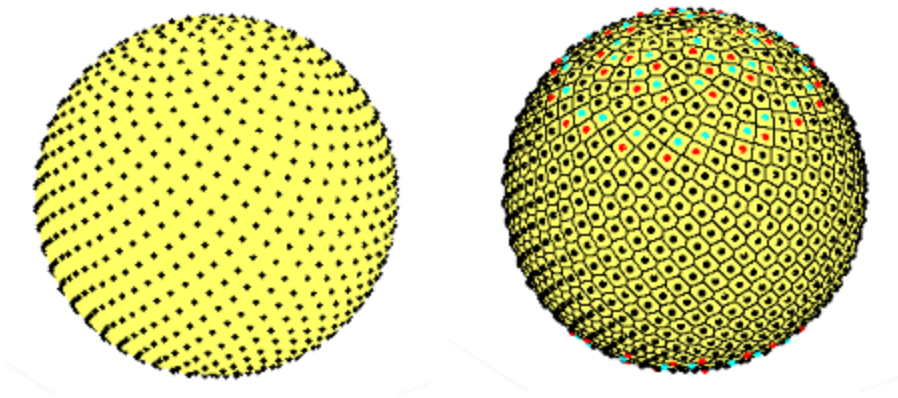

Figure 2.2: Fibonacci nodes for $N = 1001$ and corresponding Voronoi decomposition.

$$\widetilde{\omega}_N := \left(\left\{ i\varphi^{-1} \right\}, \frac{i}{N} \right), \quad 0 \le i \le N.$$

Swinbank and Purser [96] define a spherical point set for all odd integers $2N+1$ symmetrically across the equator derived from the irrational lattice with points shifted a half step away from the poles:

$$\theta_i = 2\pi i\varphi^{-1}, \ \ \sin\phi_i = \frac{2i}{2N+1}, \quad -N \le i \le N, \quad -\pi/2 \le \phi_i \le \pi/2.$$

Denote ω_{2N+1} as the configuration generated above. Whereas for large N, the generalized spiral points tend towards flattening out and partitioning the sphere into distinct regions of latitude, the Fibonacci points maintain visible clockwise and counterclockwise spirals as N grows. Labeling the points of ω_{2N+1} by increasing latitude, the dominant spirals emanating from $x_i \in \omega_{2N+1}$ are formed by the sequence $\left\{ x_{i+jF_k} \right\}$ for some Fibonacci number F_k and $j = \cdots, -2, -1, 0, 1, 2, \cdots$. A typical configuration is given in Figure 2.2.

The Fibonacci points derived from the rational lattice are studied by Aistleitner et al [1] and Bilyk et al [10] for discrepancy estimates. In [1], the spherical cap discrepancy of the configurations with total points F_k is bounded by

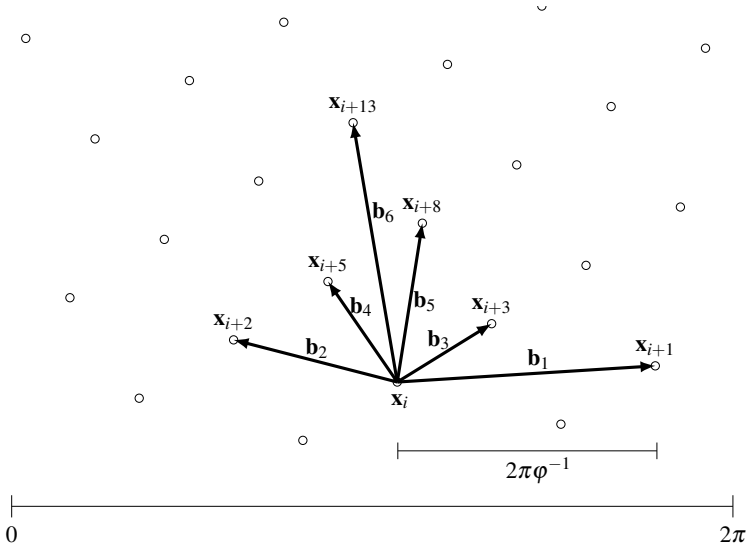

Figure 2.3: Irrational lattice points on the square with labeled basis vectors.

$$D(\Lambda(\widetilde{\omega}_{F_k})) \leq \begin{cases} 44\sqrt{(2/F_k)} & \text{if } k \text{ is odd,} \\ 44\sqrt{(8/F_k)} & \text{if } k \text{ is even.} \end{cases}$$

Numerical experiments in [1] suggest that in fact,

$$D(\Lambda(\widetilde{\omega}_{F_k})) = O\left(\frac{(\log F_k)^c}{F_k^{3/4}}\right), \quad k \to \infty \quad \text{for some } \ 1/2 \leq c \leq 1.$$

which is optimal up to a log power [5]. Both sequences of Fibonacci configurations are equidistributed. However, since the Swinbank and Purser nodes are defined for more values of total points, we will take these to be the Fibonacci sets moving forward. In [96], these points are also numerically shown to be asymptotically equal area as defined in (2.15) below.

Analyzing ω_{2N+1} as a shifted irrational lattice mapped by the Lambert projection helps to visualize the underlying spiral structure. Define a system of basis vectors

$$\mathbf{b}_k = \Lambda^{-1}(x_{i+F_k}) - \Lambda^{-1}(x_i), \quad k = 1,2,3...,$$

which are independent of base point x_i. This is illustrated in Figure 2.3. Emanating from

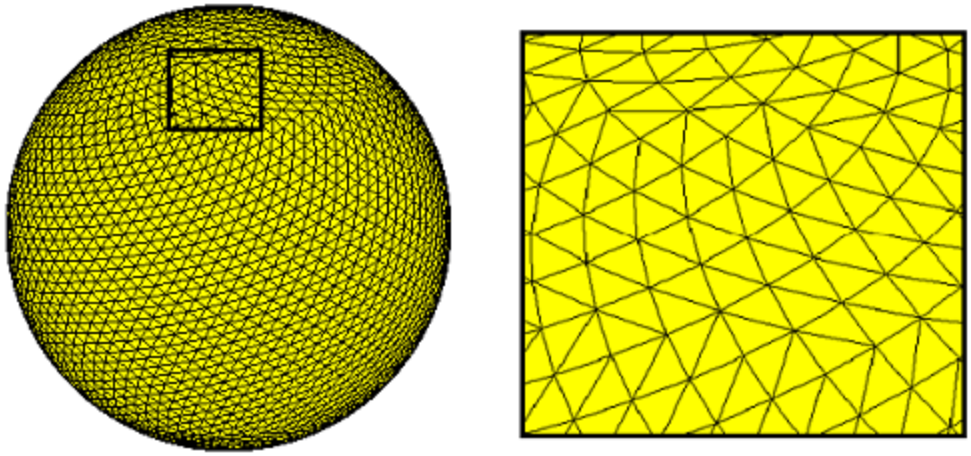

Figure 2.4: Triangulation of $N = 3001$ Fibonacci nodes.

each point x_i, the line of points $\{x_i + m\mathbf{b}_k\}_{m=\cdots,-1,0,1,\cdots}$ is mapped to a spiral on $\mathbb{S}^2$ under the Lambert projection. Like the Fibonacci sequence, the basis vectors satisfy

$$\mathbf{b}_{k+1} = \mathbf{b}_k + \mathbf{b}_{k-1}.$$

On the sphere, the basis vectors in terms of the local Cartesian coordinate system at a point $(\phi_i, \theta_i) \in \omega_{2N+1}$ have the form

$$\mathbf{c}_{k,i} = \left((-1)^k 2\pi \cos\phi_i \varphi^{-k}, \frac{2F_k}{(2N+1)\cos\phi_i} \right). \tag{2.6}$$

For a fixed latitude ϕ and total number of points $2N+1$, the zone number z is defined by

$$\varphi^{2z} = (2N+1)\pi\sqrt{5}\cos^2\phi.$$

Letting $d = \sqrt{4\pi/(\sqrt{5}(2N+1))}$ and using the fact that for large k, $F_k \approx \varphi^k/\sqrt{5}$ equation (2.6) can be rewritten

$$\mathbf{c}_{k,i} \approx d((-1)^k \varphi^{z-k}, \varphi^{k-z}). \tag{2.7}$$

For latitudes where $k - 1/2 \leq z \leq k + 1/2$, $\mathbf{c}_{k,i}$ has the minimum length of the basis vectors

around x_i and forms the dominant spiral at those latitudes. As shown in [96], $|\mathbf{c}_{k,i}|$ is also the smallest distance between points near these latitudes. Thus, the Delaunay triangulation [78] of ω_{2N+1} is composed of $\mathbf{c}_{k,i}, \mathbf{c}_{k-1,i}$, and $\mathbf{c}_{k+1,i}$ when $k-1/2 \leq z \leq k+1/2$. This is shown in Figure 2.4. The enlarged box demonstrates where zone number z changes with changing ϕ. The sudden shift occurs at $z = k \pm 1/2$. Along this latitude, $\mathbf{c}_{k,i}$ and $\mathbf{c}_{k\pm1,i}$ have equal lengths. This allows us to prove quasi-uniformity.

Proposition 2.1.2. *The sequence of Fibonacci configurations is quasi-uniform.*

Numerically, the minimal separation appears to occur at the pole with value $\|x_1 - x_4\| = \|x_{2N+1} - x_{2N-2}\|$ and the largest hole appears to occur in the triangles covering the poles, $\triangle x_2, x_3, x_5$ and $\triangle x_{2N}, x_{2N-1}, x_{2N-3}$. In a straightforward computation, it can be shown that

$$\lim_{N\to\infty} \sqrt{2N+1}\|x_1 - x_4\| = \sqrt{16 - \sqrt{112}\cos(6\pi\varphi^{-1})} = 3.09207...$$

and the circumradius r of the polar triangles satisfies

$$\lim_{N\to\infty} \sqrt{2N+1}\, r = 2.72812....$$

As shown in Table 2.2, the mesh ratios for Fibonacci nodes appear to converge quickly to this ratio $= 0.882298....$

Table 2.2: Mesh Ratios for Fibonacci Nodes

N	$\gamma(\omega_N)$	N	$\gamma(\omega_N)$	N	$\gamma(\omega_N)$
11	0.859197	401	0.881897	20001	0.882289
21	0.872632	501	0.881978	30001	0.882292
31	0.876251	1001	0.882139	40001	0.882293
41	0.877909	2001	0.882218	50001	0.882294
51	0.878857	3001	0.882244	100001	0.882296
101	0.880646	4001	0.882258	200001	0.882297
201	0.881489	5001	0.882266	300001	0.882297
301	0.881762	10001	0.882282	500001	0.882297

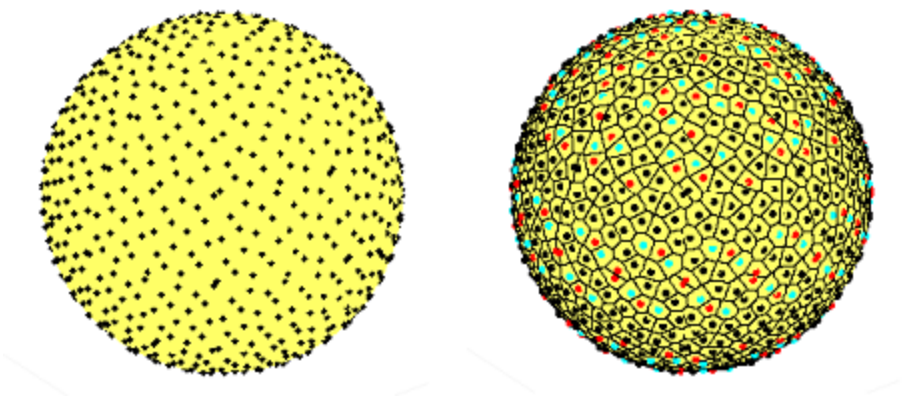

Figure 2.5: Hammersley nodes for $N = 1000$ and corresponding Voronoi decomposition.

2.2 Low Discrepancy Nodes

Another approach for distributing points on the sphere is to minimize a suitable notion of discrepancy, such as spherical cap, L_p, or generalized discrepancy (cf. [23] and [38]). A low spherical cap discrepancy sequence $\{\omega_N\}_{N=2}^{\infty}$ satisfies [5]

$$\frac{a}{N^{3/4}} \leq D_C(\omega_N) \leq A\frac{\sqrt{\log N}}{N^{3/4}}, \qquad N \geq 2, \tag{2.8}$$

for some $a, A > 0$. Low discrepancy point sets are used in Quasi-Monte Carlo methods for numerical integration and also in graphics applications in [104]. One method for generating spherical nodes is to first distribute points on the square $[0,1)^2$ with low planar discrepancy with respect to the L_1 metric [77], i.e. for some $A > 0$

$$D(\omega_N) = \sup_R \left| \frac{R \cap \omega_N}{N} - \sigma(R) \right| \leq A\frac{\log N}{N}, \quad \omega_N \subset [0,1)^2, \tag{2.9}$$

where the supremum R is taken over all rectangles with sides parallel to the axes. These sequences are then mapped to the sphere via the Lambert projection. While the $\log N/N$ term in (2.9) is optimal on the plane [86], it is an open problem whether the images of these sequences have optimal order spherical cap discrepancy. There are several such node distributions in the literature (cf. [1] and [38]), but as their properties are similar, we only

consider the following one.

Hammersley Nodes

For an integer $p \geq 2$, the p-adic van der Corput sequence is defined by

$$x_k^{(p)} = \frac{a_0}{p} + \cdots + \frac{a_r}{p^{r+1}}, \quad \text{where} \quad k = a_0 + \cdots + a_r p^r, \quad a_i \in \{0,1\}.$$

The Hammerlsy node set on the square ([38], [77], and [104]) is given by $x_k := x_k^{(2)}$ and $y_k := \frac{2k-1}{2N}$. The N point spherical Hammersley node set is given by $\{\Lambda(2\pi x_k, 1-2y_k)\}_{k=1}^N$. The configuration for $N = 1000$ is given in Figure 2.5. The discrepancy of the planar Hammersley nodes is known from Niederreiter [77] to satisfy (2.9) . The sequence of Hammersley configurations is equidistributed; however it is not well-separated or quasi-uniform. This makes the nodes poor candidates for energy, as shown in Section 2.8. Their Voronoi decompositions also exhibit no discernible geometric patterns.

2.3 Equal Area Partitions

Another class of point sets are those derived from equal area partitions of the sphere. A partition $P_N := \{W_i\}_{i=1}^N$ of $\mathbb{S}^2$ into N cells whose pairwise intersections have σ-measure 0 is *equal area* if $\sigma(W_i) = 1/N$ for all $1 \leq i \leq N$. A sequence of partitions $\{P_N\}_{N=2}^\infty$ of $\mathbb{S}^2$ such that each P_N has N cells is *diameter bounded* if there are constants $c, C > 0$ such that for all $N \in \mathbb{N}$ and for every cell $W_i^N \in P_N$,

$$cN^{-1/2} \leq \operatorname{diam} W_i^N \leq CN^{-1/2}, \tag{2.10}$$

where $\operatorname{diam}(A) := \sup_{x,y \in A} \|x - y\|$.

Zonal Equal Area Nodes:

Rakhmanov et al [81] construct a diameter bounded, equal area partition of $\mathbb{S}^2$ into rectilinear cells of the form

$$R([\tau_\phi, \nu_\phi] \times [\tau_\theta, \nu_\theta]) := \left\{(\phi, \theta) \in \mathbb{S}^2 \ : \ \tau_\phi \leq \phi \leq \nu_\phi, \tau_\theta \leq \theta \leq \nu_\theta\right\}.$$

The cells are grouped by regions of equal latitude called collars that have the form $R([\tau_\phi, \nu_\phi] \times [0, 2\pi])$. The cells are defined such that $\nu_\phi - \tau_\phi$ and $\nu_\theta - \tau_\theta$ approximate $\sqrt{4\pi/N}$ as N grows. This ensures the correct order of the diameter bound. The cells are defined in the following way.

1. *Determine the latitudes of the polar caps.* The first two cells are taken to be the polar caps of radius $\phi_c = \cos^{-1}(1 - 2/N)$.

2. *Determine the ideal collar angle and ideal number of collars.* The ideal angle between two collars is

$$\delta_I := \sqrt{4\pi/N}.$$

The ideal number of collars between the polar caps, all of which have angle δ_I, is

$$n_I := \frac{\pi - 2\phi_c}{\delta_I}.$$

3. *Determine the actual number of collars, n.* If $N = 2$, then $n := 0$. Otherwise,

$$n := \max\left\{1, \text{round}(n_I)\right\}.$$

4. *Create a list of the ideal number of cells in each collar.* The "fitting" collar angle is

$$\delta_F := \frac{n_I}{n}\delta_I = \frac{\pi - 2\phi_c}{n}.$$

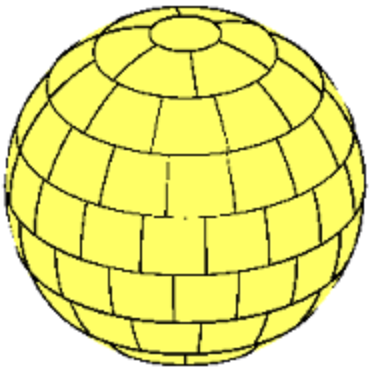

Figure 2.6: Zonal equal area partition of the sphere into 100 cells.

Label the collars $\{C_j\}_{j=1}^{n+2}$ southward with the North polar cap as C_1 and the South polar cap as C_{n+2}. The area A_j of collar C_j can be written as the difference of polar cap areas:

$$A_j = 2\pi(\cos(\phi_c + (j-2)\delta_F) - \cos(\phi_c + (j-1)\delta_F)).$$

Thus the ideal number of cells $y_{j,I}$ in each collar C_j, $j \in \{2,\ldots,n+1\}$, is given by

$$y_{j,I} = \frac{4\pi A_j}{N}.$$

5. *Create a list of the actual number of cells in each collar.* We apply a cumulative rounding procedure. Letting y_j be the number of cells in C_j, define the sequences y and a by $a_1 := 0$, $y_1 := 1$, and for $j \in \{2,\ldots,n+1\}$:

$$y_j := \text{round}(y_{j,I} + a_{j-1}), \qquad a_j := \sum_{k=1}^{j} y_k - y_{k,I}.$$

6. *Create a list of latitudes ϕ_j of each collar and partition each collar into cells.* We define ϕ_j as follows: $\phi_0 = 0$, $\phi_{n+2} = \pi$ and for $j \in \{1,\ldots,n+1\}$,

$$\phi_j = \cos^{-1}(1 - \frac{2}{N}\sum_{k=1}^{j} y_k).$$

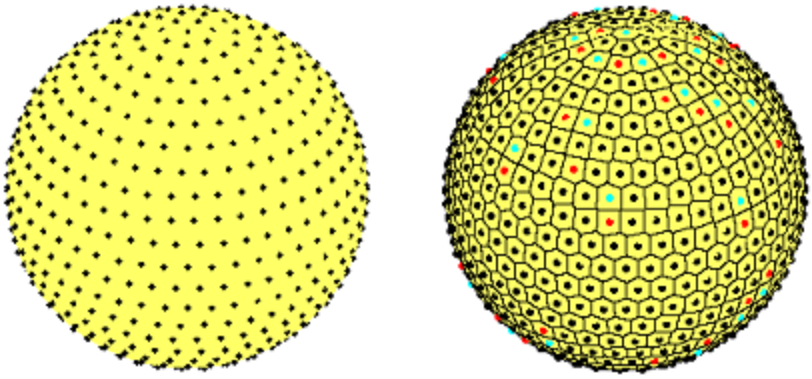

Figure 2.7: Zonal equal area points for $N = 700$ and corresponding Voronoi decomposition.

Thus the North polar cap of radius ϕ_j has normalized area $\sum_{k=1}^{j} y_k/N$, and $C_j := R([\phi_{j-1}, \phi_j] \times [0, 2\pi])$.

7. *Partition each collar into cells.* C_j has y_j equal cells

$$\left\{ R([\phi_{j-1}, \phi_j] \times [\theta_j + k\frac{y_j}{2\pi}, \theta_j + (k+1)\frac{y_j}{2\pi}]) \right\}_{k=0}^{y_j - 1},$$

where $\theta_j \in [0, 2\pi)$ can be chosen to be any starting angle. Note that because θ_j are chosen independently, the equal area partition determined by the algorithm is not unique. Indeed, the collars can rotate past each other without affecting the diameter bound or equal area property of the partition. Because the choice of the θ_j's does not strongly affect the other properties with which we are concerned, we will take them to be random.

The point set ω_N is defined to be the centers of the cells of the rectilinear partition. A configuration and Voronoi decomposition is given in Figure 2.7. As proved by Zhou [107], the cells are diameter bounded from above by $7/\sqrt{N}$; however, numerical experiments from Leopardi in [63] suggest the bound to be $6.5/\sqrt{N}$. For large N, the zonal equal area configurations look very similar to the generalized spiral configurations. Namely they exhibit iso-latitudinal rings with separation between adjacent points equal to separation between rings and a random longitudinal shift between points in adjacent rings. As shown

Table 2.3: Mesh Ratios for Zonal Equal Area Nodes

N	$\gamma(\omega_N)$	N	$\gamma(\omega_N)$	N	$\gamma(\omega_N)$
10	0.711934	400	0.769527	20000	0.758100
20	0.790937	500	0.766808	30000	0.758069
30	0.788546	1000	0.765356	40000	0.756793
40	0.843385	2000	0.764631	50000	0.756785
50	0.790252	3000	0.758645	100000	0.756770
100	0.761296	4000	0.756510	200000	0.756762
200	0.764846	5000	0.764217	300000	0.758015
300	0.763188	10000	0.758192	500000	0.756757

in Section 2.8, the energy computations for both point sets are nearly identical.

Proposition 2.3.1. *The sequence of zonal equal area configurations is equidistributed and quasi-uniform.*

The above construction was modified by Bondarenko et al [11] to create a partition with geodesic boundaries for the creation of well-separated spherical designs. More details can be found in [11]. Table 2.3 gives a comparison of the mesh ratios of the zonal points.

HEALPix Nodes

Developed by NASA for fast data analysis of the cosmic microwave background (CMB), the Hierarchical Equal Area iso-Latitude Pixelization (HEALPix) was designed to have three properties essential for computational efficiency in discretizing functions on $\mathbb{S}^2$ and processing large amounts of data [53]:

1. The sphere is hierarchically tessellated into curvilinear quadrilaterals.
2. The pixelization is an equal area partition of $\mathbb{S}^2$.
3. The point sets are distributed along fixed lines of latitude.

To create the partition of $\mathbb{S}^2$, the authors in [53] first divide the sphere into 12 equal area, four sided pixels defined by the following boundaries:

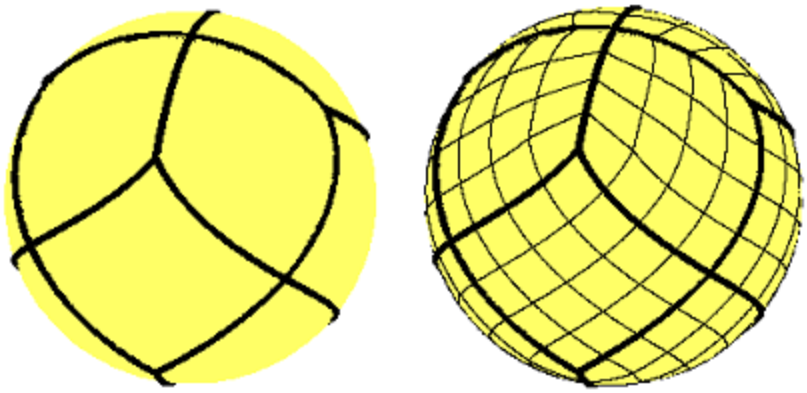

Figure 2.8: Base tessellation of the sphere into 12 equal area pixels.

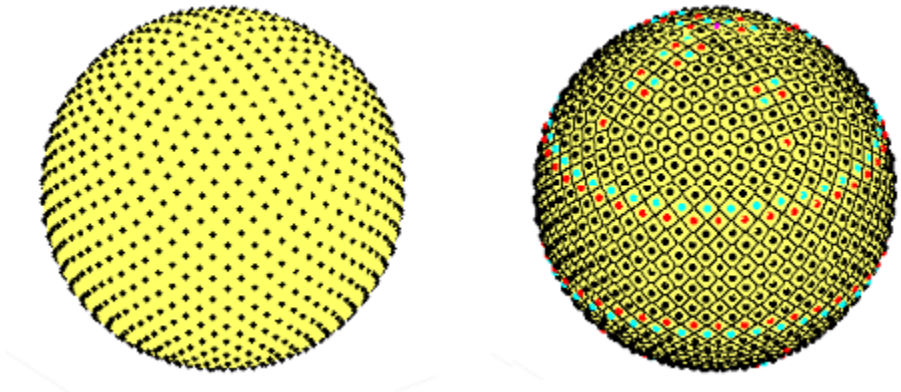

Figure 2.9: HEALPix nodes and Voronoi decomposition for $N = 1200$, $k = 10$.

$$|\cos\phi| > \frac{2}{3}, \quad \theta = m\frac{\pi}{2}, \quad m = 0,1,2,3$$

$$\cos\phi = \frac{-2-4m}{3} + \frac{8\theta}{3\pi}, \quad \frac{m\pi}{2} \leq \theta \leq \frac{(m+1)\pi}{2}, \quad m = 0,1,2,3$$

$$\cos\phi = \frac{2-4m}{3} - \frac{8\theta}{3\pi}, \quad \frac{-(m+1)\pi}{2} \leq \theta \leq \frac{-m\pi}{2}, \quad m = 0,1,2,3.$$

The base tessellation is shown in Figure 2.8. For a given $k \in \mathbb{N}$, each pixel is partitioned into a $k \times k$ grid of sub-pixels of the same shape and equal area. The HEALPix point sets are taken to be the centers of these pixels.

On the polar regions $|\cos\phi| > 2/3$, the points are distributed along k iso-latitudinal rings, indexed by i, each with $4i$ equally spaced points, indexed by j:

$$|\cos\phi_i| = 1 - \frac{i^2}{3k^2}, \qquad \theta_j = \frac{\pi}{2i}\left(j - \frac{1}{2}\right).$$

On the equatorial region, there are $2k-1$ iso-latitudinal rings, each with $4k$ points. The rings are indexed by $k \leq |i| \leq 2k$ and the points by $1 \leq j \leq 4k$:

$$|\cos\phi_i| = \frac{4}{3} - \frac{2i}{3k},$$

$$\theta_j = \frac{\pi}{2k}\left(j - \frac{s}{2}\right), \quad s \equiv (i-k+1) \mod 2.$$

The index s describes the phase shift between rings. This gives a configuration of size $N = 12k^2$. The point sets are hierarchical along the subsequence $k = 3^m$. Holhoş and Roşca [59] have shown that the HEALPix points can be obtained as the image of points on a certain convex polyherdon under an area preserving mapping to the sphere.

Proposition 2.3.2. *The sequence of HEALPix configurations is equidistributed and quasi-uniform.*

Numerically, the mesh ratio appears to be bounded by 1, as shown in Table 2.4.

Table 2.4: Mesh Ratios for HEALPix nodes

k	N	$\gamma(\omega_N)$	k	N	$\gamma(\omega_N)$	k	N	$\gamma(\omega_N)$
1	12	0.864783	9	972	0.965950	45	24300	0.992956
2	48	0.862243	10	1200	0.969599	50	30000	0.993648
3	108	0.909698	15	2700	0.979371	60	43200	0.994701
4	192	0.929080	20	4800	0.984328	70	58800	0.995456
5	300	0.940016	25	7500	0.987365	80	76800	0.996020
6	432	0.951047	30	10800	0.989509	90	97200	0.996455
7	588	0.957584	35	14700	0.990959	100	120000	0.996807
8	768	0.961782	40	19200	0.992082	150	270000	0.997867

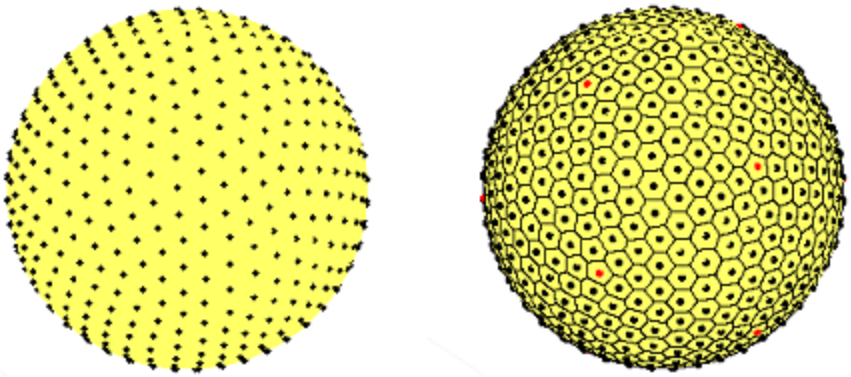

Figure 2.10: Radial icosahedral nodes $N = 642$.

2.4 Polyhedral Nodes and Area Preserving Maps

Another class of point sets are those derived from subdividing regular polyhedra and applying radial projection: $\Pi(\mathbf{x}) = \mathbf{x}/\|\mathbf{x}\|$ or an equal area projection. These node sets are used in finite element methods to give low error solutions to boundary value problems. See, for instance, [51] and [76].

Radial Icosahedral Nodes

This point set, as described in [98] and [105] is formed by overlaying a regular triangular lattice onto each face of a regular icosahedron of circumradius 1 and edge length $a = \csc(2\pi/5)$. Given $k \in \mathbb{N}$, for each vertex v, divide two adjacent edges emanating from v into basis vectors of length a/k. For the face $\mathcal{F}$ determined by these edges and vertex, the icosahedral point set $\widetilde{\omega}_{N_k}$ on $\mathcal{F}$ is taken to be the set of lattice points generated by these basis vectors restricted to $\mathcal{F}$. The spherical points are $\omega_{N_k} := \Pi(\widetilde{\omega}_{N_k})$. These node sets are defined for total points $N = 10k^2 + 2$ and hierarchical along the subsequence $k_j = k_0 2^j$ for any $k_0 \in \mathbb{N}$.

The sequence of icosahedral configurations $\{\widetilde{\omega}_{N_k}\}_{k=1}^{\infty}$ is equidistributed. However, because radial projection is not area preserving, the sequence of spherical configurations is not equidistributed. Density is higher towards the vertices of the icosahedron and lower

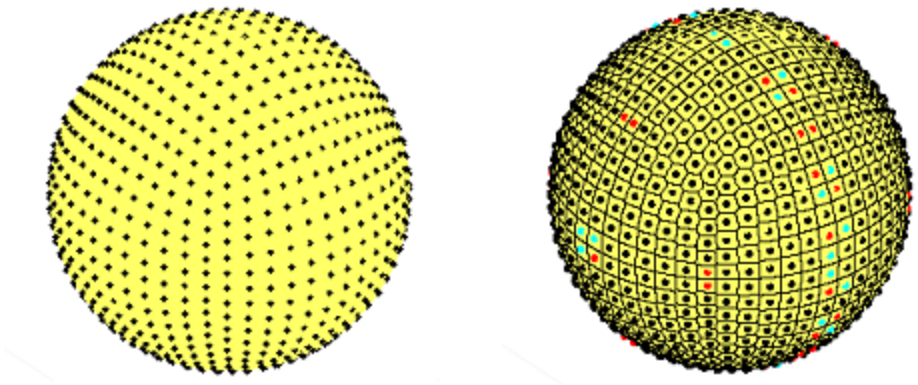

Figure 2.11: Plot of $N = 1016$ cubed sphere points and Voronoi decomposition.

towards the center of the faces where the areal distortion of Π is greatest. The Voronoi decomposition of ω_{N_k} is composed of twelve regular pentagons with all other cells regular hexagons of varying size as illustrated in Figure 2.10.

Proposition 2.4.1. *The sequence of radial icosahedral configurations is quasi-uniform.*

Numerically, the mesh ratio appears to be bounded by 0.86, as shown in Table 2.5.

Table 2.5: Mesh Ratios for Radial Icosahedral Nodes

k	N	$\gamma(\omega_N)$	k	N	$\gamma(\omega_N)$
1	12	0.620429	20	4002	0.830750
2	42	0.667597	30	9002	0.838066
3	92	0.684698	40	16002	0.842358
4	162	0.745348	50	25002	0.844697
5	252	0.765157	60	36002	0.846156
6	362	0.769854	70	49002	0.847376
7	492	0.789179	100	100002	0.849390
10	1002	0.808024	150	225002	0.850941
15	2252	0.821504	200	400002	0.851745

Cubed Sphere Nodes

A similar method as above can be applied to the cube [76]. A square $k \times k$ grid is placed on each face of the cube and radially projected to the sphere. A typical point set is shown in Figure 2.11. The Voronoi cells tend towards regular hexagons near the vertices of the

cube. Towards the middle of each face they resemble a square lattice. The configurations are defined for $N = 6k^2 - 12k + 8$ and are hierarchical along the subsequence $k = k_0 2^m$. By an argument similar to that in the proof of Proposition 2.4.1, the limiting distribution is not uniform, but the sequence of configurations is quasi-uniform. Numerically, the mesh ratio seems to quickly converge to 1, as shown in Table 2.6.

Table 2.6: Mesh Ratios for Cubed Sphere Points

k	N	$\gamma(\omega_N)$	k	N	$\gamma(\omega_N)$	k	N	$\gamma(\omega_N)$
2	8	0.827329	10	488	0.996846	50	14408	0.999893
3	26	0.794265	15	1178	0.994025	60	20888	0.999926
4	56	0.972885	20	2168	0.999289	70	28568	0.999946
5	98	0.933655	25	3458	0.997954	80	37448	0.999959
6	152	0.989913	30	5048	0.999695	90	47528	0.999968
7	218	0.968757	35	6938	0.998979	100	58808	0.999974
8	296	0.994805	40	9128	0.999831	150	133208	0.999988
9	386	0.982046	45	11618	0.999390	200	237608	0.999994

Octahedral Points

Unlike in the previous examples, the octahedral points, described by Holhoş and Roşca [58], are derived from an area preserving map $\mathcal{U}$ from the regular octahedron $\mathbb{K}$ of edge length $L = \sqrt{2\pi}/\sqrt[4]{3}$ and surface area 4π to $\mathbb{S}^2$. Let $\mathcal{U}_x, \mathcal{U}_y$, and $\mathcal{U}_z$ denote the x,y, and z components of $\mathcal{U}$ respectively. For $(X,Y,Z) \in \mathbb{K}$,

$$\mathcal{U}_z = \frac{2Z}{L^2}(\sqrt{2}L - |Z|),$$

$$\mathcal{U}_x = \operatorname{sgn}(X)\sqrt{1-\mathcal{U}_z^2}\cos\frac{\pi|Y|}{2(|X|+|Y|)},$$

$$\mathcal{U}_y = \operatorname{sgn}(Y)\sqrt{1-\mathcal{U}_z^2}\sin\frac{\pi|Y|}{2(|X|+|Y|)}.$$

To produce a spherical point set, the authors form a partition P_k of k^2 triangles on each face of the octahedron in the same manner as the radial icosahedral points and obtain an

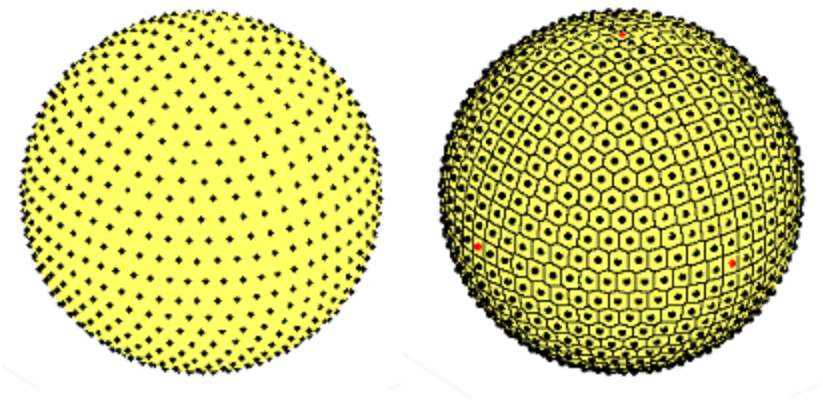

Figure 2.12: Equal area octahedral points for $k = 15$ and $N = 902$.

equal area spherical partition $\mathcal{P}_k = \mathcal{U}(P_k)$. The point sets ω_{N_k} are taken to be the vertices of the triangles of $\mathcal{P}_k$. For a given k, there are $8k^2$ triangles and $N = 4k^2 + 2$ points.

The octahedral configurations have similar properties to the HEALPix node sets. They are iso-latitudinal and hierarchical along the subsequence $k = k_0 2^m$. As shown in Figure 2.12, the Voronoi decomposition of the octahedral points is composed of hexagons and eight squares at the vertices of the octahedron. The hexagons approach regularity towards the center of the faces and deform along the edges. The sequence of configurations is equidistributed, and in addition, the authors in [58] compute a diameter bound for any triangular region $\mathcal{T}$ of $\mathcal{P}_k$ to be

$$\operatorname{diam} \mathcal{T} \leq \frac{2\sqrt{4+\pi^2}}{\sqrt{8k^2}} \approx \frac{7.448}{\sqrt{8k^2}}.$$

Following their proof of this bound, we can calculate a lower bound on the separation and an upper bound on the mesh norm.

Theorem 2.4.2. *The sequence of equal area octahedral configurations is quasi-uniform with*

$$\gamma(\omega_{4k^2+2}) \leq \frac{1}{4}\sqrt{\frac{4+\pi^2}{2-(k+1)^2/k^2}} \to \frac{\sqrt{4+\pi^2}}{4} \approx 0.931048..., \quad k \to \infty. \tag{2.11}$$

Table 2.7: Mesh Ratios for Octahedral Nodes

k	N	$\gamma(\omega_N)$	k	N	$\gamma(\omega_N)$	k	N	$\gamma(\omega_N)$
1	6	0.675511	9	326	0.873510	60	14402	0.905758
2	18	0.872884	10	402	0.875606	70	19602	0.908047
3	38	0.854610	15	902	0.882510	80	25602	0.909875
4	66	0.856329	20	1602	0.886310	90	32402	0.911382
5	102	0.860536	25	2502	0.888702	100	40002	0.912644
6	146	0.864599	30	3602	0.892884	200	160002	0.919218
7	198	0.868095	40	6402	0.898762	300	360002	0.921947
8	258	0.871036	50	10002	0.902784	400	640002	0.923503

This bound seems to be near optimal. As shown in Table 2.7, the mesh ratio grows to at least 0.9235.

2.4.1 Equidistributed mesh icosahedral nodes

Improvements to the radially projected icosahedral points have been put forth by Song et al [93] and Tegmark [99]. Here, we introduce two other improvements to these points to create new configurations. First, we generalize the icosahedral lattice structure to create configurations of more possible numbers of total points. Due to a method of Caspar and Klug [28] derived during their investigation of the construction of viruses, we define a triangular lattice on a regular icosahedron with total points

$$N = 10(m^2 + mn + n^2) + 2, \qquad (m,n) \in \mathbb{N} \times \mathbb{N} \setminus (0,0).$$

Consider the triangular lattice $\Lambda_2 \subset \mathbb{R}^2$ generated by $e_1 = (1,0)$ and $e_2 = (1/2, \sqrt{3}/2)$. For a given (m,n), let $e_{m,n} = me_1 + ne_2$ and it's rotation by $\pi/3$ be basis vectors for an unfolded icosahedron superimposed on the lattice. This is illustrated in Figure 2.13. Folding the icosahedron results in a triangular lattice $\widetilde{\omega}_{m,n}$ on each face. Due to rotational symmetry of the lattice, the resulting configuration is independent of how the icosahedron is unfolded.

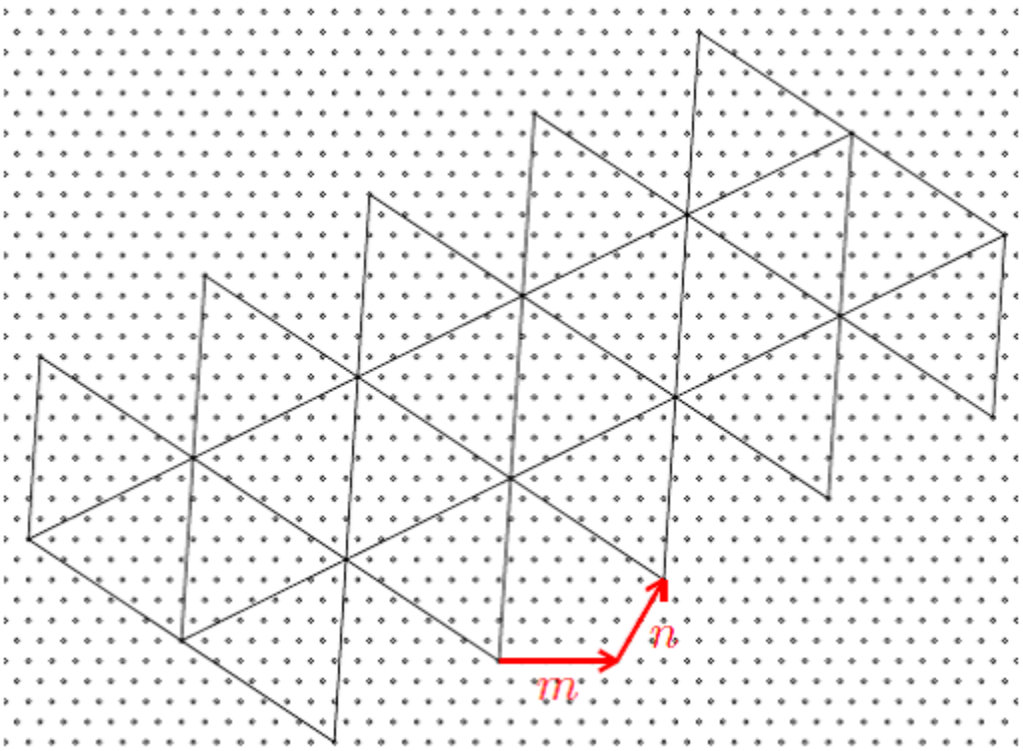

Figure 2.13: Planar icosahedral mesh for $(m,n) = (5,4)$.

The subsequence $(m,0)$ produces the lattice for the radial icosahedral nodes. The following number theoretic result makes precise the improvement given by the (m,n) subsequences in terms of the possible number of total points N in the resulting configuration.

Proposition 2.4.3. *Let* $T := \left\{x = 10(m^2+mn+n^2)+2 \mid m,n \in \mathbb{N}\right\}$ *and let*

$$S(N) := |\{x \in T \mid x \leq N\}|.$$

Then,

$$S(N) = O\left(\frac{N}{\sqrt{\log N}}\right). \tag{2.12}$$

By comparison, for points generated along the subsequence $(m,0)$ as realized by the radial icosahedral nodes as well as the configurations in [93] and [99], the analogous quantity

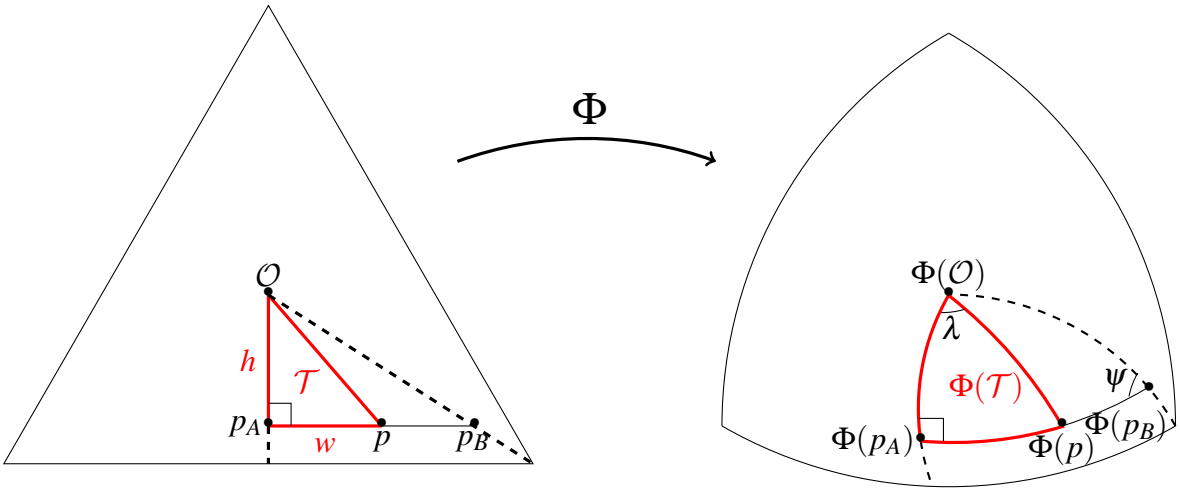

Figure 2.14: Illustration of area preserving map Φ defined piecewise on each triangle bounded by two altitudes of an icosahedral face.

$S(N) = O(\sqrt{N})$.

Secondly, we derive an area preserving map Φ from the regular icosahedron $\mathcal{I}$ of edge length $L = \sqrt{4\pi}/\sqrt[4]{75}$, circumradius $r = L\sin 2\pi/5$, and surface area 4π using the technique presented by Snyder [91] for the truncated icosahedron. We define Φ piecewise by dividing each face $\mathcal{F} \subset \mathcal{I}$ into the six triangles $\mathcal{R}_i$ partitioned by the altitudes of $\mathcal{F}$:

1. Parametrize each point $p \in \mathcal{R}_i$ by h and w as labeled in Figure 2.14. If A is the side of $\mathcal{R}_i$ of length $L/2\sqrt{3}$, then w is the distance from p to A and h is the distance of $p_A :=\text{proj}(p,A)$ to $\mathcal{O}$, the center of $\mathcal{F}$.

2. Let B be the side of $\mathcal{R}_i$ of length $L/\sqrt{3}$ and p_B be the intersection of the line $\overline{p_A p}$ with B. For the triangle $\mathcal{S} = \triangle p_A p_B \mathcal{O}$, find ψ as in Figure 2.14 and spherical right triangle $\Phi(\mathcal{S})$ such that $\sigma_{\mathcal{I}}(\mathcal{S}) = \sigma_{\mathbb{S}^2}(\Phi(\mathcal{S})) = \psi - \pi/6$. Thus,

$$\psi = \frac{h^2\sqrt{3}}{2} + \frac{\pi}{6}.$$

3. The point $\Phi(p)$ will lie on the great circle $\Phi(\overline{p_A p_B})$. Letting $\mathcal{T} = \triangle p_A p \mathcal{O}$, find λ as

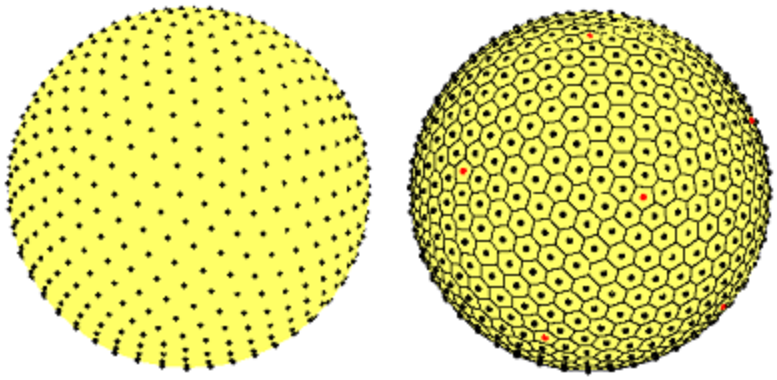

Figure 2.15: Equidistributed mesh icosahedral nodes for $(m,n) = (7,2)$.

in Figure 2.14 such that $\sigma_{\mathcal{I}}(\mathcal{T}) = \sigma_{\mathbb{S}^2}(\Phi(\mathcal{T}))$. By the spherical law of cosines,

$$\sigma_{\mathbb{S}^2}(\Phi(\mathcal{T})) = \lambda + \cos^{-1}\left(\frac{2\sin\lambda\cos\psi}{\sqrt{3}}\right) - \frac{\pi}{2}.$$

Thus

$$\tan\lambda = \frac{\sin(\frac{hw}{2})}{\cos(\frac{hw}{2}) - \frac{2\cos\psi}{\sqrt{3}}}.$$

4. Transform (ψ,λ) into spherical coordinates.

The map Φ is extended to $\mathcal{I}$ by rotations and reflections. This defines the unique azimuthal equal area projection from $\mathcal{I}$ onto $\mathbb{S}^2$ [92]. The spherical configurations are $\omega_{m,n} := \Phi(\widetilde{\omega}_{m,n})$. A typical point set is shown in Figure 2.15. The Voronoi cells are almost regular hexagons with 12 pentagonal cells at the vertices of $\mathcal{I}$, and the Voronoi decomposition forms a spherical Goldberg polyhedron [52]. To implement the points in Matlab, we derive explicit formulas on a triangular face.

Unlike the radial icosahedral points, the sequence of equal area configurations is equidistributed on $\mathbb{S}^2$ because Φ is an area preserving map and the icosahedral configurations $\widetilde{\omega}_{m,n}$ are equidistributed on $\mathcal{I}$. We have the following regarding quasi-uniformity.

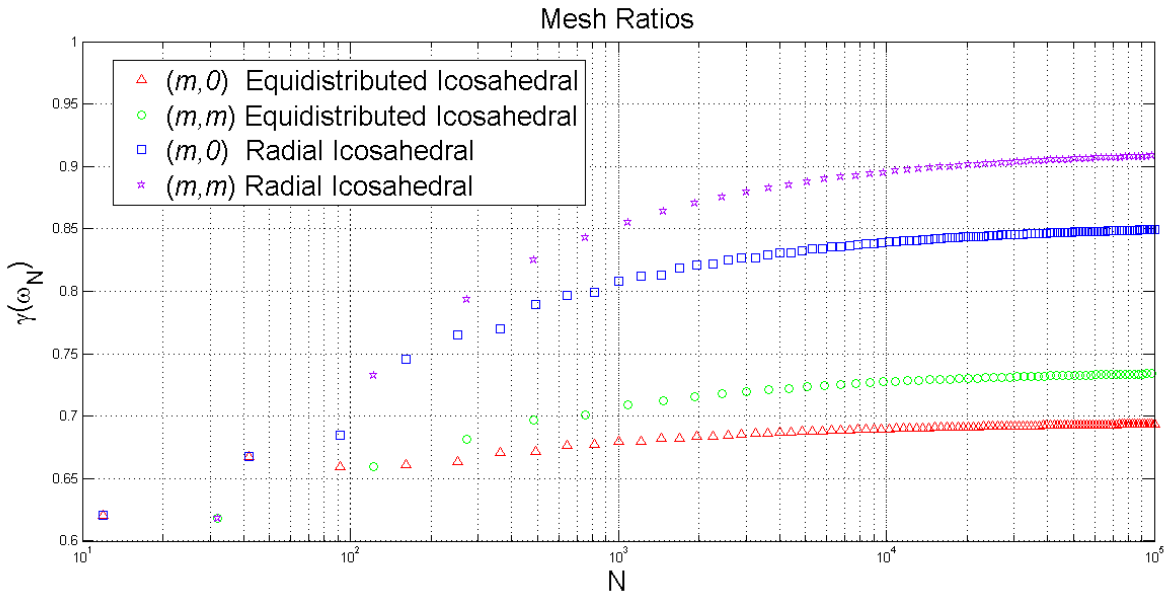

Figure 2.16: Plot of mesh ratios for radial and equidistributed icosahedral nodes sampled along the subsequences $(m,0)$ and (m,m).

Theorem 2.4.4. *The sequence of equal area icosahedral configurations is quasi-uniform with*

$$\gamma(\omega_N) \leq 0.798.... \tag{2.13}$$

Figure 2.16 compares the mesh ratios of the icosahedral configurations under radial projection versus projection by Φ along the subsequences $(m,0)$ and (m,m) for total points $N < 100,000$. Both equidistributed subsequences have lower mesh ratios than the radially projected subsequences and perform better than the bound in Theorem 2.4.4. These are the lowest mesh ratios of all point sets discussed.

Conjecture 2.4.5. *For the special subsequence* $(m,0)$,

$$\liminf_{m\to\infty} \gamma(\omega_{m,0}) \leq 0.697....$$

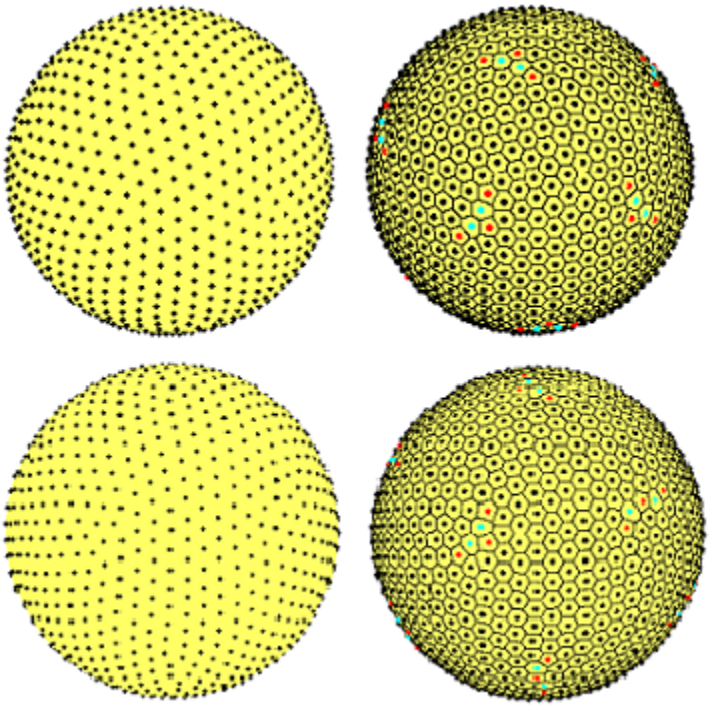

Figure 2.17: Coulomb points (top) and log energy points (bottom) and their Voronoi decomposition for $N = 1024$.

2.5 Nodes via Optimization

Coulomb Points and Log Energy Points

For $s = 1$, Riesz s-energy minimization on $\mathbb{S}^2$ is the classic Thomson problem for the Coulomb potential [100]. The sequence of minimal Coulomb energy configurations is known to be equidistributed, well-separated, and quasi-uniform [39]. However, no explicit bound is known for the mesh ratio. The Voronoi decomposition of these cells, as shown in Figure 2.17, primarily consists of close to regular hexagons with heptagons and pentagons forming scars along the sphere. For relatively small N, the scars grow out from the 12 vertices of the icosahedron like dislocations in a crystal due to displacement deformities. For $N > 5,000$, the scars become less fixed, spreading across the sphere. For an in-depth discussion of the scarring behavior, see Bowick et al [18] and [19].

The log energy points, also called elliptic Fekete points, are minimizers of the Riesz log-

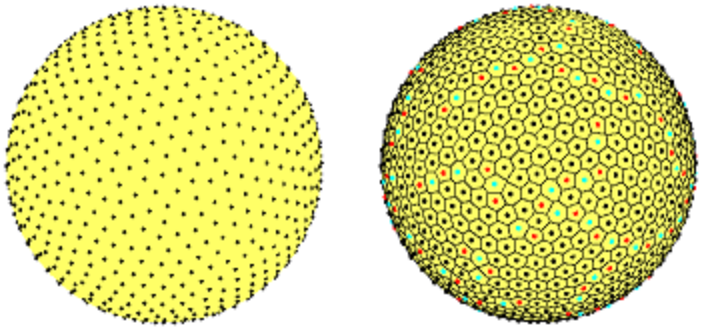

Figure 2.18: Maximal determinant nodes for $N = 961$.

arithmic potential. The sequence of log energy configurations is known to be equidistributed and well-separated, but covering and quasi-uniformity is an open problem. As shown in Table 2.8 below, numerically the log energy points appear to be quasi-uniform. The best known lower bound on separation is due to Dragnev [43]:

$$\delta(\omega_N^{\log}) \geq \frac{2}{\sqrt{N}}, \quad N \geq 2.$$

Their geometric structure is very similar to the Coulomb points as shown in Figure 2.17. The energies of log and Coulomb points have the same asymptotic behavior in the dominant and second order term for many Riesz potentials (see [56]).

Generating these points is a highly nonlinear optimization problem. Unlike the configurations we have described up to now, they are not so quickly obtained. Table 2.8 displays the mesh ratios of near minimal Coulomb and log energy configurations. We remark that the sequence appears to have outliers at several values of N, such as $N = 20,\ 300$, and 4096. Points for $N < 500$ and $N = k^2$, $k \leq 150$, were provided by Rob Womersley.

Maximal Determinant Nodes

Other node sets used in polynomial interpolation and numerical integration on the sphere are the maximal determinant nodes (Fekete nodes). Let $\phi_1, ..., \phi_{(n+1)^2}$ be a basis for the space $\mathbb{P}_n(\mathbb{S}^2)$ of spherical polynomials of degree $\leq n$. The maximal determinant node set is

Table 2.8: Mesh Ratios for Coulomb and Log Energy Points

N	$\gamma(\omega_N^{\log})$	$\gamma(\omega_N^{\text{Coul}})$	N	$\gamma(\omega_N^{\log})$	$\gamma(\omega_N^{\text{Coul}})$
10	0.687401	0.689279	500	0.757354	0.755834
20	0.731613	0.733265	1024	0.752122	0.755770
30	0.695481	0.692966	2025	0.761261	0.766218
40	0.669531	0.670842	3025	0.765075	0.761661
50	0.661301	0.656591	4096	0.770240	0.765712
100	0.695371	0.694604	5041	0.753573	0.758457
200	0.662102	0.658561	10000	0.762672	0.761964
300	0.740635	0.730182	15129	0.762385	0.763398
400	0.650106	0.647351	22500	0.773483	0.767096

the configuration $\omega_N := \omega_{(n+1)^2} \subset \mathbb{S}^2$ which maximizes

$$\det(\phi_i(x_j))_{i,j=1}^{(n+1)^2}$$

These points are independent of the choice of basis. The interpolatory cubature rule associated with the configuration ω_N,

$$Q_n(f) := \sum_{j=1}^{N} w_j f(x_j),$$

is conjectured in [89] to have all weights positive which is of interest in numerical integration. For more information about these points and their applications, see [83], [84], and [89]. A typical node set is shown in Figure 2.18. The Voronoi decomposition is primarily composed of regular hexagons with scarring features similar to the minimal energy points.

Also like the minimal energy points, computing the maximal determinant nodes is a nonlinear optimization problem. The maximum is approximated by conjugate gradient and Newton-like methods on $\mathbb{S}^2$ [89]. Nodes for $1 \leq n \leq 165$ are available from *http://web.maths.unsw.edu.au/~rsw/Sphere/Extremal/New/index.html*.

Berman et al [6] proved the sequence of maximal determinant configurations is equidis-

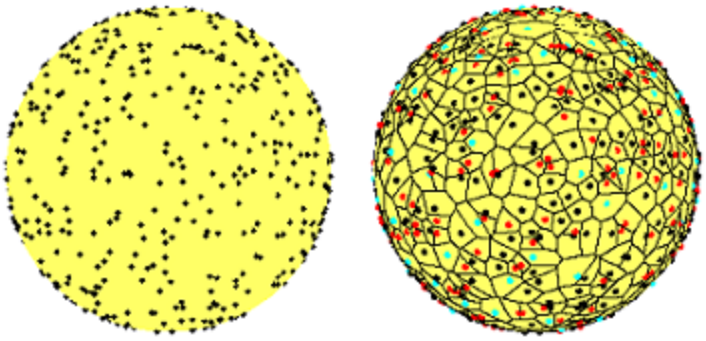

Figure 2.19: Random points for $N = 700$ and their Voronoi decomposition.

tributed, while in [89], Sloan and Womersley proved it is quasi-uniform with

$$\limsup_{N\to\infty} \gamma(\omega_N) < \frac{4z_1}{\pi} = 3.06195\ldots,$$

where z_1 is the smallest positive zero of the Bessel function of the first kind, $J_0(z)$. As shown in Table 2.9, the mesh ratio bound appears to be much lower though it is unclear whether or not $\lim_{N\to\infty} \gamma(\omega_N)$ exists.

Table 2.9: Mesh Ratios for Maximal Determinant Nodes

N	$\gamma(\omega_N)$	N	$\gamma(\omega_N)$
9	0.718884	625	0.805608
16	0.685587	1024	0.840506
25	0.768510	2025	0.858874
36	0.806140	3025	0.847347
49	0.777490	4096	0.859887
100	0.708579	4900	0.877990
225	0.860728	10201	0.859625
324	0.799227	15129	0.865695
400	0.809172	22500	0.881492

2.6 Random Points

The final configurations we consider are random configurations ω_N^{rand} consisting of N independent samples chosen with respect to surface area measure. Not surprisingly, these

configurations do not have optimal order separation or covering and the sequence is not quasi-uniform. As proved in [24] and [85] respectively,

$$\lim_{N\to\infty} \mathbb{E}(\delta(\omega_N^{\text{rand}}))N = \sqrt{2\pi}, \qquad \lim_{N\to\infty} \mathbb{E}(\eta(\omega_N^{\text{rand}}))\left(\frac{N}{\log N}\right)^{1/2} = 2.$$

Note that while the order of the separation of random points is off by factor of $N^{1/2}$, the covering is only off by a factor of $\sqrt{\log N}$. Figure 2.19 shows a realization of i.i.d. uniformly chosen random points on $\mathbb{S}^2$.

2.7 Summary of Properties

The following tables compare some of the properties of the point sets described above. Table 2.10 compares which sequences are proven to be equidistributed and well-separated, for which values of N the configurations are defined, and whether a subsequence is hierarchical. Table 2.11 compares which sequences are quasi-uniform and the numerically determined bounds for separation and mesh ratio constants.

Table 2.10: Summary of Point Set Properties

Name	Defined for	Hier.	Equidist.	Separated
Gen. Spiral	$N \geq 2$	No	Yes	Yes
Fibonacci	Odd N	No	Yes	Yes
Hammersley	$N \geq 2$	No	Yes	No
Zonal Eq. Area	$N \geq 2$	No	Yes	Yes
HEALPix	$12k^2$,	Subseq.	Yes	Yes
Octahedral	$4k^2+2$	Subseq.	Yes	Yes
Radial Icos.	$10k^2+2$,	Subseq.	No	Yes
Cubed Sphere	$6k^2-12k+8$	Subseq.	No	Yes
Equidist. Icos.	$10(m^2+mn+n^2)+2$	Subseq.	Yes	Yes
Coulomb	$N \geq 2$	No	Yes	Yes
Log Energy	$N \geq 2$	No	Yes	Yes
Max Det.	$(1+k)^2$	No	Yes	Yes
Random	$N \geq 2$	No	Yes	No

Table 2.11: Comparison of Separation and Mesh Ratio Constants

Name	Quasi-Uniform	Numeric lower bound on $\liminf \delta(\omega_N)\sqrt{N}$	Numeric upper bound on $\limsup \gamma(\omega_N)\sqrt{N}$
Gen. Spiral	Yes	3.1319	0.8099
Fibonacci	Yes	3.0921	0.8823
Hammersley	No	N/A	N/A
Zonal Eq. Area	Yes	3.3222	0.7568
HEALPix	Yes	2.8345	1.0000
Radial Icos.	Yes	2.8363	0.8517
Cubed Sphere	Yes	2.7027	1.0000
Octahedral	Yes	2.8284	0.9235
Equidist. Icos.	Yes	3.1604	0.7360
Coulomb	Yes	3.3794	0.7671
Log Energy	Conj.	3.3733	0.7735
Max Det.	Yes	3.1957	0.8900
Random	No	N/A	N/A

2.8 A Riesz Energy Comparison

We next examine the Riesz energy of the above spherical configurations. For $0 < s < 2$, a characterization of asymptotically optimal point sets is due to Leopardi [65].

Theorem 2.8.1. *If a well-separated sequence of configurations $\{\omega_N\}_{N=2}^{\infty}$ is equidistributed, then it is asymptotically optimal for $0 < s < 2$, that is from* (1.10)*,*

$$\lim_{N\to\infty} \frac{E_s(\omega_N)}{N^2} = \mathcal{I}_s[\sigma_{\mathbb{S}^2}] = \frac{2^{1-s}}{2-s}.$$

Thus the generalized spiral, Fibonacci, zonal equal area, HEALPix, octahedral, equidistributed icosahedral, maximal determinant, and Coulomb and log energy points are all minimal to the leading order term of $\mathcal{E}_s(N)$, for $0 < s < 2$. An analogous statement is conjectured for the logarithmic energy [56].

For $s > 2$, from Theorem 1.2.4, $\mathcal{E}_s(N, \mathbb{S}^2)$ has leading order $N^{1+s/d}$. Figure 2.20 plots $E_3(\omega_N)/N^{5/2}$ for the point sets. Some configurations are sampled along subsequences to avoid overcrowding the picture. Due to the computational cost of generating approximate

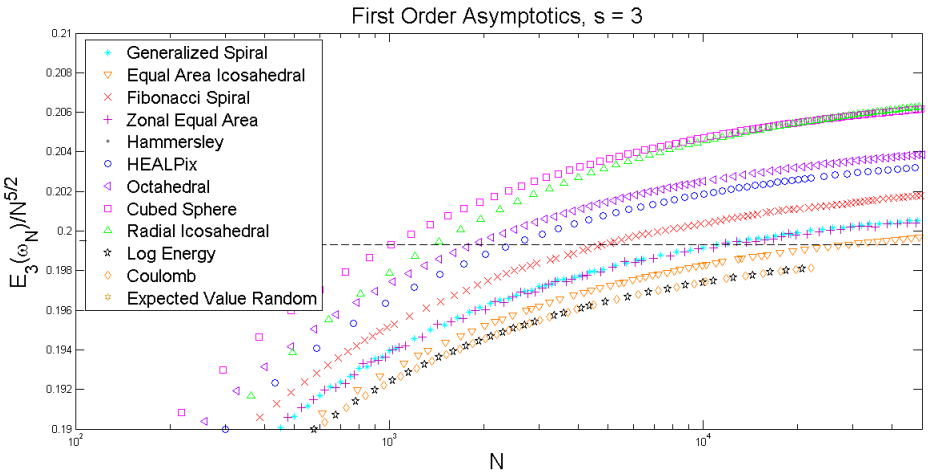

Figure 2.20: Comparison of Riesz energies in the hypersingular case

log energy and Coulomb points, these points are only available for $N < 22,500$. We do not include the maximal determinant nodes because there is no known algorithm to generate them in polynomial time.

The dashed line is the conjuectured value of $C_{3,2} \approx 0.199522$ given by Conjecture 1.3.2. The energies of most configurations seem to be going to the correct order but incorrect coefficient. The equidistributed icosahedral points outperform the other algorithmically generated configurations. Heuristically, this is expected because their Voronoi decomposition is closest to a regular hexagonal lattice. The log energy and Coulomb points seem to be close to minimal and may converge to the conjectured value. The Hammersley points are not seen on the plot because their asymptotic energy does not appear to have leading order $N^{5/2}$. For random points, the expected value of the Riesz s-energy is computed to be:

$$\mathbb{E}[E_s(\omega_N^{\text{rand}})] = \mathcal{I}_s[\sigma_{\mathbb{S}^2}](N(N-1)). \tag{2.14}$$

Thus, for $s \geq 2$, $\mathbb{E}[E_s(\omega_N^{\text{rand}})] = \infty$. More energy comparisons of the point sets for other values of s and lower order terms can be found in [56].

2.9 Proofs of Equidistribution and Mesh Ratios

In this section we collect the proofs of the results presented in the previous sections of this chapter. Throughout this section, let $\sigma := \sigma_{\mathbb{S}^2}$ be the normalized surface area measure on $\mathbb{S}^2$. We will call a sequence of partitions $P_N := \{W_i\}_{i=1}^N$ of $\mathbb{S}^2$ *asymptotically equal area* if

$$\lim_{N\to\infty} N \max_{1\le i\le N} \sigma(W_i) = \lim_{N\to\infty} N \min_{1\le i\le N} \sigma(W_i) = 1, \tag{2.15}$$

and a sequence of spherical configurations $\{\omega_N\}_{N=1}^\infty$ will be said to be asymptotically equal area if its sequence of Voronoi decompositions is asymptotically equal area. We begin with an auxiliary result.

Proposition 2.9.1. *Let $\{P_N\}_{N=1}^\infty$ be a diameter bounded sequence of asymptotically equal area partitions of $\mathbb{S}^2$ such that each P_N has N cells. For each P_N, let ω_N be a configuration of points on $\mathbb{S}^2$ such that the interior of each cell of P_N contains exactly one point of ω_N. Then $\{\omega_N\}_{N=1}^\infty$ is equidistributed and provides a covering of $\mathbb{S}^2$ with $\eta(\omega_N) \le CN^{-1/2}$ for all $N \in \mathbb{N}$, where C is as in equation* (2.10).

Proof. The bound on the covering radius is trivial. Let $A \subset \mathbb{S}^2$ be a spherical cap and let

$$A_\delta := \left\{x \in \mathbb{S}^2 : \ \operatorname{dist}(x,A) \le \delta\right\},$$

where $\operatorname{dist}(x,A) := \min_{y\in A} \|x-y\|$ is the standard distance function. For $x \in \omega_N$, denote by W_x^N the cell of P_N containing x. Let $\varepsilon, \delta > 0$ and choose N large enough such that

$$N \min_{x\in\omega_N} \sigma(W_x^N) \ge 1-\varepsilon$$

and $x \in A \cap \omega_N$ implies $W_x^N \subset A_\delta$. Then

$$\frac{|\omega_N \cap A|}{N} \le \frac{|\left\{x \ : \ W_x^N \subset A_\delta\right\}|}{N} \le \frac{\sigma(A_\delta)}{N \min_{x\in\omega_N} \sigma(W_x^N)} \le \frac{\sigma(A_\delta)}{1-\varepsilon}.$$

Since ε is arbitrary, we have

$$\limsup_{N\to\infty} \frac{|\omega_N \cap A|}{N} \leq \sigma(A_\delta).$$

Letting $\delta \to 0$ gives

$$\limsup_{N\to\infty} \frac{|\omega_N \cap A|}{N} \leq \sigma(A). \tag{2.16}$$

Applying inequality (2.16) to $\mathbb{S}^2 \setminus A$, we obtain

$$\liminf_{N\to\infty} \frac{|\omega_N \cap A|}{N} = 1 - \limsup_{N\to\infty} \frac{|\omega_N \cap (\mathbb{S}^2 \setminus A)|}{N} \geq 1 - \sigma(\mathbb{S}^2 \setminus A) = \sigma(A),$$

and thus, we have

$$\lim_{N\to\infty} \frac{|\omega_N \cap A|}{N} = \sigma(A).$$

□

Proof of Theorem 2.1.1. For a fixed N denote in spherical coordinates $x_i := (\phi_i, \theta_i) \in \omega_N$. We first prove the separation bound. Let $\varepsilon_N = 2\sqrt{4\pi/N}$. We can restrict our attention to ε_N-balls $B(x_k, \varepsilon_N)$ and a hemisphere, i.e, $k \leq N/2$. For large N, if $k < 8\pi + 1/2$, then

$$\cos\phi_k = 1 - \frac{2k-1}{N} \geq 1 - \frac{16\pi}{N} \approx \cos(2\sqrt{\frac{4\pi}{N}}),$$

and x_k is within the first two full longitudinal turns of S_N starting from a pole. Otherwise, $B(x_k, \varepsilon_N)$ contains disjoint levels of S_N. In this case, the minimal distance between levels in $B(x_k, \varepsilon_N)$ is $\sqrt{4\pi/N}$. We compute the nearest neighbor distance between points in the same level as follows. Let

$$f_N(k) := \sqrt{N}\|x_k - x_{k+1}\|, \quad x_k \in \omega_N, \quad k < N/2.$$

Using the distance formula for spherical coordinates

$$\|x_j - x_k\|^2 = 2 - 2(\cos\phi_j \cos\phi_k + \sin\phi_j \sin\phi_k \cos(\theta_j - \theta_k)) \tag{2.17}$$

and expanding $\cos^{-1} x$ around $x = 1$ we have

$$\lim_{N\to\infty} f_N(k) = \sqrt{8k - 4\sqrt{4k^2-1}\cos(\sqrt{2\pi}(\sqrt{2k-1} - \sqrt{2k+1}))}, \tag{2.18}$$

and $f_N(k) < f_{N+1}(k)$ for all $k < N/2 - 1$ and large N. Thus we have the correct order for the minimal separation between adjacent points in ω_N. Furthermore, (2.18) is increasing as a function of k and thus

$$\lim_{N\to\infty} \min_k f_N(k) = \sqrt{8 - 4\sqrt{3}\cos(\sqrt{2\pi}(1-\sqrt{3}))}. \tag{2.19}$$

Lastly, around the north pole, $k_1, k_2 < 8\pi + 1/2$, we can again use (2.17) to show that

$$\lim_{N\to\infty} \sqrt{N}\|x_{k_1} - x_{k_2}\|$$

exists and can be computed case by case for pairs (k_1, k_2). The southern hemisphere can be similarly computed. Comparing to (2.19) gives the separation constant (2.2).

For covering, given $y \in \mathbb{S}^2$,

$$\text{dist}(S_N) \leq \sqrt{\frac{\pi}{N}}.$$

From (2.18), the maximal distance from any point on S_N to a point of ω_N is $O(1/\sqrt{N})$ and thus the covering radius of ω_N is also $O(1/\sqrt{N})$.

We have two additional observations. First, the Voronoi decompositions of the spiral points are diameter bounded. Secondly, the Voronoi cells are asymptotically equal area on $K_h := \left\{(x,y,z) \in \mathbb{S}^2 : -h \leq z \leq h\right\}$ for any fixed $0 < h < 1$. By this we mean

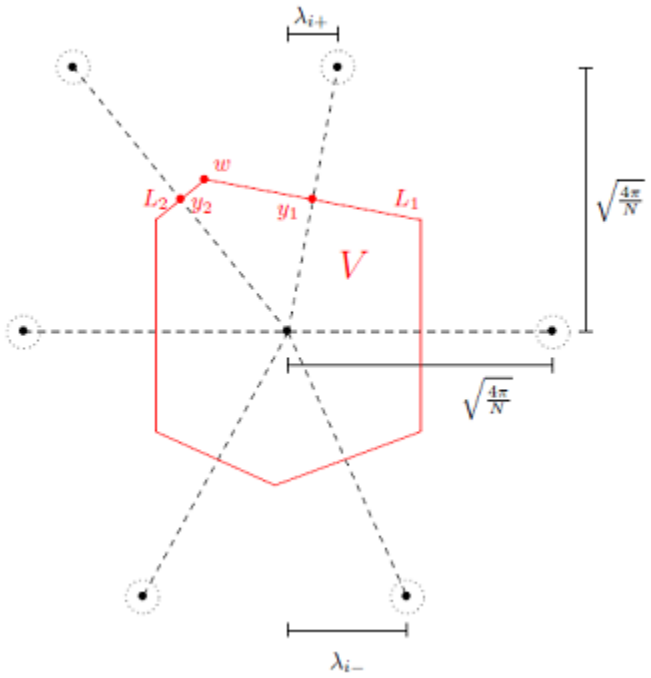

Figure 2.21: Limiting form of Voronoi cell for each $x_i \in K_h \cap \omega_N$.

$$\lim_{N\to\infty} N \max_{V_x(\omega_N)\subset K_h} \sigma(V_x(\omega_N)) = \lim_{N\to\infty} N \min_{V_x(\omega_N)\subset K_h} \sigma(V_x(\omega_N)) = 1.$$

Indeed, fixing h, for any $\varepsilon > 0$, we can take N large enough such that given $x_i = (\phi_i, \theta_i) \in K_h \cap \omega_N$, x_{i-1}, and x_{i+1} are almost iso-latitudinal with x_i with separation $\sqrt{4\pi/N}$. I.e.,

$$|x_{i\pm1} - (\phi_i, \theta_i \pm \csc\phi_i \sqrt{4\pi/N})| < \varepsilon.$$

There exists shifts $0 \le \lambda_{i+}, \lambda_{i-} \le \sqrt{4\pi/N}$ such that the nearest points in the adjacent spiral levels are within ε of the points $(\phi_i \pm \sqrt{4\pi/N}, \theta_i + \csc\phi_i \lambda_{i\pm})$ and $(\phi_i \pm \sqrt{4\pi/N}, \theta_i + \csc\phi_i(\lambda_{i\pm} - \sqrt{4\pi/N}))$. Thus as $N \to \infty$, the Voronoi cell $V_i(\omega_N)$ approaches the form of V in Figure 2.21 and

$$\sigma(V_i(\omega_N)) = \sigma(V) + O(\varepsilon^2).$$

Furthermore, we can treat V as a planar polygon in Figure 2.21, and

$$\sigma(V) = \frac{1}{N}$$

independent of the shifts $\lambda_{i\pm}$. This we show by direct computation.

Letting $a = \sqrt{4\pi/N}$ and centering x_i at $(0,0)$, the points $y_1 = (\lambda_{i+}/2, a/2)$ and $y_2 = ((\lambda_{i+} - a)/2, a/2)$ are the midpoints of the lines connecting x_i to its nearest neighbors in the adjacent level which are shifted by λ_{i+}. The corresponding lines

$$L_1 : y = -\frac{\lambda_{i+}}{a}(x - \frac{\lambda_{i+}}{2}) + \frac{a}{2} \qquad L_2 : y = \frac{a - \lambda_{i+}}{a}(x - \frac{\lambda_{i+} - a}{2}) + \frac{a}{2}$$

form the top boundary of V and have intersection point

$$w := (\lambda_{i+} - a/2, (\lambda_{i+}a + a^2 - \lambda_{i+}^2)/2a).$$

From this we calculate the area of the top half of V to be

$$\sigma(V_{top}) = \frac{1}{4\pi}\left[a\left(\frac{-a\lambda_{i+} + \lambda_{i+}^2 + a^2}{2a}\right) + \frac{a}{2}\left(\frac{a\lambda_{i+} - \lambda_{i+}^2}{a}\right)\right] = \frac{1}{2N}.$$

The same calculation holds for the bottom half of V and thus (2.15) holds.

We now consider equidistribution. Because the height steps between points in ω_N are uniform, for a spherical cap A centered at a pole,

$$\lim_{N\to\infty} \frac{|\omega_N \cap A|}{N} = \sigma(A). \tag{2.20}$$

If A does not contain one of the poles, then $A \subset K_h$ for some h and (2.20) holds by Proposition 2.9.1. Finally if A is a cap containing but not centered at one of the poles, A can be partitioned into an open cap of height h centered at the pole and $A \cap K_h$. Because (2.20) holds on each disjoint subset, it also holds on A. □

Proof of Proposition 2.1.2.

When $z = k$, the basis vector $\mathbf{c}_{k,i}$ has minimum length of $\sqrt{2}d$. At this latitude, $\mathbf{c}_{k+1,i}$ and $\mathbf{c}_{k-1,i}$ form the next most dominant spirals and have length $\sqrt{3}d$. For $z = k+1/2$, $\mathbf{c}_{k,i}$ and $\mathbf{c}_{k+1,i}$ are equally dominant and have grid length $\sqrt[4]{5}d$. For a fixed latitude $\phi \neq \pm\pi/2$, z increases with N. Points around ϕ will form a locally rectangular grid. Thus the separation approaches $\sqrt{2}d$ which occurs when $z = k$ and the largest hole in the triangulation around x_i will be at most $\sqrt[4]{5}d/\sqrt{2}$ which occurs when $z = k \pm 1/2$. Thus off the poles, $\delta(\omega_{2N+1}) \geq \sqrt{8\pi\sqrt{5}}/\sqrt{N}$ and $\eta(\omega_{2N+1}) \leq \sqrt{2\pi/N}$.

Indeed, these inequalities hold for large zone numbers z where $F_k \approx \varphi^k/\sqrt{5}$ holds. However, on the polar points, x_1 and x_N, the zone number

$$z = \frac{\log((2N+1)\pi\sqrt{5}(1-4N^2/(2N+1)^2))}{\log\varphi^2} \to \frac{\log(2\pi\sqrt{5})}{\log\varphi^2} = 2.75..., \quad N \to \infty$$

and writing $\mathbf{c}_{k,i}$ in the form of equation (2.7) for small k overestimates the length of the vector. Using equation (2.6) and noticing that $k-1/2 \leq z \leq k+1/2$ implies

$$\frac{\varphi^{2k-1}}{(2N+1)\pi\sqrt{5}} \leq \cos^2\phi \leq \frac{\varphi^{2k+1}}{(2N+1)\pi\sqrt{5}},$$

we have

$$|\mathbf{c}_{k,i}|^2 \geq \frac{4\pi^2\varphi + 20\pi F_k^2\varphi^{-2k+1}}{(2N+1)\pi\sqrt{5}} = O\left(\frac{1}{2N+1}\right), \quad k-1/2 \leq z \leq k+1/2.$$

Since $|\mathbf{c}_{k,i}|$ is the minimal separation distance for $k-1/2 \leq z \leq k+1/2$, we have the correct order of separation on $\mathbb{S}^2$. By a similar computation, we have the upper bound

$$|\mathbf{c}_{k,i}| \leq O\left(\frac{1}{\sqrt{2N+1}}\right), \qquad k-3/2 \leq z \leq k+3/2.$$

Since the triangulation of ω_{2N+1} in each zone consists of $\mathbf{c}_{k,i}$, $\mathbf{c}_{k-1,i}$, and $\mathbf{c}_{k+1,i}$, the covering of ω_{2N+1} is of the correct order on all of $\mathbb{S}^2$. □

Proof of Proposition 2.3.1.

The diameter boundedness of the partition and Proposition 2.9.1 gives equidistribution and covering,

$$\eta(\omega_N) \leq \frac{3.5}{\sqrt{N}}.$$

In [64] and [107], it is established that there exists $c_1, c_2 > 0$ such that for all partitions P_N, with ϕ_j, n as defined above,

$$\frac{c_1}{\sqrt{N}} \leq \phi_{j+1} - \phi_j \leq \frac{c_2}{\sqrt{N}}, \qquad 0 \leq j \leq n. \tag{2.21}$$

This gives the correct order of separation between collars. For neighbors $x_1, x_2 \in \omega_N$ within collar j, wlog suppose $\phi_j < \pi/2$. Using the fact that the normalized area of each cell can be expressed as

$$\frac{(\cos\phi_j - \cos\phi_{j+1})}{2y_i} = \frac{1}{N},$$

we have

$$\|x_1 - x_2\| \geq \frac{2\pi \sin\phi_j}{y_i} = \frac{4\pi \sin\phi_j}{N(\cos\phi_j - \cos\phi_{j+1})}.$$

So it suffices to show there exists $c_3 > 0$ such that

$$\frac{\sin\phi_j}{\cos\phi_j - \cos\phi_{j+1}} \geq c_3\sqrt{N} \qquad \forall N, 0 \leq j \leq n. \tag{2.22}$$

For a fixed $h > 0$ and $\phi_j \geq h$, this follows from (2.21) and the fact that cosine is Lipschitz. On the other hand, for sufficiently small ϕ_j, there exists $c_4 > 0$ such that

$$\frac{\sin\phi_j}{\cos\phi_j - \cos\phi_{j+1}} \geq c_4 \frac{\phi_j}{\phi_j^2 - \phi_{j+1}^2}.$$

Again applying (2.21) twice,

$$\text{RHS } (2.22) \geq \frac{c_4}{c_1}\frac{\phi_j}{\phi_j + \phi_{j+1}}\sqrt{N} \geq \frac{c_4}{c_1}\frac{\phi_j}{2\phi_j + \frac{c_2}{\sqrt{N}}}\sqrt{N} \geq c_3\sqrt{N}.$$

In the last step we used the fact that for some $c_5 > 0$ and all j

$$\phi_j \geq \cos^{-1}(1 - \frac{2}{N}) \geq \frac{c_5}{\sqrt{N}}.$$

□

Proof of Proposition 2.3.2.

The pixels are diameter bounded and thus by Proposition 2.9.1 the nodes are equidistributed.

To establish separation, we examine the five cases of nearest neighbor points: The points lie in 1) the polar region or 2) the equatorial region, and the points lie in a) the same ring or b) adjacent rings, and 3) the points lie in adjacent rings at the boundary of the polar region and the equatorial region.

Case 1a: If nearest neighbor points lie in the polar region along the same ring $1 \leq i \leq k$ that has radius

$$r_i = \sin\phi_i = \sqrt{\frac{2i^2}{3k^2} - \frac{i^4}{9k^4}}$$

and $4i$ equally spaced points, then the separation δ satisfies

$$\delta = 2r_i \sin\frac{\pi}{4i} = 2\sqrt{\frac{2i^2}{3k^2} - \frac{i^4}{9k^4}}\sin\frac{\pi}{4i} \geq \frac{\sqrt{2}}{i}\sqrt{\frac{2i^2}{3k^2} - \frac{i^4}{9k^4}} = O\left(\frac{1}{k}\right) = O\left(\frac{1}{\sqrt{N}}\right).$$

In the middle inequality we use the fact that

$$\sin x \geq \frac{\sqrt{2}/2}{\pi/4} x \qquad 0 \leq x \leq \pi/4. \tag{2.23}$$

Case 2a: Suppose the nearest neighbor points lie in the equatorial region along the same ring. Since each ring has $4k$ points, the smallest separation occurs at the ring farthest from the equator and closest to $z = 2/3$. Using (2.23) again, we have

$$\delta = 2r_i \sin\frac{\pi}{4k} \geq \frac{2\sqrt{5}}{3}\sin\frac{\pi}{4k} \geq \frac{\sqrt{10}}{3k} = O\left(\frac{1}{\sqrt{N}}\right).$$

Case 1b: We split up the rings in the polar region into the outer half, $1 \leq i \leq k/2$ and the inner half, $k/2 \leq i \leq k$. On the outer half, the separation between rings is

$$\begin{aligned}\delta \geq r_{i+1} - r_i =& \frac{(i+1)\sqrt{6k^2-(i+1)^2} - i\sqrt{6k^2-i^2}}{3k^2} \\ \geq& \frac{(k/2+1)\sqrt{6k^2-(k/2+1)^2} - (k/2)\sqrt{6k^2-(k/2)^2}}{3k^2} = O\left(\frac{1}{\sqrt{N}}\right).\end{aligned}$$

On the inner polar rings, the separation between rings is

$$\delta \geq |\cos\phi_{i+1} - \cos\phi_i| = \frac{2i+1}{3k^2} \geq \frac{k+1}{3k^2} = O\left(\frac{1}{\sqrt{N}}\right).$$

Case 2b: In the equatorial region, the ring height z increases linearly with respect to the index i giving

$$\delta \geq \frac{2}{3k} = O\left(\frac{1}{\sqrt{N}}\right).$$

Case 3 follows from Case 1b and 2b.

The covering of the points follows by similar geometric arguments. □

Proof of Proposition 2.4.1.

It suffices to show Π is locally bi-Lipschitz on each face $\mathcal{F}$ of the icosahedron. If for some $\delta, L_1, L_2 > 0$

$$L_1|x-y| \le |\Pi(x)-\Pi(y)| \le L_2|x-y|, \quad x,y \in \mathcal{F},\ |x-y| < \delta,$$

then

$$\gamma(\omega_N) \le \frac{L_2}{L_1}\gamma(\widetilde{\omega_{N_k}}) = \frac{L_2}{L_1\sqrt{3}}.$$

Let $c := \min_{x\in \mathrm{Icos}} |x| = \sqrt{(1/3+2\sqrt{5}/15)}$. For $x,y \in \mathcal{F}$ with angle θ, we have

$$|x-y| \ge 2c\sin\frac{\theta}{2}.$$

Using the fact that $\sin^{-1} x \le \frac{\pi}{2}x$ for $x \le 1$ and $|x-y| < 2c$,

$$|\Pi(x)-\Pi(y)| \le \theta \le 2\sin^{-1}\left(\frac{|x-y|}{2c}\right) \le \pi c|x-y|.$$

For the other inequality, wlog suppose $c \le |x| \le |y| \le 1$, and consider the line $P \subset \mathcal{F}$ connecting x and y. Denote z as the projection of 0 onto P. Defining $\phi := \cos^{-1}(|z|/|x|)$, we have

$$|y|-|x| = |z|\sec(\theta+\phi) - |z|\sec\phi \le \sec(\theta+\phi) - \sec\phi.$$

Since $\phi \le \cos^{-1} c - \theta$ and secant is convex on $(0,\pi/2)$,

$$|y|-|x| \le \frac{1}{c} - \sec(\cos^{-1} c - \theta) =: g(\theta).$$

Thus,

$$|x-y|^2 = |x|^2+|y|^2-2|x||y|\cos\theta \le \max_{c\le|y|\le 1}(|y|+g)^2+|y|^2-2|y|(|y|+g)\cos\theta$$
$$= (1+g)^2+1-2(1+g)\cos\theta.$$

Since

$$f(\theta) := \frac{(1+g)^2+1-2(1+g)\cos\theta}{2-2\cos\theta}$$

is continuous for $\theta \in (0, \pi/2+\cos^{-1}c)$ and $\lim_{\theta\to 0} f(\theta)$ exists, there exists $L>0$ such that

$$|x-y| \le L|\Pi(x)-\Pi(y)|, \qquad \theta \in (0, \pi/2+\cos^{-1}c).$$

□

Proof of Theorem 2.4.2. Restricting ourselves to the face of $\mathbb{K}$ with all positive coordinates, label the vertices of the partition $\{A_{i,j}\}_{0\le i+j\le k}$ by

$$A_{i,j} = \left(\frac{iL}{k\sqrt{2}}, \frac{jL}{k\sqrt{2}}, \frac{L}{\sqrt{2}}\left(1-\frac{i+j}{k}\right)\right).$$

Let $\mathcal{A}_{i,j} = \mathcal{U}(A_{i,j})$. Then

$$\mathcal{A}_{i,j} = \left(\frac{i+j}{k}\sqrt{2-\frac{(i+j)^2}{k^2}}\cos\frac{\pi j}{2(i+j)}, \frac{i+j}{k}\sqrt{2-\frac{(i+j)^2}{k^2}}\sin\frac{\pi j}{2(i+j)}, 1-\frac{(i+j)^2}{k^2}\right).$$

Then

$$\delta(\omega_N) = \min_{i,j}\{\|\mathcal{A}_{i+1,j}-\mathcal{A}_{i,j}\|, \|\mathcal{A}_{i,j+1}-\mathcal{A}_{i,j}\|, \|\mathcal{A}_{i+1,j}-\mathcal{A}_{i,j+1}\|\}. \tag{2.24}$$

Adapting [58], we have

$$\|\mathcal{A}_{i+1,j}-\mathcal{A}_{i,j}\|^2 = 2\frac{(i+j+1)^2}{k^2}+2\frac{(i+j)^2}{k^2}-2\frac{(i+j+1)^2(i+j)^2}{k^4}$$

$$-2\frac{(i+j)(i+j+1)}{k^2}\sqrt{2-\frac{(i+j+1)^2}{k^2}}\sqrt{2-\frac{(i+j)^2}{k^2}}\cos\frac{\pi j}{2(i+j)(i+j+1)}.$$

Along the line $i+j=c$, the minimum is obtained when the cosine term is maximized, i.e. at $j=0$. Thus

$$\min_{i,j}\|\mathcal{A}_{i+1,j}-\mathcal{A}_{i,j}\|^2 = \min_{0\le i\le k}\|\mathcal{A}_{i+1,0}-\mathcal{A}_{i,0}\|^2$$

$$=\frac{2}{k^2}\min_{0\le i\le k}\left((i+1)^2+i^2+\frac{(i+1)^2i^2}{k^2}-i(i+1)\sqrt{2-\frac{(i+1)^2}{k^2}}\sqrt{2-\frac{i^2}{k^2}}\right)=\frac{2}{k^2}.$$

By symmetry of the above expressions in i and j,

$$\min_{i,j}\|\mathcal{A}_{i,j+1}-\mathcal{A}_{i,j}\|^2 = \min_{0\le j\le k}\|\mathcal{A}_{0,j+1}-\mathcal{A}_{0,j}\|^2=\frac{2}{k^2}.$$

Lastly,

$$\|\mathcal{A}_{i+1,j}-\mathcal{A}_{i,j+1}\|^2 = 4\frac{(i+j+1)^2}{k^2}\left(2-\frac{(i+j+1)^2}{k^2}\right)\sin^2\frac{\pi}{4(i+j+1)}$$

which again depends on only $i+j$. Using (2.23) we have

$$\begin{aligned}
\min_{i,j} \|\mathcal{A}_{i+1,j} - \mathcal{A}_{i,j+1}\|^2 &= \min_{0\le i\le k} \|\mathcal{A}_{i+1,0} - \mathcal{A}_{i,1}\|^2 \\
&= 4 \min_{0\le i\le k} \frac{(i+1)^2}{k^2}\left(2 - \frac{(i+1)^2}{k^2}\right) \sin^2 \frac{\pi}{4(i+1)} \\
&\ge 4 \min_{0\le i\le k} \frac{(i+1)^2}{k^2}\left(2 - \frac{(i+1)^2}{k^2}\right) \frac{1}{2(i+1)^2} \\
&= 4 \min_{0\le i\le k} \frac{1}{2k^2}\left(2 - \frac{(i+1)^2}{k^2}\right) = \frac{2}{k^2}\left(2 - \frac{(k+1)^2}{k^2}\right).
\end{aligned}$$

Thus from (2.24)

$$\delta(\omega_{4k^2+2})^2 \ge \frac{2}{k^2}\left(2 - \frac{(k+1)^2}{k^2}\right).$$

Taking the square root and substituting $N = 4k^2+2$ gives

$$\liminf_{N\to\infty} \delta(\omega_N)\sqrt{N} \ge \sqrt{8}.$$

Finally, the diameter bound in [58] gives an immediate upper bound for the covering radius from which (2.11) follows:

$$\eta(\omega_{4k^2+2}, \mathbb{S}^2) \le \sqrt{\frac{4+\pi^2}{8k^2}}.$$

□

Proof of Proposition 2.4.3.

If $x = m^2 + mn + n^2$, we call x *representable* by (m,n). Let $U \subset \mathbb{N}$ be the set of representable numbers. We adapt an argument of Leveque for the density of numbers which are the sum of two squares. See for example [69], Section 7.5. First we establish that U is

closed under multiplication and division: We have the identity

$$(m^2+mn+n^2)(l^2+lk+k^2) = (nk-ml)^2+(nk-ml)(mk+nl+ml)+(mk+nl+ml)^2. \tag{2.25}$$

If $x = m^2+mn+n^2$ and $y = l^2+lk+k^2$ is prime with $y|x$, the identity

$$k^2(m^2+mn+n^2) - m^2(l^2+lk+k^2) = (nk-ml)(mk+nl+ml) \tag{2.26}$$

implies y must divide either $nk-ml$ or $mk+nl+ml$. By equation (2.25), y must also divide the other term. Thus,

$$\frac{m^2+mn+n^2}{l^2+lk+k^2} = \left(\frac{nk-ml}{l^2+lk+k^2}\right)^2 + \frac{(nk-ml)(mk+nl+ml)}{(l^2+lk+k^2)^2} + \left(\frac{mk+nl+ml}{l^2+lk+k^2}\right)^2$$

and $x/y \in U$. Now, if $x \in U, z \notin U$ and $z|x$, then x/z must contain a prime factor which is also not in U. Otherwise, writing

$$x = zp_1 \cdots p_k$$

with $p_i \in U$ prime, repeated application of the prior step yields $z \in U$. Finally, if x is representable by (m,n) coprime, then every factor of x is representable. We prove this by infinite descent. Let $q|x$, write

$$m = aq \pm c \qquad n = bq \pm d$$

where $c,d \leq q/2$. Then

$$x = m^2+mn+n^2 = Aq + c^2 \pm cd + d^2$$

for some integer A and thus q divides $c^2 \pm cd + d^2$. Say $qr = c^2 \pm cd + d^2$. If c,d are

coprime, then

$$qr = c^2 \pm cd + d^2 \leq \left(\frac{q}{2}\right)^2 + \left(\frac{q}{2}\right)^2 + \left(\frac{q}{2}\right)^2 = \frac{3q^2}{4}.$$

If q is not representable, then by the previous step r has a factor s that is not representable, and $s < q$. Repeating the same procedure leads to an infinite descent, and thus $q \in U$ by contradiction. If $\gcd(c,d) = g \neq 1$, then g and x must be coprime because $\gcd(g,x)$ must divide m and n. Thus $g^2|r$ and we can write $qs = e^2 \pm ef + f^2$ with e, f coprime and proceed as before.

It is easy to check on a case by case basis that for any (m,n), $x = m^2 + mn + n^2 \equiv 1,3,4 \pmod 6$. From the previous step, if $p \equiv 2,5 \pmod 6$, and $p|x$, then $p^2|x$. Combining the above we have shown if $x \in U$, the prime factorization of x has the form

$$x = 2^{2p} 3^q \alpha_1^{2a_1} \cdots \alpha_k^{2a_k} \beta_1^{b_1} \cdots \beta_l^{b_l}, \quad p,q,a_i,b_j \in \mathbb{N}, \tag{2.27}$$

$$\alpha_i \equiv 5 \pmod 6, \qquad \beta_j \equiv 1 \pmod 6.$$

By the Prime Number Theorem for arithmetic progressions [94], the density of numbers whose prime factorization is of the form in (2.27) is the same as those of the form

$$x = 2^{p} \alpha_1^{2a_1} \cdots \alpha_k^{2a_k} \beta_1^{b_1} \cdots \beta_l^{b_l}, \quad p,a_i,b_j \in \mathbb{N}, \tag{2.28}$$

$$\alpha_i \equiv 3 \pmod 4, \qquad \beta_j \equiv 1 \pmod 4.$$

This is precisely the characterization of numbers that are the sum of two squares whose density is known from [69] Theorem 7.28 to be $O(N/\sqrt{\log N})$. Thus (2.12) holds. □

Proof of Theorem 2.4.4.

We use the fact that

$$\min_{\substack{z\in\mathcal{I}\\ \mathbf{v}\in\mathbb{S}^1}} ||D_\Phi(z)\cdot\mathbf{v}||\cdot||x-y|| \le ||\Phi(x)-\Phi(y)|| \le \max_{\substack{z\in\mathcal{I}\\ \mathbf{v}\in\mathbb{S}^1}} ||D_\Phi(z)\cdot\mathbf{v}||\cdot||x-y||$$

where $D_\Phi(z=(h,w))$ is the Jacobian of Φ. Thus

$$\gamma(\omega_{m,n}) \le \frac{\max_{(z,\mathbf{v}\in\mathcal{I}\times\mathbb{S}^1)} ||D_\Phi(z)\cdot\mathbf{v}||}{\min_{(z,\mathbf{v}\in\mathcal{I}\times\mathbb{S}^1)} ||D_\Phi(z)\cdot\mathbf{v}||}\tilde{\gamma}_{m,n} \tag{2.29}$$

where $\tilde{\gamma}_{m,n} = 1/\sqrt{3}$ is the mesh ratio of the CK configurations on $\mathcal{I}$. Due to symmetry it suffices to restrict Φ to the fixed triangle $\mathcal{R}_i$ on which Φ is derived in Section 2. Orienting $\mathcal{I}$ such that $\Phi(\mathcal{O}) = (0,0,1)$ and $\Phi(h,0)$ lies in the xz-plane, the point $\Phi(h,w)$ will be at the intersection of the meridian λ and the great circle in the yz-plane rotated around the y-axis by an angle of g where $\cos g = 2\cos\psi/\sqrt{3}$ (see Figure 2.14). Solving for Euclidean coordinates,

$$\Phi(h,w) = \begin{bmatrix} \sin\xi\cos\lambda \\ \sin\xi\sin\lambda \\ \cos\xi \end{bmatrix},$$

where $\tan\xi = \tan g/\cos\lambda$. Thus for $(h,w)\neq(0,0)$,

$$D_\Phi(h,w) = \begin{bmatrix} \cos\lambda\cos\xi\frac{\partial\xi}{\partial h} - \sin\xi\sin\lambda\frac{\partial\lambda}{\partial h} & \cos\lambda\cos\xi\frac{\partial\xi}{\partial w} - \sin\xi\sin\lambda\frac{\partial\lambda}{\partial w} \\ \sin\lambda\cos\xi\frac{\partial\xi}{\partial h} + \sin\xi\cos\lambda\frac{\partial\lambda}{\partial h} & \sin\lambda\cos\xi\frac{\partial\xi}{\partial w} + \sin\xi\cos\lambda\frac{\partial\lambda}{\partial w} \\ -\sin\xi\frac{\partial\xi}{\partial h} & -\sin\xi\frac{\partial\xi}{\partial w} \end{bmatrix},$$

$$\lim_{(h,w)\to(0,0)} D_\Phi(h,w) = \begin{bmatrix} 1 & 0 \\ 0 & 1 \\ 0 & 0 \end{bmatrix}.$$

The quantities in (2.29) were optimized algebraically using Mathematica. The minimum

of $||D_\Phi(h,w)\cdot \mathbf{v}||$ occurs at $(h,w) = (a/(2\sqrt{3}), a/2)$, the vertex shared by $\mathcal{R}_i$ and $\mathcal{F}$, and equals 0.828499.... The maximum of $||D_\Phi(h,w)||$ equals 1.14563... and occurs at $(h,w) = (a/(2\sqrt{3}), 0)$. Combining the above, we have

$$\gamma(\omega_{m,n}) \leq \frac{1.14563}{0.828499\sqrt{3}} \approx 0.798...$$

□

CHAPTER 3

NODE GENERATION ON OTHER MANIFOLDS

In this chapter we describe and numerically analyze algorithms for quasi-uniform point generation on the torus $\mathbb{T}$ and the sphere $\mathbb{S}^3 \subset \mathbb{R}^4$ as well as develop a general program for generating quasi-uniform points on a domain $\Omega \subset \mathbb{R}^3$ with variable density given by a prescribed local node separation function $\rho : \Omega \to \mathbb{R}^+$. The latter is particularly useful to radial basis function methods in atmospheric modeling. Section 3.3 is based on the paper [79]

3.1 Torus Configurations

A torus $\mathbb{T} = \mathbb{T}(R,r)$ is defined parametrically by

$$x(\theta,\phi) = (R + r\cos\phi)\cos\theta, \tag{3.1}$$

$$y(\theta,\phi) = (R + r\cos\phi)\sin\theta, \tag{3.2}$$

$$z(\theta,\phi) = r\sin\phi, \tag{3.3}$$

where R is the distance from the center of the torus to the center of the tube, r is the radius of the tube, and R/r is the aspect ratio. To create equidistributed nodes we define an area preserving map $\Lambda_{\mathbb{T}} : [0,1)^2 \to \mathbb{T}$ analogous to the Lambert cylindrical equal area projection onto $\mathbb{S}^2$ defined in (2.4). The map $\Lambda_{\mathbb{T}}$ will identify both pairs of opposing edges of the square, so the initial point configuration on $[0,1)^2$ must be 1-periodic in both the x and y coordinates. Thus we take the Fibonacci nodes on $[0,1)^2$ defined on the rational lattice given in (2.5) with total points F_k. Define $\Lambda_{\mathbb{T}}(x,y) := (\phi,\theta)$ where $\theta = 2\pi x$ as in the Lambert projection. Letting $h = (\pi R - 2r)/4\pi R$, then $-\pi \le \phi \le \pi$ is defined implicitly

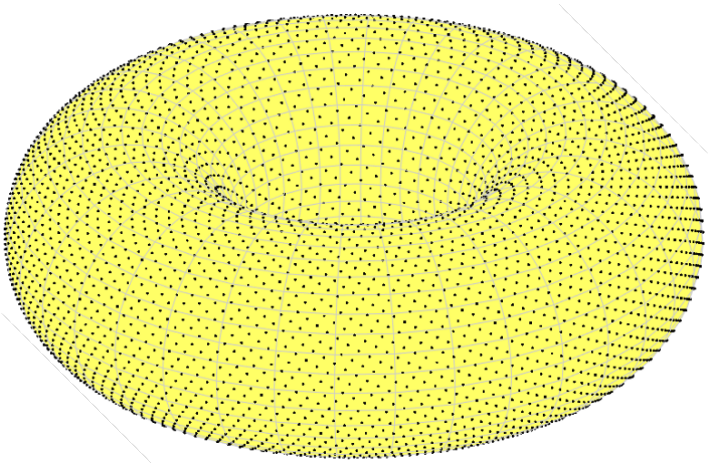

Figure 3.1: 6765 equidistributed Fibonacci torus nodes

$$\begin{aligned} R(\pi-\phi)-r\sin(\phi) &= 2\pi Ry, && 0 \le y < h \\ R\phi + r\sin\phi &= 2\pi R(1/2-y), && h \le y < 1-h \\ R(\pi+\phi)-r\sin(\phi) &= 2\pi R(1-y), && 1-h \le y \le 1 \end{aligned}$$

which is well defined because $f(t) := Rt \pm r\sin t$ maps $[0,\pi/2]$ onto $[0,(R\pi \pm 2r)/2]$ bijectively when $R > r$ and is continuous and monotonic with respect to y. The regions $0 \le y < h$ and $1-h < y \le 1$ are mapped to the regions of $\mathbb{T}$ of negative curvature while the region $h < y < 1-h$ is mapped to the positive curvature part. The lines $y = h$ and $y = 1-h$ are mapped to the boundary circles between the positive and negative curvature areas of $\mathbb{T}$. The map $\Lambda_{\mathbb{T}}$ is an area preserving projection because the area of a rectangular patch $A = [\phi_1,\phi_2]\times[\theta_1,\theta_2]$, $0 \le |\phi_1| \le |\phi_2| \le \pi$ is

$$\sigma_{\mathbb{T}}(A) = 2\pi r(\theta_2-\theta_1)\cdot \begin{cases} R|\phi_1-\phi_2| - r|\sin\phi_1 - \sin\phi_2|, & |\phi_1|,|\phi_2| \ge \pi/2 \\ R(\phi_1-\phi_2) + r(\sin\phi_1 - \sin\phi_2), & |\phi_1| < \pi/2, \phi_2 < -\pi/2 \\ R(\phi_2-\phi_1) + r(\sin\phi_2 - \sin\phi_1), & |\phi_1| < \pi/2, \phi_2 \ge \pi/2 \\ R|\phi_1-\phi_2| + r|\sin\phi_1 - \sin\phi_2|, & |\phi_1|,|\phi_2| < \pi/2 \end{cases}$$

Thus if $\Lambda_{\mathbb{T}}(x_1, y_i) = (\phi_i, \theta_i),\ i = 1, 2$, as can be verified in each case

$$|x_1 - x_2| \cdot |y_1 - y_2| = \frac{\sigma_{\mathbb{T}}(A)}{4\pi^2 Rr}.$$

Unlike the Lambert projection onto the sphere, $\Lambda_{\mathbb{T}}$ is bi-Lipschitz. Indeed, it is enough to bound the Jacobian

$$D_{\Lambda_{\mathbb{T}}}(x, y) = 2\pi \cdot \begin{bmatrix} -\sin\theta(R + r\cos\phi) & \frac{-Rr\sin\phi}{R+r\cos\phi} \\ \cos\theta(R + r\cos\phi) & \frac{-Rr\sin\phi}{R+r\cos\phi} \\ 0 & \frac{-Rr\cos\phi}{R+r\cos\phi} \end{bmatrix},$$

Minimizing along the columns of $D_{\Lambda_{\mathbb{T}}}$, and using the fact that for a matrix $B = [b_{ij}]$,

$$\|B\|_2 \leq (\sum_{i,j} |b_{ij}|^2)^{1/2}$$

it follows that

$$\begin{aligned} 4\pi^2 \min\left\{(R-r)^2, \left(\frac{Rr}{R-r}\right)^2\right\} &\leq \min_{(x,y)\in[0,1)^2} \|D_{\Lambda_{\mathbb{T}}}(x, y)\|_2^2 \\ &\leq \max_{(x,y)\in[0,1)^2} \|D_{\Lambda_{\mathbb{T}}}(x, y)\|_2^2 \leq 4\pi^2 \left[(R+r)^2 + \left(\frac{2Rr}{R+r}\right)^2\right]. \end{aligned}$$

Thus the Fibonacci nodes on the torus are quasi-uniform. For certain aspect ratios, the map $\Lambda_{\mathbb{T}}$ is almost a local isometry. For $R = 3,\ r = 2$, we computed the mesh ratios for $F_k \leq F_{25} = 75025$ and numerically determined

$$\gamma(\omega_{F_k}) \leq 1.0554\sqrt{2}/2 \approx 0.7463...$$

where $\sqrt{2}/2$ is the mesh ratio for the Fibonacci lattice on $[0, 1)$.

3.2 Configurations on $\mathbb{S}^3$

The 600−cell is a 4 dimensional regular convex polytope consisting of 120 vertices, 600 regular tetrahedra and each edge is common to five tetrahedra. The vertices are given by the Cartesian axes $\pm e_i$, vectors of the form

$$(\pm 1/2, \pm 1/2, \pm 1/2, \pm 1/2),$$

and lastly by taking even permutations of

$$1/2(\pm\varphi, \pm 1, \pm 1/\varphi, 0).$$

where $\varphi = (1+\sqrt{5})/2$ is the golden ratio. The 600-cell is a universally optimal configuration in the sense of Cohn and Kumar [35], that is, it minimizes the K energy for 120 points on $\mathbb{S}^3$ for any continuous and completely monotonic potential K.

We generate a sequence of configurations ω_{N_k} in each cell of the 600-cell and then radially project to the sphere, In each tetrahedron, we place an FCC lattice parallel to the faces. Let T be a tetrahedral cell with a vertex at the origin and remaining vertices given by the columns of

$$A = \begin{bmatrix} 1 & \frac{1}{2} & \frac{1}{2} \\ 0 & \frac{\sqrt{3}}{2} & \frac{\sqrt{3}}{6} \\ 0 & 0 & \sqrt{\frac{2}{3}} \end{bmatrix}$$

Then the configurations are given by

$$x_{m,n,p} = \frac{1}{k} A \cdot [m,n,p]^T, \qquad m,n,p = 1,\ldots,k.$$

followed by scaling and translating to each cell of the 600-cell. By an inclusion-exclusion argument, we have that $N_k = 100k^3 - 300k^2 + 320k - 120$.

The shortest length vector in a face of the 600-cell has length $L = \sqrt{2}/8(3+\sqrt{5}) = 0.9256...$, and like the radial projection from the icosahedron $\mathbb{S}^2$, the map is bi-Lipschitz and thus the resulting sequence of spherical configurations is quasi-uniform. However it is not equidistributed.

Remark 3.2.1. It is possible to generalize the equal area map from the icosahedron to $\mathbb{S}^2$ given in Section 2.4 to produce an equidistributed sequence of spherical configurations from the 600-cell. Given a regular tetrahedron T of edge length L, we can create an volume preserving map Φ to a regular spherical tetrahedron $\Phi(T)$ in the following way:

1. Label the vertices of T by x_i. Prescribe the vertices $\Phi(x_i)$ such that they form a regular spherical tetrahedron of equal volume to T.

2. The edges of T will be mapped to the corresponding geodesics between $\Phi(x_i)$.

3. For a fixed $h \leq L$, denote by $v_i \in T$, $i = 1,2,3$ the points along the edges between x_4 and x_i of Euclidean distance h to x_4. Let $A(h)$ be the volume of the tetrahedron formed by $\{v_1, v_2, v_3, x_4\}$. Similarly on the sphere, let $\tilde{v}_i$ be the points along the geodesics connecting $\Phi(x_4)$ to $\Phi(x_i)$ with geodesic distance h to $\Phi(x_4)$, and let $B(h)$ denote the volume of the spherical tetrahedron formed by $\{\tilde{v}_1, \tilde{v}_2, \tilde{v}_3, \Phi(x_4)\}$. Formulae for the volume of spherical tetrahedra in terms of edge lengths are given in [60].

4. Both $A(\cdot)$ and $B(\cdot)$ are continuous and strictly monotonic with $A(0) = B(0) = 0$ and $A(L) = B(\tilde{L}) = \mathcal{H}_3(T)$ where $\tilde{L}$ is the geodesic edge length of $\Phi(T)$. Thus for each $0 \leq h \leq L$, there exists a unique $0 \leq \tilde{h} \leq \tilde{L}$ such that $A(h) = B(\tilde{h})$.

5. For $0 \leq h \leq L$ and $v_i \in T$, $i = 1,2,3$ as described in Step 3, define $\Phi(v_i)$ to be the points along the geodesics between $\Phi(x_i)$ and $\Phi(x_4)$ corresponding to the $\tilde{h}$ in Step 4.

6. Apply the equal area map described in Section 2.4 between the cross sectional equilateral triangle $\{v_1, v_2, v_3\}$ to the cross sectional equilateral spherical triangle $\{\Phi(v_1), \Phi(v_2), \Phi(v_3)\}$.

Determining the formulas for this map and proving they result in a sequence of equidistributed and quasi-uniform configurations on $\mathbb{S}^3$ is an open problem.

3.3 Variable Density Node Generation in $\mathbb{R}^d$

3.3.1 Radial basis functions

We now turn our attention to generating nodes specifically for Radial Basis Function (RBF) modeling whose usefulness is well-known in a number of applications. They have found their way into high-dimensional interpolation, machine learning, spectral methods, vector-valued approximation and interpolation, just to name a few [103], [29], [46], [25], [87]. RBFs have a number of advantages, most importantly extreme flexibility in forming stencils (in the case of RBF-FD) and high local adaptivity; allowing spectral accuracy on irregular domains; the fact that the corresponding interpolation matrix (denoted by A below) is positive-definite for several types of radial functions and does not suffer from instability phenomena characteristic of some of the alternative interpolation methods.

Applying RBF-FD stencils to building solvers requires an efficient way of distributing the centers of basis elements in the domain, which can be either a solid or a surface. The tasks of modeling and simulation often call for distribution of massive numbers of RBF centers, so it is important to ensure that the distribution process is easily scalable. One further has to be able to place nodes according to a certain non-uniform density.

An RBF [47] is a linear combination of the form

$$s(x) = \sum_{k=1}^{N} \lambda_k \phi(\|x - x_k\|), \tag{3.4}$$

where $\phi(\cdot)$ is a radial function, and $\{x_k\}_{k=1}^N$ is a collection of pairwise distinct points in $\mathbb{R}^d$. A common choice of ϕ is the Gaussian $e^{-(\varepsilon r)^2}$, although one may also use $1/(1+(\varepsilon r)^2)$, $r^{2m}\log(r), m \in \mathbb{N}$, or any kernel approximating the delta-function [74]. In this discussion, we are not concerned with the distinctions between the different radial kernels.

It is well-known that the matrix

$$A = \begin{bmatrix} \phi(\|x_1 - x_1\|) & \phi(\|x_1 - x_2\|) & \dots & \phi(\|x_1 - x_N\|) \\ \phi(\|x_2 - x_1\|) & \phi(\|x_2 - x_2\|) & \dots & \phi(\|x_2 - x_N\|) \\ \vdots & \vdots & & \vdots \\ \phi(\|x_N - x_1\|) & \phi(\|x_N - x_2\|) & \dots & \phi(\|x_n - x_N\|) \end{bmatrix}$$

is positive-definite if the nodes $x_1 \dots x_N$ are all distinct, and therefore under this assumption there exists an N-point RBF interpolant for any function data which we denote by ω_N. A different question, however, is whether the matrix A will be well-conditioned. This is not the case, for example, when the kernel is Gaussian, the nodes are placed on a lattice and $\varepsilon \to 0$, [49]. It is due to this phenomenon that planar lattice nodes perform much worse than Halton nodes [49], or quasi-uniform nodes. Furthermore, node clumping can lead to instability of PDE solvers, [46]. To avoid this, one must guarantee that the RBF centers are well-separated.

In many applications, one has to ensure that the distance from a node x_i to its nearest neighbor behaves approximately as a function of the position of the node [48]. Prescribing this function, $\rho(x)$, which we call the *radial density*, is a natural way to treat the cases when a local refinement is required in order to capture special features of the domain. We will describe a method of node placement for which the distance to the nearest neighbor, denoted by $\delta_i(\omega_N) = \min_{i \neq j} \|x_i - x_j\|$, satisfies the above description. To summarize, we are interested in a procedure of distributing discrete configurations inside a domain that would:

- guarantee that $\delta_i(\omega_N) \simeq \rho(x_i)$ for a given function $\rho(\boldsymbol{N})$ (that is, they differ only up to a constant factor) for a reasonably wide choice of ρ;
- be suitable for mesh-free PDE discretizations using RBFs, i.e., produce well-separated configurations without significant node alignment;
- result in regular node distribution on the surface boundaries of the domain;

- be computationally efficient, easily scalable, and suitable for parallelization.

3.3.2 Choice of method

To generate nodes both devoid of lattice alignment and having near-optimal local separation, we apply Riesz energy minimization. Furthermore, we consider the *weighted s-energy* which is defined in [15] as

$$E_s(x_1,\dots,x_N) = \sum_{i\neq j} \frac{w(x_i,x_j)}{\|x_i - x_j\|^s}. \tag{3.5}$$

It will be useful to assume that the weight function in (3.5) is chosen so that all the terms are zero except when x_j is among the K nearest nodes to x_i, a condition equivalent to the truncated weights in [16]. As described in detail in [16], when $s > d$, the truncated kernel has the same asymptotics and limiting distribution, and the minimal energy configurations are well-separated. Yet it can be computed in an amount of time of order $O(NK)$, unlike the $O(N^2)$ order computation time for the complete kernel.

We choose $s > d$ to ensure that the energy functional is sufficiently repulsive and the local structure does not depend on the domain Ω. While any symmetric kernel that grows fast enough towards the diagonal of $\Omega \times \Omega$ and smooth away from it would produce similar results, we chose the Riesz kernel because the properties of its minimizers are well understood.

To facilitate convergence of whichever optimization algorithm is used to find minimizers of (3.5), we initialize it with a configuration that approximates the limiting measure. Due to the separation requirement, one has to rule out uses of Monte Carlo method, as random points exhibit clustering [22], and turn instead to the quasi-Monte Carlo (Q-MC) approach.

The key element of our construction lies in distributing the node set in a deterministic way in order to guarantee low discrepancy between the desired and the obtained radial densities. This is achieved by a Q-MC analog of the *stratification* of Monte Carlo method

[26]: nodes are distributed with piecewise constant (radial) density that approximates the desired density. We consider two different Q-MC sequences to draw from with constant radial density: irrational lattices and periodic Riesz minimizers. After dividing the set Ω into cube-shaped *voxels*, each voxel is filled with nodes obtained in one of the two ways, appropriately scaled, then the weighted s-energy of the whole node set is minimized. It is important to observe that, although we discuss the radial density case here, an argument for the volumetric density can be produced along the same lines.

An *irrational lattice* (IL) is defined as a discrete subset of the d-dimensional unit cube $[0,1]^d$

$$\mathcal{L}_N = \left\{ \left(\{\Xi + i/N\}, \{i\alpha_1\}, \{i\alpha_2\}, \ldots, \{i\alpha_{d-1}\} \right) \right\}_{i=1}^{N}, \tag{3.6}$$

where $\{x\} = x - \lfloor x \rfloor$ denotes the fractional part of x, $0 < \Xi < 1$ is fixed, and $\alpha_1, \alpha_2, \ldots, \alpha_{d-1}$ are irrational numbers, linearly independent over the rationals. This terminology seems to be accepted in the low-discrepancy community [8], while closely related objects, when used for Q-MC purposes, are known as *Korobov/lattice point sets* [62].

The motivation for using an IL in this context comes in part from the desire to avoid recursive data structures, which can be detrimental to the overall performance, and in part is motivated by the existing results on the discrepancy of such lattices. It is known for example, that the two-dimensional ILs have optimal order L^2 discrepancy, [8], [9]. Furthermore, in all dimensions ILs are equidistributed [61, Chapter 1.6]. The simple linear structure of ILs makes them especially attractive for SIMD-parallelization.

Another Q-MC sequence that has proven to suit our purposes consists of *periodic Riesz minimizers* on the unit flat torus, that is, energy minimizers on $[0,1]^d$ with the Euclidean distance replaced with the coordinate-wise periodic metric

$$\|[x_1,x_2,x_3] - [y_1,y_2,y_3]\|_{\sim}^2 = \Pi(x_1 - y_1) + \Pi(x_2 - y_2) + \Pi(x_3 - y_3),$$

where $\Pi(t) = \min(t^2, (1-t)^2),\ 0 \le t \le 1$. It follows from [55] that such configurations

are well-separated and equidistributed. From the numerics, the nearest neighbor distances appear to vary little from node to node. This reason and also that minimizing configurations do not suffer from the lattice-like alignment, makes their rescaled copies good candidates for the stratification.

The number of nodes in individual voxels is defined by the function ρ, and the resulting collection has piecewise constant density; refining the voxel partition leads to an improved piecewise approximation of the desired (e.g., smooth) density. In practice, the dependence between the number of nodes contained in the unit cube, and average/minimal nearest neighbor distance is tabulated in advance, and then inverted during the construction of the node set.

3.3.3 The algorithm

If the nodes must be restricted to a certain compact set, for example, support of a given indicator function, we will refer to the set as *density support*. We may assume that the desired node distribution is contained in the d-dimensional unit cube; the case of an arbitrary compact support then follows by choosing a suitable enclosing cube and applying scaling and translation. Suppose the radial density is prescribed by a bounded Lipschitz function $\rho : \mathcal{C} = [0,1]^d \to [0,D]$, so that the distance $\delta_i(\omega_N)$ to the nearest neighbor from a node x_i has to be close to $\rho(x_i)$. We summarize the discussion in Section 3.3.2 into the following algorithm for generating nodes with radial density ρ:

1. Choose one of the two Q-MC sequences described in Section 3.3.2. For a fixed $1 \leq n \leq n_{max}$, place a configuration of n nodes into $[0,1]^d$, and determine the average periodic nearest neighbor distance, denoted by δ_n of the configuration. Let $L : (0,\infty) \to \{0,1,2,\ldots,n_{\max}\}$ be the interpolated inverse to $\delta_n : \{1,2,\ldots,n_{\max}\} \to (0,1]$.[1]

[1] Note that both ILs and the minimizers can have nearest neighbor distance of at most 1, due to periodicity. We therefore take $L(t) = 0$ whenever $t > 1$.

2. Partition $\mathcal{C}$ into N_v^d equal cube-shaped voxels of side length $1/N_v$, with faces parallel to the coordinate planes. The choice of N_v corresponds to the resolution of the piecewise constant density of the resulting distribution.

3. Let $\{\mathcal{V}_j\}_{j=1}^{N_v^d}$ denote the voxels, and let $\bar{\rho}_j$ be the average value of ρ at the 2^d vertices of the voxel $\mathcal{V}_j$. Place inside $\mathcal{V}_j$ a scaled and translated version of (3.6), or of the n-point periodic Riesz minimizer, using $n = n_j$ defined by

$$n_j = L(\bar{\rho}_j N_v).$$

4. Iterate over all the voxels $\{\mathcal{V}_j\}_{j\in\mathcal{J}}$ for which at least one of the adjacent (i.e., sharing a face) voxels has a vertex inside the density support. Apply Step 3 to every such voxel.

5. Consider the voxels in $\{\mathcal{V}_j\}_{j\in\mathcal{J}}$, for which $\bar{\rho}_j N_v > 1$; at this stage they do not contain any nodes. Sort such voxels by increasing values of $\bar{\rho}_j$; iterate over the resulting list, which will be denoted by $\{\mathcal{V}_j\}_{j\in\mathcal{K}}$, and place nodes in the center Z_j of every voxel, for which distance to all the previously placed nodes is greater than $\bar{\rho}_j$. Finally, for all nonempty voxels, remove nodes outside the density support.

6. Perform T iterations of gradient descent on the truncated s-energy functional with $w(x_i,x_j) = \rho(x_i)^s$, $s > d$, using the K nearest neighbors of each node. Let the initial configuration be the 0-th iteration, $\omega_N^{(0)}$. On the t^{th} iteration, given a node $x_i^{(t)}$ with K nearest neighbors $\{x_{i,k}^{(t)}\}_{k=1}^K$, form the weighted vector sum

$$G_i^{(t)} = \sum_{k=1}^{K} \frac{x_i^{(t)} - x_{i,k}^{(t)}}{\|x_i^{(t)} - x_{i,k}^{(t)}\|^{s+2}},$$

the new node position can now be expressed as

$$x_i^{(t+1)} = \begin{cases} x_i^{(t)} + s\dfrac{\delta_i(\omega_N^{(t)})}{t+\Theta}\rho\left(x_i^{(t)}\right)^s \dfrac{G_i^{(t)}}{\|G_i^{(t)}\|} & \text{if this sum in inside } \operatorname{supp}\rho; \\ x_i^{(t)}, & \text{otherwise,} \end{cases} \qquad 1 \le i \le N. \tag{3.7}$$

where Θ is an offset chosen to control the step size between $x_i^{(t)}$ and $x_i^{(t+1)}$. The condition of $x_i^{(t+1)}$ being inside the support is replaced with applying a "pullback" function if one is provided. Update the nearest neighbor structure after every few iterations.

7. If no boundary node set/pullback function is prescribed, define the boundary nodes as follows. Evaluate the point inclusion function for $x_i \pm \delta_i(\omega_N)\boldsymbol{e}_j$ for each $i = 1,\dots,N,\ j = 1,\dots,d$, where $\boldsymbol{e}_j$ is the j-th basis vector. If at least one such point lies outside the density support, the node x_i is considered to be part of the boundary set.

Remark 3.3.1. It doesn't matter which minimization method was applied to the Riesz s-energy in Step 6, rather the gradient descent is chosen due to its simplicity. Note, the second case in (3.7), leading to shrinking of the line stepping distance, can be thought of as a simplistic backtracking line search, and it turns out to be sufficient for our purposes. Furthermore, applying a more involved line search may significantly deplete performance for complicated or nonsmooth domains.

Remark 3.3.2. If the irrational lattice method is chosen in Step 1, than the node set in voxel $\mathcal{V}_j$ is constructed as follows. Let $\boldsymbol{C}_j$ be the vertex of $\mathcal{V}_j$ closest to the origin. Before scaling and translating, randomly permute the coordinates of the lattice by a permutation σ so that the resulting IL in $\mathcal{V}_j$ will be oriented randomly with respect to its neighboring voxels. Then the IL from (3.6) in voxel $\mathcal{V}_j$ becomes

$$\mathcal{L}_j = \boldsymbol{C}_j + \frac{\gamma}{N_v}\sigma(i/n_j, \{i\alpha_1\}, \{i\alpha_2\}, \dots, \{i\alpha_{d-1}\}) + \frac{\boldsymbol{\xi}}{N_v}, \qquad i = 1\dots n_j, \tag{3.8}$$

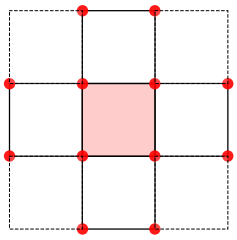

Figure 3.2: The vertices which the algorithm tests to be in the density support.

where

$$\gamma = 1 - c_d \left(\frac{1}{n_{\max}} \right)^{1/d}$$
$$\xi = \frac{1-\gamma}{2} \cdot [1, 1, \ldots, 1]^t,$$

with c_d a constant depending only on the dimension. The quantities γ and ξ ensure that the lattice points in $\mathcal{L}_j$ are inset into the voxel by at least half a minimum separation distance, avoiding poorly separated points along the boundaries between voxels.

Remark 3.3.3. The values of K and T can be adjusted to achieve a trade-off between execution speed/memory consumption and local separation. In practice[2], even relatively small values of K and T produce good results: we used $K \approx T \approx 30$ for 1.3 million nodes in Section 3.3.4.2, and $K \approx T \approx 20$ for about 250 thousand nodes in Section 3.3.4.3.

Remark 3.3.4. Observe that in Step 4 the nodes are only placed in voxels for which neighbors (sharing a face) have corners inside the density support – in other words, for which the radial density function is smaller than a certain threshold value. This means, removing the nodes outside the support in Step 4 does not lead to much overhead, provided the function ρ is varying slow enough. Furthermore, since the density is first evaluated at the corners only, the total number of evaluations may be significantly reduced, which is especially useful when ρ is computationally expensive.

One could equally use a different arrangement of nearby corners to detect whether to count a particular voxel as being inside/outside the support. Figure 3.2 illustrates the one we

[2]The Matlab code we provide performs naive autotuning of K and T, using the total number of nodes to be placed. Although sufficient for demonstration purposes, there is room for improvement.

used in our implementation, for the $d = 2$ case.

Remark 3.3.5. To introduce adaptive refinement of the voxel structure, it suffices to modify Step 3 in the following way.

After computing $\{\bar{\rho}_j\}_{j=1}^{N_v^d}$, detect voxels $\mathcal{V}_j$ for which the node distribution needs to be refined, either because of large density variation, or by some meaningful criterion (coastline, vortex creation, boundary conditions, etc.). Mark the corresponding corners $\boldsymbol{C}_j$ as *refined*; for each refined corner, add $2^d - 1$ new corners, obtained by taking the middles of segments connecting $\boldsymbol{C}_j$ with the other vertices of $\mathcal{V}_j$. Mark the new corners as refined. Proceed as before in Step 3, except for $\mathcal{L}_j$s in (3.8) for the refined corners being scaled with $\gamma' = \gamma/2$.

3.3.4 Sample applications

3.3.4.1 Spherical shell

The motivation for this example comes from atmospheric modeling. Approximating the surface of the Earth by a sphere, we consider first a thin 3-D shell of inner radius a and outer radius $a + ztop$ with separation h between points in the radial (vertical) direction and separation in the tangential (horizontal) direction at radius r to be $k(r) = C \cdot r$ for some constant C. With typical choices of parameters, k will be much larger than h, reflecting the much higher resolution needed in the vertical direction. We make a variable change in the radial direction $R = R(r)$ in order to compute with equal resolution in all spatial directions, the easiest case to implement with RBF-FD. Following this change of variables, the node separations become

$$H(r) = h \cdot R'(r)$$

$$K(r) = R(r) \cdot C$$

Setting these two quantities to be equal, we obtain the ODE

$$R'(r) = R(r) \cdot \frac{C}{h}$$

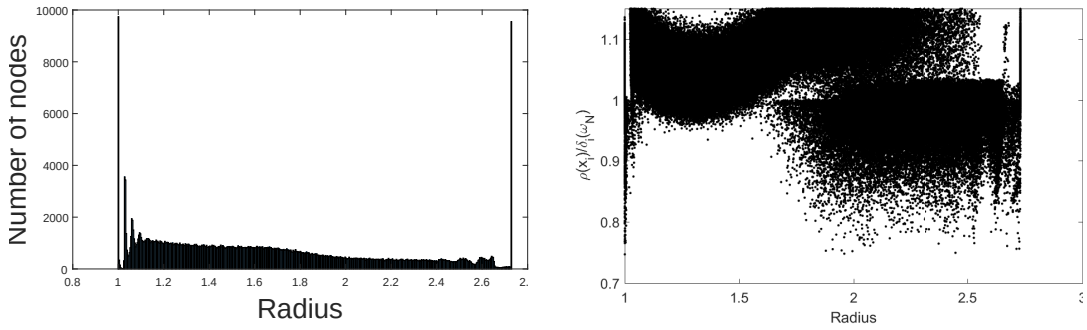

Figure 3.3: Left: Distribution of radii of the spherical shell node set. Right: Ratios of expected separation to nearest neighbor distances.

with initial condition $R(a) = a$, and its solution becomes

$$R(r) = a \exp\left(C \cdot \frac{r-a}{h}\right).$$

We thus generate a node set whose separation is proportional to $R(r)$ and has equal resolution in all dimensions. Letting $a = 6{,}371{,}220$ be the mean radius of the Earth in meters and $ztop = 12{,}000$ we generate 325,003 nodes corresponding to a 2 degree separation on the surface of the Earth and a 400 meter resolution in the vertical direction. On the inner and outer boundary we fix 12,100 approximate Riesz energy minimizers on the sphere. We rescale the configuration so that the inner shell has radius 1.

The left plot of Figure 3.3 plots the number of nodes at each radius. As expected, the distribution follows a roughly exponential decay while the inner and outer nodes are repelled from the fixed boundary nodes. The right plot of Figure 3.3 shows $\rho(x_i)/\delta_i(\omega_N)$ with respect to radius for node x_i. The minimum and maximum values are 0.7468 and 1.1500 respectively with mean 1.0486 and variance 0.0030 which reflects the quality of the density recovery.

3.3.4.2 Atmospheric node distribution using surface data

We use the geodata [2] from the collection[3] of global relief datasets from NOAA (National Oceanic and Atmospheric Administration), which contains a 1 arc-minute resolution model. The sample configuration consists of 1,356,985 nodes distributed uniformly inside an atmospheric-type shell: the outer boundary of the domain is spherical, the inner one is an interpolation of the relief from ETOPO1 data, exaggerated by a factor of 100. The scale is chosen so that the average Earth radius, assumed to be 6,371,220 meters, has unit length; the radius of the outer boundary is 1.1.

The ETOPO1 dataset stores relief as a 21 600-by-10 800 array of heights from the sea level – equivalently, of radial coordinates that correspond to the spherical angles defined by the array's indices. The data points are equispaced on lines of constant azimuth/inclination with angular distance $\delta = \pi/10\,800$. To determine whether a given node x_i belongs to the domain, its radial coordinate r_i was compared with a linear interpolation of the values of radii of three ETOPO points with the nearest spherical coordinates. For example, assume that for $x_i = (r_i, \phi_i, \theta_i)$ the three nearest data points have spherical coordinates $(r_j, \phi_j, \theta_j),\ j = 1,2,3$, where $0 \le \phi \le 2\pi$ and $0 \le \theta \le \pi$ are the azimuth and inclination, respectively, and

$$\begin{aligned} &\phi_1 = \delta l, \quad \phi_2 = \phi_1 + \delta, \qquad \phi_3 = \phi_1, \qquad 0 \le l \le 21\,599; \\ &\theta_1 = \delta m, \qquad \theta_2 = \theta_1, \qquad \theta_3 = \theta_1 + \delta, \quad 0 \le m \le 10\,799. \end{aligned}$$

The other possible arrangements for ϕ_j, θ_j can be treated similarly. The node x_i was deemed to belong to the atmospheric shell if

$$r_1 + \frac{\phi_i - \phi_1}{\delta}(r_2 - r_1) + \frac{\theta_i - \theta_1}{\delta}(r_3 - r_1) < r_i < r_{\text{outer}},$$

with r_{outer} being the radius of the outer sphere as above. In effect, the point inclusion function described here coincides with using the star-shaped point location algorithm from

[3] https://doi.org/10.7289/V5C8276M

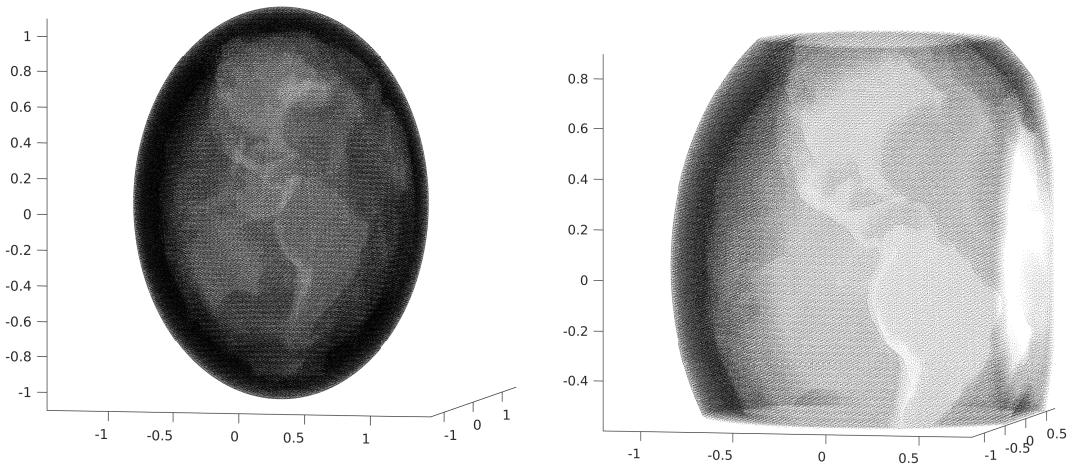

Figure 3.4: Left: a general view of a uniform node distribution in an atmospheric-like shell. Right: zoomed in Americas.

[80, Section 2.2] to verify that x_i lies outside the interpolated Earth surface, and inside the outer sphere.

The time required to select the node configuration inside the domain from a piecewise irrational lattice was 11.78 seconds on an Intel i5 CPU. Performing 30 iterations in Step 6 with the whole 1.3M-node set additionally took 136.07 seconds.

Figure 3.5 illustrates the distribution of nodes close to the surface of the domain. Although there has been no special treatment of the near-surface nodes, they appear to be quite regular. Note that the node spacing is about the same on the continental part (green), as on the slope of Andes going down to the ocean bed (from yellow to blue). This shows that the introduction of a boundary into the algorithm by simply recomputing the point inclusion function in (3.7) did not lead to distribution artifacts.

The left subplot in the Figure 3.6 illustrates the effect of Step 6 on the distribution of distances to the nearest neighbor. On the right, we have collected distances to the nearest neighbors for the whole configuration, and separately for the surface subset. The histogram also contains the distribution of *hole radii*, that is, distances from the Voronoi centers of the present node configuration to their respective nearest nodes. It is a well-known fact that the Voronoi centers are local maxima of the distance from the node set [36], considered as a

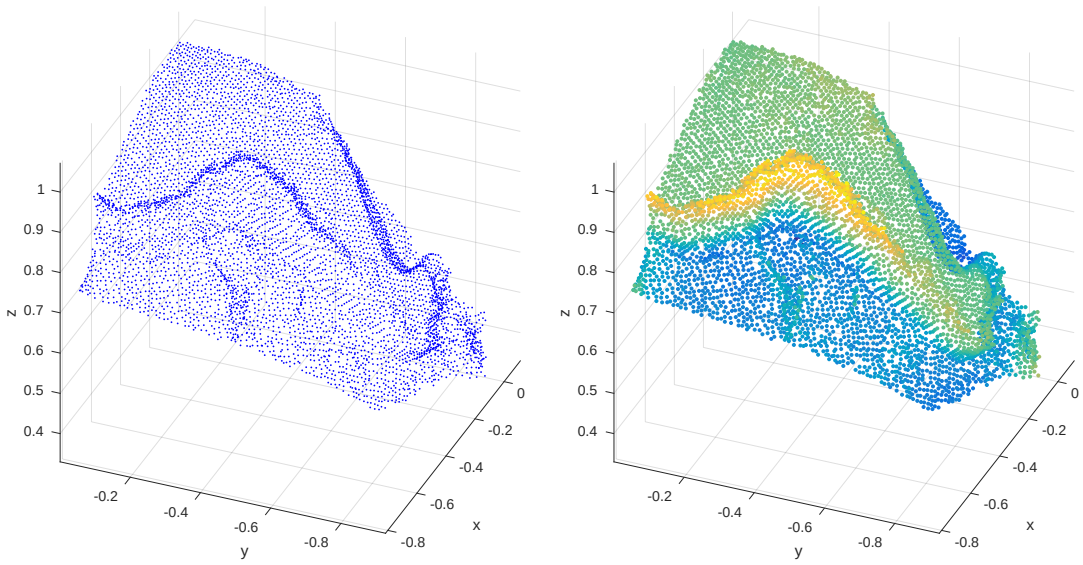

Figure 3.5: A fragment of the Western coast of South America. The nodes on the right are color-coded using heights.

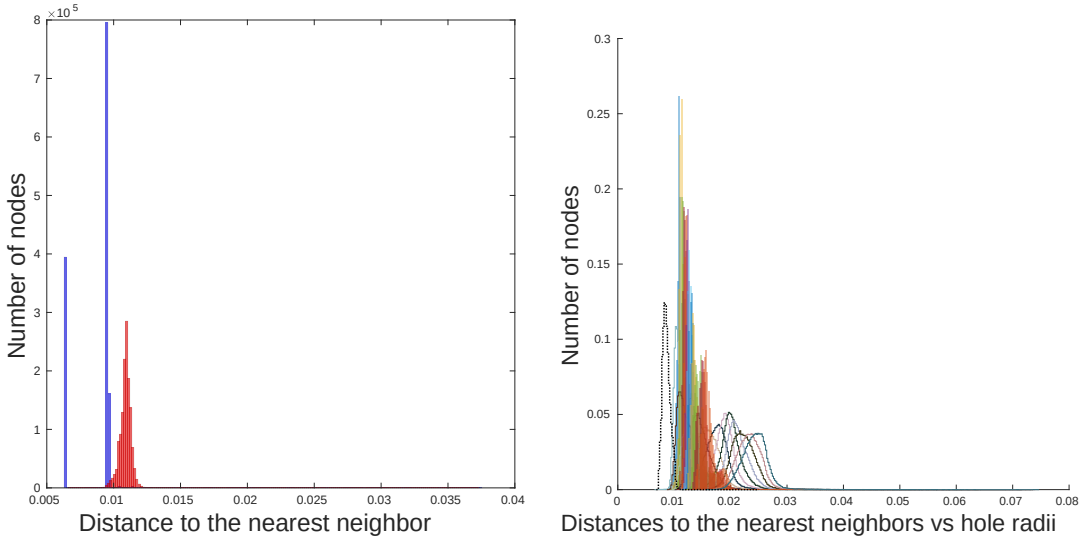

Figure 3.6: The effects of the repel procedure and hole radii.
Left: distribution of the nearest-neighbor distances in the atmospheric node set, before (blue) and after (red) executing the repel subroutine. Right: distribution of distances to the 12 nearest neighbors for the whole configuration (color only), for the surface subset (contours), the hole radii (black dashed contour).

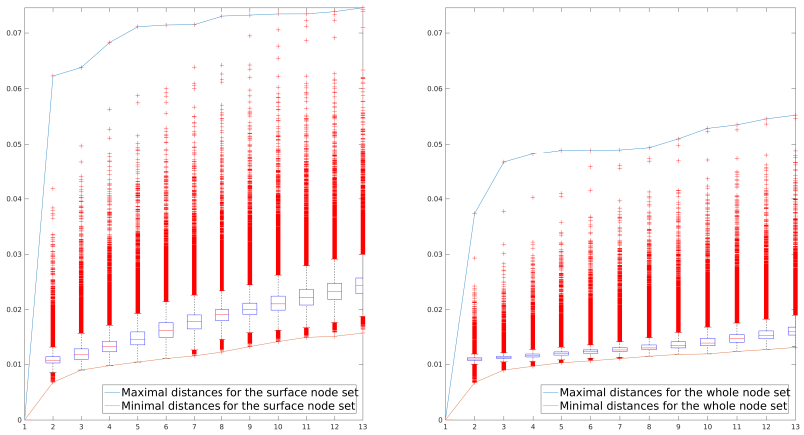

Figure 3.7: Distribution of distances to the 12 nearest neighbors for the atmospheric node configuration. Left: the surface subset. Right: the whole set. Scales are the same in both subplots.

function on the whole space $\mathbb{R}^3$. Note that all the histograms on the right are normalized by probability, not by the node count.

The pair of plots in Figure 3.7 shows in detail the distribution of distances to the nearest neighbors in the sample node set. It has been produced using the standard Matlab routine *boxplot*. Each of the blue boxes corresponding to a specific nearest neighbor, the central mark is the median, the edges of the box denote the 25th and 75th percentiles. The red crosses are what Matlab considers as outliers.

3.3.4.3 A pair of Gaussians

To demonstrate a nonuniform node distribution using our algorithm, we consider the following density function:

$$\rho(x) = 0.04 \cdot \min\left(\exp(0.2 \cdot \|x + [1,1,1]^t\|^2),\ \exp(0.1 \cdot \|x - [1,1,1]^t\|^2)\right).$$

The goal is therefore to produce a nodeset for which the distance to a nearest neighbor for the node x_i is close to the value $\rho(x_i)$. We proceed as in the algorithm above, and the resulting distribution recovers the density function quite well, see Figure 3.9. Picking

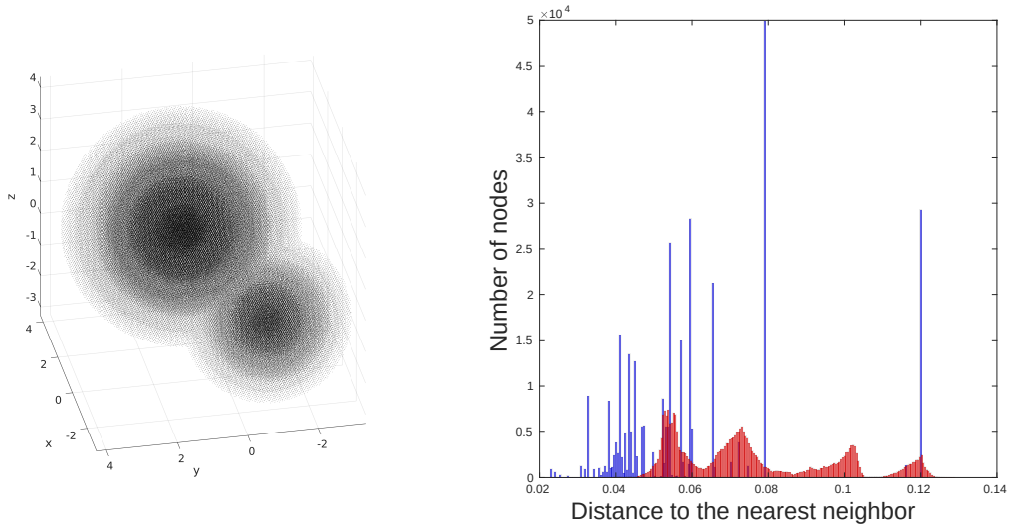

Figure 3.8: Left: the node set from Section 3.3.4.3. Right: distribution of the nearest neighbor distances, before (blue) and after (red) executing the repel subroutine.

318,662 nodes from the piecewise irrational lattice with variable density took 12.4 seconds, and 23 repelling iterations from Step 6 of the algorithm took additionally 18.86 seconds.

Figure 3.9 contains the plot of the ratio $\rho(x_i)/\delta_i(\omega_N)$. The minimal and maximal values of the ratio are about 0.650 and 1.112 respectively; its mean value is 0.847, and the variance is 0.004. The latter shows the quality of recovery of the radial density. A straightforward way to improve the recovery of a specific density is to increase the number of voxels per side of the enclosing cube, N_v. For the distribution discussed in this example, changing N_v from 100 to 200 caused only a four-fold increase in the total execution time.

3.4 Concluding remarks

- The nodes produced by the IL approach may still be too close to a lattice structure for some applications. In the light of connections to quasi-Monte Carlo methods, it is interesting to note that this issue is akin to the property of congruential number generator described in [70].

- One could, without much difficulty, modify the algorithm so that to use different sets of

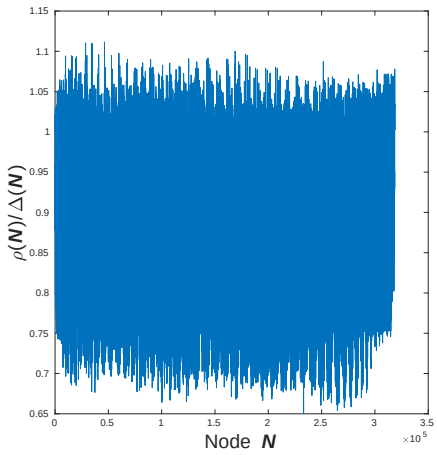

Figure 3.9: Ratios of the values of radial density function ρ to nearest neighbor distance, evaluated for the node set from Section 3.3.4.3.

irrational parameters $\alpha_1, \ldots, \alpha_{d-1}$ for different numbers of nodes in a voxel. This appears to be useful in mitigating the non-isotropic behavior of ILs as shown in Section 3.4.1

- Although it is largely obvious how to scale the algorithm to parallel architectures, our proof-of-concept implementation currently does not include it.

- Similar purpose meshing methods are widely used for dimensions 2 and 3, see, e.g., AMRClaw [30]; our approach is applicable to even higher dimensions. A shortcoming that is common to all quasi-Monte Carlo methods (and their derivatives) is, however, a much worse performance (measured by L^2 discrepancy), compared to Monte-Carlo distribution, in dimensions starting at about 15 [26].

3.4.1 Separation distances of tiled irrational lattices

The function $L(r)$ used in Step 3 is the number of nodes in the unit cube, placed according to (3.6), or obtained by minimizing the Riesz s-energy, such that the mean separation distance is the closest to r. To compute it in the case $d = 3$, we tabulate (mean) separation distances in a sample configuration comprised of n nodes in each of $27 = 3^3$ adjacent unit cubes. The nodes are obtained by shrinking and translating the lattice (3.6) by factor γ and vector ξ

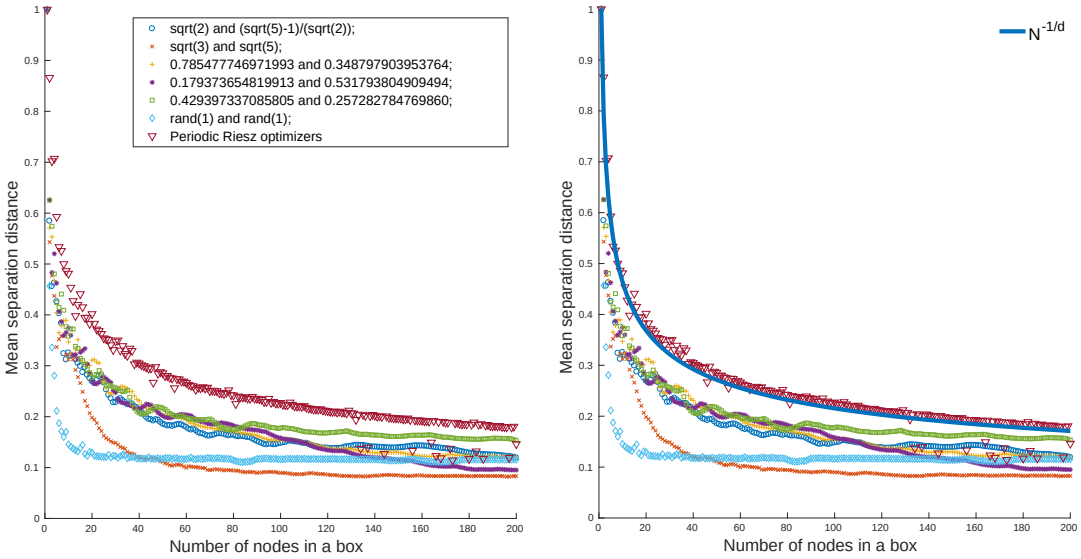

Figure 3.10: Dependence of the separation distance of the 3-dimensional lattice on the number of nodes in a single cube.

defined in (3.8). The tabulated dependence is then inverted and interpolated. The reason to consider separation distance between lattices in 3^d cubes in dimension d (and not a single cube) is to account for the boundary effects.

In general, putting too many nodes in individual voxels is justified only if the radial density function ρ varies slowly. For our applications, $1 \leq n \leq 100$ was sufficient.

The second plot in Figure 3.10 illustrates the delicate dependence of the separation distances of irrational lattices on the ratio used in each coordinate. While any set of irrational quantities $\alpha_1, \ldots, \alpha_{d-1}$ in (3.6), that are linearly independent over rationals, will give a uniformly distributed lattice as n grows, certain values may perform better than the others. In particular, adjustments can be made to improve the distribution for small values of n. Numerical experiments have shown, for example, that parameters $\alpha_1 = \sqrt{2}$, $\alpha_2 = (\sqrt{5}-1)/\sqrt{2}$ perform well in $\mathbb{R}^3$, which should be expected due to [8], where, in particular, it is pointed out that a 2-dimensional lattice generated by the golden ratio has optimal L^2 discrepancy.

We have carried out a numerical search for ratios maximizing the separation distance for the lattice in (3.6), and the results are shown in Figure 3.10. We found (necessarily

rational) pairs of ratios that perform at least as well, as the irrational pairs mentioned above. It follows that the function $L(r)$ will have very uneven structure for a fixed set of irrational parameters, which makes promising implementing a lookup function that would pick different parameters for different values of the number of nodes n. Unfortunately, we haven't been able to make much improvement in this way, over using the same pair of parameters for all numbers of nodes in a voxel. On the other hand, the minimal separation distances produced in this way are much smaller which is probably due to coincidental small separation between nodes in neighboring voxels with different parameters α_i.

CHAPTER 4

ASYMPTOTIC LINEAR PROGRAMMING BOUNDS FOR MINIMAL ENERGY NODES

4.1 Introduction

In this Chapter we prove lower bounds on the quantity $C_{s,d}$ from Theorem 1.2.4. For the discrete energy problem in a fixed dimension, the use of the Delsarte-Yudin linear programming bounds and Levenshtein $1/N$-quadrature rules are known to provide bounds on the minimal energy and prove universal optimality of some configurations on the sphere $\mathbb{S}^d$ (see for example [35]). We use this framework to bound $\mathcal{E}_s(N,\mathbb{S}^d)$ in the limit as N grows. Due to the localized nature of the Riesz potential when $s > d$, these bounds are independent of the underlying set $\mathbb{S}^d$.

A simple lower bound for $C_{s,d}$ comes from the following convexity argument. Let $\omega_N^* = \{x_1, \ldots x_N\}$ be an optimal packing configuration on $\mathbb{S}^d$, and for each $i = 1 \ldots N$, let $\delta_i := \min_{j \neq i} \|x_i - x_j\|$. Then $\sum_{i=1}^N (\delta_i/2)^d \leq \mathcal{H}_d(\mathbb{S}^d)$ and by convexity we have

$$\sum_{i \neq j} \frac{1}{|x_i - x_j|^s} \geq \sum_{i=1}^N \frac{1}{\delta_i^s} = \sum_{i=1}^N (\delta_i^d)^{-s/d} \geq N \left(\frac{1}{N} \sum_{i=1}^N \delta_i^d \right)^{-s/d} \geq N^{1+\frac{s}{d}} 2^{-s} (\mathcal{H}_d(\mathbb{S}^d))^{-s/d},$$

thus establishing

Proposition 4.1.1.

$$C_{s,d} \geq \Theta_{s,d} := \frac{\mathcal{H}_d(\mathbb{S}^d)^{-s/d}}{2^s}$$

Another lower bound is the following, established in [21]:

Proposition 4.1.2. *Let $d \geq 2$, $s > d$, then for $(s-d)/2$ not an integer,*

$$C_{s,d} \geq \xi_{s,d} := \left[\frac{\pi^{d/2}\Gamma(1+\frac{s-d}{2})}{\Gamma(1+\frac{s}{2})}\right]^{s/d} \frac{d}{s-d}$$

The main result of this chapter is to improve these lower bounds.

Theorem 4.1.3. *For a fixed dimension d, let z_i be the i^{th} smallest positive zero of the Bessel function $J_{d/2}(z)$, $i = 1, 2, \ldots$. Then*

$$C_{s,d} \geq A_{s,d} \tag{4.1}$$

where

$$A_{s,d} := \left[\frac{\pi^{\frac{d+1}{2}}\Gamma(d+1)}{\Gamma(\frac{d+1}{2})}\right]^{s/d} \frac{4}{\lambda_d \Gamma(d+1)} \sum_{i=1}^{\infty} (z_i)^{d-s-2} \left(J_{d/2+1}(z_i)\right)^{-2}, \tag{4.2}$$

and

$$\lambda_d = \int_{-1}^{1} (1-t^2)^{\frac{d-2}{2}} dt = \frac{\sqrt{\pi}\Gamma(\frac{d}{2})}{\Gamma(\frac{d+1}{2})}. \tag{4.3}$$

For $d = 1$, $A_{s,d} = 2\zeta(s)$ which is optimal. Furthermore, when $d = 2$, our bound is tight as $s \to d^+$.

Theorem 4.1.4.

$$\lim_{s \to 2^+} \frac{(\sqrt{3}/2)^{s/2}\zeta_{\Lambda_2}(s)}{C_{s,2}} = 1. \tag{4.4}$$

As shown in Corollary 4.2.10, the Levenshtein $1/N$-quadrature rules give bounds on the minimal separation distance for optimal packings on $\mathbb{S}^d$, and $A_{s,d}$ recovers these bounds as $s \to \infty$. For $d = 2, 4, 8$, and 24, letting $\widetilde{C}_{s,d}$ be the conjectured values of $C_{s,d}$ from Conjecture 1.3.2, then $\lim_{s\to\infty}(\widetilde{C}_{s,d}/A_{s,d})^{1/s}$ exists. Theorem 4.1.3 is analogous to Theorem 1.4 of [31]

which is given in terms of Gaussian energy of configurations on the plane. We define this case in the following way.

Definition 4.1.5. Denote by $B(r)$ the ball in $\mathbb{R}^d$ of radius r centered at 0. For an infinite configuration $\mathcal{C} \subset \mathbb{R}^d$ and $f : (0,\infty) \to \mathbb{R}$, the *lower f-energy* of $\mathcal{C}$ is

$$E_f(\mathcal{C}) := \liminf_{r\to\infty} \frac{1}{\#\mathcal{C} \cap B(r)} \sum_{\substack{x,y\in\mathcal{C}\cap B(r) \\ x\neq y}} f(\|x-y\|)$$

If the limit exists, we call it the *f-energy* of $\mathcal{C}$.

Recall the definition of the density of an infinite configuration from (1.12). The proof of Theorem 4.1.3 yields an alternate proof of the main theorem in [31].

Theorem 4.1.6. *Let $f(\|x-y\|) = e^{-\alpha\|x-y\|^2}$ be a Gaussian potential and choose R so that $vol(B(R/2)) = \rho$. Then the minimal f-energy for point configurations of density ρ in $\mathbb{R}^d$ is bounded below by*

$$\frac{4}{\lambda_d \Gamma(d+1)} \sum_{i=1}^{\infty} z_i^{d-2} \big(J_{d/2+1}(z_i)\big)^{-2} f\left(\frac{z_i}{\pi R}\right). \tag{4.5}$$

In Section 4.2 we introduce the Delsarte-Yudin linear programming lower bounds and the Levenshtein $1/N$-quadrature rules. More thorough treatments can be found in [13], [17], and [68]. In Section 4.3, we present the proof of Theorems 4.1.3, 4.1.4, and 4.1.6 using an asymptotic result on Jacobi polynomials from Szegő, and in Section 4.4 we discuss numerically the quality of the bound $A_{s,d}$ and formulate a natural conjecture.

For $\alpha, \beta \geq -1$, let $\left\{P_k^{(\alpha,\beta)}\right\}_{k=1}^{\infty}$ be the family of Jacobi polynomials which are orthogonal with respect to the weight $\omega^{(\alpha,\beta)}(t) := (1-t)^{\alpha}(1+t)^{\beta}$. That is,

$$\langle P_k^{(\alpha,\beta)}, P_j^{(\alpha,\beta)} \rangle := \int_{-1}^{1} P_k^{(\alpha,\beta)}(t) P_j^{(\alpha,\beta)}(t) \omega^{(\alpha,\beta)}(t) dt = r_k^{(\alpha,\beta)} \delta_{jk} \tag{4.6}$$

for some constants $r_k^{(\alpha,\beta)}$ where δ_{jk} is the Kroenecker delta. We choose the normalization

$$P_k^{(\alpha,\beta)}(1) = 1. \tag{4.7}$$

While this normalization is crucial for the linear programming methods presented here, we note that many authors in the orthogonal polynomial literature choose $P_k^{(\alpha,\beta)}(1) = \binom{k+\alpha}{k}$. For a fixed dimension $d \geq 1$, the Gegenbauer or ultraspherical polynomials are given by $P_k(t) := P_k^{(\frac{d-2}{2}, \frac{d-2}{2})}(t)$ and $\omega_d(t) := \omega^{(\frac{d-2}{2}, \frac{d-2}{2})}(t)$ and we define the adjacent polynomials

$$P_k^{a,b}(t) := P_k^{(\frac{d-2}{2}+a, \frac{d-2}{2}+b)}(t) \tag{4.8}$$

with weights $\omega_d^{a,b}(t)$ defined similarly. The weights $\omega_d(t)$ arise from itegration over $\mathbb{S}^d$ with respect to the normalized surface area measure $\sigma_{\mathbb{S}^d}$. If f is a function integrable on $[-1,1]$ with respect to the weight $\omega_d(t)$, then from a special case of the Funk-Hecke formula [75, Theorem 6], for any fixed point $y \in \mathbb{S}^d$,

$$\int_{S^d} f(\langle x, y \rangle) d\sigma_{\mathbb{S}^d}(x) = \frac{1}{\lambda_d} \int_{-1}^{1} f(t) \omega_d(t) dt. \tag{4.9}$$

where λ_d is defined in (4.3). Any $f : [-1,1] \to \mathbb{R}$ can be uniquely expanded in terms of the Gegenbauer polynomials $f(t) = \sum_{k=0}^{\infty} f_k P_k(t)$ where the f_k are given by

$$f_k := \frac{\int_{-1}^{1} f(t) P_k(t) \omega_d(t) dt}{\int_{-1}^{1} [P_k(t)]^2 \omega_d(t) dt}. \tag{4.10}$$

Recall that a real valued homogeneous polynomial $f(x) = f(x_1, \ldots, x_{d+1})$ is called *harmonic* if it satisfies Laplace's equation:

$$\Delta(f) = \frac{\partial^2 f}{\partial x_1^2} + \cdots + \frac{\partial^2 f}{\partial x_{d+1}^2} = 0. \tag{4.11}$$

A function $Y(x)$ is called a *spherical harmonic* on $\mathbb{S}^d$ if it is the restriction of a real valued homogeneous polynomial that is harmonic on $\mathbb{R}^{d+1}$. The set of all spherical harmonics of total degree k, denoted by $\mathbb{H}_k^d$, form a linear subspace of $L_2(\mathbb{S}^d)$ and can be shown to have dimension

$$Z(d,k) = \dim(\mathbb{H}_k^d) = (2k+d-1)\frac{\Gamma(k+d-1)}{\Gamma(d)\Gamma(k+1)}.$$

Let $\{Y_{kl}(x)\}_{l=1}^{Z(d,k)}$ be an orthonormal basis of $\mathbb{H}_k^d$. The Gegenbauer polynomials are related to spherical harmonics by the Addition Formula [3],

$$\sum_{l=1}^{Z(d,k)} Y_{kl}(x) Y_{kl}(y) = Z(d,k) P_k(\langle x, y \rangle). \tag{4.12}$$

An immediate consequence of (4.12) is that for any configuration $\omega_N = \{x_1 \ldots x_N\} \subset \mathbb{S}^d$,

$$\begin{aligned} \sum_{i,j=1}^{N} P_k(\langle x_i, x_j \rangle) &= \frac{1}{Z(d,k)} \sum_{l=1}^{Z(d,k)} \sum_{i,j=1}^{N} Y_{kl}(x_i) Y_{kl}(x_j) \\ &= \frac{1}{Z(d,k)} \sum_{l=1}^{Z(d,k)} \left(\sum_{i=1}^{N} Y_{kl}(x_i) \right)^2 \geq 0. \end{aligned} \tag{4.13}$$

We call an N-point configuration $\omega_N = \{x_1 \ldots x_N\} \subset S^d$ a *spherical τ design* if

$$\int_{S^d} f(x) d\sigma_{\mathbb{S}^d}(x) = \frac{1}{N} \sum_{i=1}^{N} f(x)$$

holds for all spherical polynomials f of degree at most τ. Equivalently, ω_N is a spherical design if and only if

$$\sum_{i=1}^{N} Y_{kl}(x_i) = 0 \tag{4.14}$$

for all $1 \leq l \leq Z(d,k)$, $1 \leq k \leq \tau$, which from (4.13) holds if and only if

$$\sum_{i,j=1}^{N} P_k(\langle x_i, x_j \rangle) = 0 \tag{4.15}$$

for all $1 \leq k \leq \tau$.

Then the following result forms the basis for the linear programming bounds for packing and energy on the sphere:

Theorem 4.2.1. *Suppose $f : [-1,1] \to \mathbb{R}$ is of the form*

$$f(t) = \sum_{k=0}^{\infty} f_k P_k(t)$$

with $f_k \geq 0$ for all $k \geq 1$ and $\sum_{k=0}^{\infty} f_k < \infty$. Then for $\omega_N = \{x_1, \ldots, x_N\} \subset \mathbb{S}^d$,

$$\sum_{1 \leq i \neq j \leq N} f(\langle x_i, x_j \rangle) \geq f_0 N^2 - f(1)N. \tag{4.16}$$

Moreover, if the energy kernel $K(x,y) := h(\langle x, y \rangle)$ for some $h : [-1,1] \to [0,\infty]$ such that $h(t) \geq f(t)$, then

$$E_K(\omega_N) \geq \mathcal{E}_K(N, \mathbb{S}^d) \geq f_0 N^2 - f(1)N \tag{4.17}$$

Equality holds in (4.17) if and only if

1. *$h(t) = f(t)$ for all $t \in \left\{ \langle x_i, x_j \rangle : i \neq j \right\}$ and*
2. *for all $k \geq 1$, either $f_k = 0$ or $\sum_{i,j=1}^{N} P_k(\langle x_i, x_j \rangle) = 0$.*

In this case ω_N is an optimal K-energy configuration

Proof.

$$\begin{aligned} E_h(\omega_N) \geq E_f(\omega_N) &= \sum_{i,j=1}^{N} f(\langle x_i, x_j \rangle) - f(1)N \\ &= \sum_{k=0}^{\infty} f_k \sum_{i,j=1}^{N} P_k(\langle x_i, x_j \rangle) - f(1)N \\ &\geq f_0 N^2 - f(1)N. \end{aligned} \tag{4.18}$$

where we throw away all but the $k = 0$ term in the sum. This inequality holds since $f_k \geq 0$ and $\sum_{i,j=1}^{N} P_k(\langle x_i, x_j \rangle) \geq 0$ by (4.13). The first inequality is equality if and only if $h(t) = f(t)$ for all $t \in \{\langle x_i, x_j \rangle : i \neq j\}$ while the second is equality if and only if for all $k \geq 1$, either $f_k = 0$ or $\sum_{i,j=1}^{N} P_k(\langle x_i, x_j \rangle) = 0$. □

In the case when ω_N is a spherical τ-design, we have following consequence of Theorem 4.2.1

Corollary 4.2.2. *Suppose ω_N is a spherical τ-design and $f(t)$ is a polynomial of degree at most τ such that $f(t) \geq 0$ on $[-1, 1]$ and $f_0 \geq 0$. Then*

$$N \geq \frac{f(1)}{f_0} \tag{4.19}$$

Proof. With the above assumptions on f, equality holds throughout in (4.18) since $\sum_{i,j=1}^{N} P_k(\langle x_i, x_j \rangle) = 0$ for $1 \leq k \leq \tau$, and $f_k = 0$ for $k > \tau$. Thus

$$0 \leq E_f(\omega_N) = f_0 N^2 - f(1)N$$

□

Using Corollary 4.2.2, Delsarte, Goethals, and Siedel [41] obtain a lower bound on

$$B(d,\tau) := \min\left\{N : \exists\ \omega_N \subset S^d \text{ a spherical } \tau \text{ design}\right\}.$$

Theorem 4.2.3.

$$B(d,\tau) \geq D(d,\tau) := \begin{cases} 2\binom{d+k-1}{d}, & \text{if } \tau = 2k-1 \\ \binom{d+k}{d} + \binom{d+k-1}{d}, & \text{if } \tau = 2k \end{cases}$$

Proof. Let $\widetilde{P}_k(t)$ denote the degree k Gegenbauer polynomial normalized by

$$\widetilde{P}_k(1) = \binom{d+k}{d} - \binom{d+k-2}{d}.$$

This normalization gives the orthogonality property

$$\int_{-1}^{1} \widetilde{P}_l(t)\widetilde{P}_k(t)\omega_d(t)dt = \lambda_d \widetilde{P}_k(1)\delta_{kl}.$$

Now let

$$R_k(t) := \sum_{i=0}^{k} \widetilde{P}_i(t).$$

At $t = 1$ this is a telescoping series and so

$$R_k(1) = \binom{d+k}{d} + \binom{d+k-1}{d}.$$

Suppose ω_N is a spherical $2k$-design. Take $f(t) = (R_k(t))^2$. This function satisfies the

hypotheses of Corollary 4.2.2 because by orthogonality,

$$\begin{aligned} f_0 &= \frac{1}{\lambda_d}\int_{-1}^{1} f(t)\omega_d(t)dt = \frac{1}{\lambda_d}\int_{-1}^{1}\left(\sum_{i=0}^{k}\widetilde{P}_i(t)\right)^2\omega_d(t)dt \\ &= \frac{1}{\lambda_d}\sum_{i=0}^{k}\int_{-1}^{1}(\widetilde{P}_i(t))^2\omega_d(t)dt \\ &= \sum_{i=0}^{k}\widetilde{P}_i(1) = R_k(1) > 0. \end{aligned}$$

Thus $N \geq f(1)/f_0 = (R_k(1))^2/R_k(1) = R_k(1)$. The bound for the case when ω_N is a $2k-1$ design can be established similarly by defining

$$C_k(t) := \sum_{i=0}^{\lfloor k/2 \rfloor}\widetilde{P}_{k-2i}(t)$$

and considering the function

$$f(t) = (t+1)(C_{k-1}(t))^2$$

□

4.2.1 Levenshtein $1/N$ quadrature rules

A sequence of ordered pairs $\{(\alpha_i,\rho_i)\}_{i=1}^{k}$ is said to be a $1/N$-*quadrature rule exact on a subspace* $\Lambda \subset C([-1,1])$ if $-1 \leq \alpha_k < \cdots < \alpha_1 < 1$, $\rho_i > 0$ for $i = 1,\ldots,k$, and for all $f \in \Lambda$,

$$f_0 = \frac{1}{\lambda_d}\int_{-1}^{1} f(t)\omega_d(t)dt = \frac{f(1)}{N} + \sum_{i=1}^{k}\rho_i f(\alpha_i). \tag{4.20}$$

Theorem 4.2.1 gives rise immediately to the following:

Theorem 4.2.4. *Let* $\{(\alpha_i,\rho_i)\}_{i=1}^{k}$ *be a* $1/N$*-quadrature rule exact on* Λ*. For* $K(x,y) = h(\langle x,y\rangle)$*, let* A_h *be the set of functions* $f(t) \leq h(t)$ *satisfying the hypotheses of Theorem 4.2.1. Then,*

$$\mathcal{E}_K(N,\mathbb{S}^d) \geq N^2 \sum_{i=1}^{k} \rho_i f(\alpha_i).$$

and

$$\sup_{f\in\Lambda\cap\mathcal{A}_h} N^2 \sum_{i=1}^{k} \rho_i f(\alpha_i) \leq N^2 \sum_{i=1}^{k} \rho_i h(\alpha_i)$$

Levenshtein derives a $1/N$-quadrature given in Theorem 4.2.5 to obtain the following bound for the maximal cardinality of a configuration $\omega_N \subset \mathbb{S}^d$ with largest inner product s. Letting $\gamma_k^{a,b}$ denote the greatest zero of $P_k^{a,b}(t)$, partition $[-1,1]$ into the following disjoint union of countable intervals. For $\tau = 1,2\ldots$,

$$I_\tau := \begin{cases} [\gamma_{k-1}^{1,1}, \gamma_k^{1,0}], & \text{if } \tau = 2k-1 \\ [\gamma_k^{1,0}, \gamma_k^{1,1}], & \text{if } \tau = 2k. \end{cases}$$

This partition is well defined by the interlacing properties $\gamma_{k-1}^{1,1} < \gamma_k^{1,0} < \gamma_k^{1,1}$. Let

$$A(d,s) := \max\left\{N : \exists\ \omega_N \subset \mathbb{S}^d, \langle x_i, x_j\rangle \leq s, i \neq j\right\}.$$

Then,

$$A(d,s) \leq L(d,s),$$

where

$$L(d,s) = \begin{cases} L_{2k-1}(d,s) = \binom{k+d-2}{k-1}[\frac{2k+d-2}{d} - \frac{P_{k-1}(s)-P_k(s)}{(1-s)P_k(s)}], & \text{if } s \in I_{2k-1} \\ L_{2k}(d,s) = \binom{k+d-1}{k}[\frac{2k+d-1}{d} - \frac{(1+s)(P_k(s)-P_{k+1}(s))}{(1-s)(P_k(s)+P_{k+1}(s))}], & \text{if } s \in I_{2k}. \end{cases} \tag{4.21}$$

The function $L(d,s)$ is called the Levenshtein function. It is continuous and increasing on $[-1,1]$. The formula for the Levenshtein function is such that the quadrature nodes given in Theorem 4.2.5 below will have weight $1/N$ at the node $\alpha_0 = 1$. At the endpoints of the

intervals I_τ,

$$\begin{aligned} L_{2k-2}(d,\gamma_{k-1}^{1,1}) &= L_{2k-1}(d,\gamma_{k-1}^{1,1}) = D(d,2k-1) \\ L_{2k-1}(d,\gamma_{k-1}^{1,0}) &= L_{2k}(d,\gamma_{k-1}^{1,0}) = D(d,2k). \end{aligned} \tag{4.22}$$

Letting $r_i^{a,b} := (\int_{-1}^{1}(P_i^{a,b}(t))^2 d\omega_d^{a,b}(t))^{-1}$, $l_i^{a,b}$ be the leading coefficient of $P_i^{a,b}(t)$, and $m_i^{a,b} := l_i^{a,b}/l_{i+1}^{a,b}$, define

$$Q_k^{a,b}(x,y) := \sum_{i=0}^{k} r_i^{a,b} P_i^{a,b}(x) P_i^{a,b}(y). \tag{4.23}$$

By the Cristoffel-Darboux formula (c.f. [97, Section 3.2]), an alternate formula for $Q_k^{a,b}(x,y)$ is

$$Q_k^{a,b}(x,y) = r_k^{a,b} m_k^{a,b} \left(\frac{P_{k+1}^{a,b}(x)P_k^{a,b}(y) - P_k^{a,b}(x)P_{k+1}^{a,b}(y)}{x-y} \right), \qquad x \neq y \tag{4.24}$$

$$Q_k^{a,b}(x,x) = r_k^{a,b} m_k^{a,b} (P_{k+1}^{a,b'}(x)P_k^{a,b}(x) - P_k^{a,b'}(x)P_{k+1}^{a,b}(x)). \tag{4.25}$$

The following $1/N$-quadrature rule proven in [67] Theorems 4.1 and 4.2, forms the basis of the proof of Theorem 4.1.3.

Theorem 4.2.5. *For $N \in \mathbb{N}$, let τ be such that $N \in (D(d,\tau), D(d,\tau+1)]$, and let $\alpha_1 = \beta_1 = s$ be the unique solution to*

$$N = L(d,s).$$

i) If $\tau = 2k-1$, define nodes $-1 < \alpha_k < \cdots < \alpha_1 < 1$ by the solutions of

$$(t-s)Q_{k-1}^{1,0}(t,s) = 0 \tag{4.26}$$

and weights

$$\rho_i = \frac{1}{\lambda_d(1-\alpha_i)Q_{k-1}^{1,0}(\alpha_i,\alpha_i)}. \tag{4.27}$$

Then $\{(\alpha_i,\rho_i)\}_{i=1}^k$ *form a* $1/N$*-quadrature rule which is exact on* Π_{2k-1}*, the space of polynomials of degree less than or equal to* $2k-1$*.*

ii) If $\tau = 2k$*, define nodes* $-1 = \beta_{k+1} < \cdots < \beta_1 < 1$ *by the solutions of*

$$(1+t)(t-s)Q_{k-1}^{1,1}(t,s) = 0 \tag{4.28}$$

and weights

$$\begin{aligned} \eta_i &= \frac{1}{\lambda_d(1-\beta_i^2)Q_k^{1,1}(\beta_i,\beta_i)}, \qquad i = 1,\ldots,k, \\ \eta_{k+1} &= \frac{Q_k^{1,1}(s,1)}{Q_k^{1,1}(-1,-1)Q_k^{1,1}(s,1) - Q_k^{1,1}(-1,1)Q_k^{1,1}(s,-1)}. \end{aligned} \tag{4.29}$$

Then $\{(\beta_i,\eta_i)\}_{i=1}^{k+1}$ *form a* $1/N$*-quadrature rule which is exact on* Π_{2k}*.*

Remark 4.2.6. If N is at the endpoints of this interval, we also have that for $N = D(d,2k)$, $\{(\alpha_i,\rho_i)\}_{i=1}^k$ is exact on Π_{2k} and for $N = D(2k+1)$, $\{(\beta_i,\eta_i)\}_{i=1}^{k+1}$ is exact on Π_{2k+1}.

Proof. We prove the case for $\tau = 2k-1$, the second case being similar. Denote by $\alpha_0 := 1$ and $\rho_0 := 1/N$. For simplicity, throughout this proof, denote $Q_k^{1,0}(t)$ by $Q_k(t)$, $P_k^{1,0}(t)$ by $P_k(t)$ and $r_k^{1,0}$ by r_k. Note first that if α_i and α_j are two distinct zeros of $(t-s)Q_k(t,s)$ for a fixed s, then $Q_k(\alpha_i,\alpha_j) = 0$. Indeed we have,

$$P_{k+1}(\alpha_i)P_k(s) - P_k(\alpha_i)P_{k+1}(s) = 0,$$

and a similar equation for α_j, and thus

$$P_{k+1}(\alpha_i)P_k(\alpha_j) - P_k(\alpha_i)P_{k+1}(\alpha_j) \\ = \frac{P_k(\alpha_i)P_{k+1}(s)}{P_k(s)}P_k(\alpha_j) - P_k(\alpha_i)\frac{P_k(\alpha_j)P_{k+1}(s)}{P_k(s)} = 0.$$

Now let

$$g_i(t) := \frac{(1-t)Q_{k-1}(t,\alpha_i)}{(1-\alpha_i)Q_{k-1}(\alpha_i,\alpha_i)}, \qquad i = 1,\ldots k, \tag{4.30}$$

$$g_0(t) := \frac{(t-s)Q_{k-1}(t,s)}{(1-s)Q_{k-1}(1,s)} \tag{4.31}$$

These are the annihilating polynomials because

$$g_i(\alpha_j) = \delta_{i,j} \qquad \text{for} \quad i,j = 1,\ldots k$$

Thus for a polynomial $f \in \Pi_{2k-1}$, the polynomial

$$f(t) - \sum_{i=0}^{k} f(\alpha_i)g_i(t)$$

has zeros $\alpha_0,\ldots,\alpha_k$ and hence

$$f(t) - \sum_{i=0}^{k} f(\alpha_i)g_i(t) = (1-t)(t-s)Q_{k-1}(t,s)\tilde{f}(t)$$

for some $\tilde{f} \in \Pi_{k-2}$. Thus, since $P_{k-1}(t), P_k(t) \in \Pi_{k-2}^{\perp}$ with respect to $(1-t)\omega_d(t)$,

$$\int_{-1}^{1}\left(f(t)-\sum_{i=0}^{k}f(\alpha_i)g_i(t)\right)\omega_d(t)dt$$
$$=\int_{-1}^{1}(t-s)Q_{k-1}(t,s)\tilde{f}(t)(1-t)\omega_d(t)dt$$
$$=\int_{-1}^{1}r_k m_k(P_k(t)P_{k-1}(s)-P_{k-1}(t)P_k(s))\tilde{f}(t)(1-t)\omega_d(t)dt$$
$$=0,$$

and hence,

$$\int_{-1}^{1}f(t)\omega_d(t)dt=\sum_{i=0}^{k}\rho_i f(\alpha_i)\qquad \rho_i=\int_{-1}^{1}g_i(t)\omega_d(t)dt$$

Equation (4.27) follows from formula (4.30) and noticing that by orthogonality,

$$\int_{-1}^{1}Q_{k-1}(t,\alpha_i)(1-t)\omega_d(t)dt=\int_{-1}^{1}\sum_{j=0}^{k}r_i P_j(t)P_j(\alpha_i)(1-t)\omega_d(t)dt$$
$$=\int_{-1}^{1}r_0P_0(t)P_0(\alpha_i)(1-t)\omega_d(t)dt=1.$$

□

Boyvalenkov et. al [20] use this quadrature rule to derive a universal lower bound for spherical configurations.

Theorem 4.2.7. *Let N be fixed and $h(t)$ an absolutely monotone potential, i.e. $h^{(k)}(t)\geq 0$ for all k. Suppose $\tau=\tau(d,N)$ is such that $N\in(D(d,\tau),D(d,\tau+1)]$ and let $k=\lceil\frac{\tau+1}{2}\rceil$. Letting α_i, ρ_i, $i=1\ldots k$ be the quadrature nodes from Theorem 4.2.5, then*

$$\mathcal{E}_h(N,\mathbb{S}^d)\geq N^2\sum_{i=1}^{k}\rho_i h(\alpha_i). \tag{4.32}$$

Taking into account Theorem 4.2.4, this is the optimal linear programming bound for

$\Lambda = \Pi_k$. As an application, we show that theorem 4.2.7 recovers the first order asymptotics for a large class of potentials.

Corollary 4.2.8. *Let $h(t)$ be absolutely monotone and integrable with respect to $\omega_d(t)$.*

$$\lim_{N\to\infty} \frac{\mathcal{E}_h(N,\mathbb{S}^d)}{N^2} \geq \frac{1}{\lambda_d}\int_{-1}^{1} h(t)\omega_d(t)dt \tag{4.33}$$

Remark 4.2.9. It is a classical result of potential theory that the limit exists and equality holds in (4.33). The Riesz case is given in (1.10).

Proof. First suppose $h(t)$ is continuous on $[-1,1]$. For $\varepsilon > 0$, let $f(t)$ be a polynomial of degree $\leq 2k-1$ such that $f(t) - h(t) \leq \varepsilon$ uniformly on $[-1,1]$. Let $(\alpha_0,\rho_0) = (1,1/N)$, and note that the weights ρ_i given in (4.27) are positive for $i = 0,\ldots,k$ and $\sum_{i=0}^{k}\rho_i = 1$. From (4.20), we have

$$\begin{aligned}\left|\frac{1}{\lambda_d}\int_{-1}^{1} h(t)\omega_d(t)dt - \sum_{i=0}^{k}\rho_i h(\alpha_i)\right| & \\ &\leq \frac{1}{\lambda_d}\int_{-1}^{1}|h(t)-f(t)|\omega_d(t)dt + \sum_{i=0}^{k}\rho_i|f(\alpha_i)-h(\alpha_i)| \\ &\leq 2\varepsilon \to 0 \qquad \text{as } N\to\infty\end{aligned}$$

Since $\rho_0 h(\alpha_0) = h(1)/N \to 0$, equation (4.33) follows. Next suppose $h(t)$ is integrable and $g_m \nearrow h$ a sequence of continuous functions increasing to h (for existence, consider $g_m(t) := h((1-1/m)(t+1)-1)$). By the Monotone Convergence Theorem and a similar string of inequalities as above, it is clear that

$$\lim_{k\to\infty}\sum_{i=i}^{k}\rho_i h(\alpha_i) = \int_{-1}^{1} h(t)\omega_d(t)$$

□

Corollary 4.2.10. *Let $\omega_N^* = \{x_1,\ldots x_N\}$ be an optimal N-point packing configuration on $\mathbb{S}^d$*

and $y_N := \max_{i \neq j} \langle x_i, x_j \rangle$. *Then*

$$y_N \geq \alpha_1 \tag{4.34}$$

Proof. Let

$$h_\alpha(t) = \begin{cases} \infty & \text{if } t > \alpha \\ 0 & \text{if } t \leq \alpha. \end{cases}$$

Then by Theorem 4.2.7, $E_{h_\alpha}(\omega_N^*) \geq N^2 \sum_{i=1}^{k} \rho_i h_\alpha(\alpha_i)$. If $y_N < \alpha_1$, then $E_{h_{y_N}}(\omega_N^*) = 0$, but $\sum_{i=1}^{k} \rho_i h_{y_N}(\alpha_i) = \infty$. □

4.3 Proofs of Theorems 4.1.3, 4.1.4, and 4.1.6

Our approach will be to find the asymptotic expansion of (4.32) as $N \to \infty$. We will make use of the following result from Szegő (c.f [97, Theorem 8.1.1]) adjusted by normalization (4.7):

Theorem 4.3.1.

$$\lim_{k\to\infty} P_k^{(\alpha,\beta)}\left(\cos\frac{z}{k}\right) = \lim_{k\to\infty} P_k^{(\alpha,\beta)}\left(1 - \frac{z^2}{2k^2}\right) = \Gamma(\alpha+1)\left(\frac{z}{2}\right)^{-\alpha} J_\alpha(z).$$

This gives the following immediate corollary:

Corollary 4.3.2. *If* $-1 \leq \gamma_{k,k} < \cdots < \gamma_{k,1} \leq 1$ *are the zeros of* $P_k^{(\alpha,\beta)}$, *and* z_i *is the* i^{th} *smallest positive zero of the Bessel function* $J_\alpha(z)$, *then*

$$\lim_{k\to\infty} k\cos^{-1}(\gamma_{k,i}) = z_i \tag{4.35}$$

We will also make use of well known properties of the derivatives, norms, and leading coefficients of the Jacobi polynomials (see for example [97, Chapter 4], using $\alpha = d/2$, $\beta = (d-2)/2$ and adjusting for normalization (4.7)):

$$\begin{aligned}\frac{\mathrm{d}}{\mathrm{d}t}P_k^{1,0}(t) &= \frac{1}{2}(k+d)\frac{\binom{k+\frac{d+2}{2}}{k}}{\binom{k+\frac{d}{2}}{k}}P_{k-1}^{2,1}(t)\\ &= \frac{1}{2}(k+d)\left(\frac{2k+d+2}{d+2}\right)P_{k-1}^{2,1}(t)\\ &= \left(\frac{k^2}{d+2}+o(k^2)\right)P_{k-1}^{2,1}(t).\end{aligned} \tag{4.36}$$

Secondly,

$$\begin{aligned}r_k^{1,0} &= \left(\int_{-1}^{1}(P_k^{1,0}(t))^2 d\omega^{1,0}(t)\right)^{-1}\\ &= \left(\frac{2^d\Gamma(k+\frac{d+2}{2})\Gamma(k+\frac{d}{2})}{\binom{k+\frac{d}{2}}{k}^2(2k+d)\Gamma(k+d)\Gamma(k+1)}\right)^{-1}\\ &= \frac{(2k+d)^2\Gamma(k+d)}{2^(d+1)\Gamma(\frac{d+2}{2})^2\Gamma(k+1)}\\ &= \frac{k^{d+1}}{2^{d-1}\Gamma(\frac{d+2}{2})^2}+o(k^{d+1}).\end{aligned} \tag{4.37}$$

Lastly, denoting $l_k^{1,0}$ as the leading coefficient of $P_k^{1,0}(t)$,

$$l_k^{1,0} = \frac{\Gamma(2k+d)}{\binom{k+\frac{d}{2}}{k}2^k\Gamma(k+1)\Gamma(k+d)},$$

then the ratio

$$\begin{aligned}m_k^{1,0} := \frac{l_k^{1,0}}{l_{k+1}^{1,0}} &= \left(\frac{2(k+1)(k+d)}{(2k+d+1)(2k+d)}\right)\left(\frac{2k+2+d}{2k+2}\right)\\ &= \frac{1}{2}+o(1).\end{aligned} \tag{4.38}$$

Remark 4.3.3. Generalizing equations (4.36) - (4.38) to $P_k^{(\alpha,\beta)}(t)$ we obtain

$$\frac{\mathrm{d}}{\mathrm{d}t}P_k^{(\alpha,\beta)}(t) = \left(\frac{k^2}{2(\alpha+1)} + o(k^2)\right)P_{k-1}^{(\alpha+1,\beta+1)}(t), \tag{4.39}$$

$$r_k^{(\alpha,\beta)} = O(k^{2\alpha+1}), \text{ and} \tag{4.40}$$

$$m_k^{(\alpha,\beta)} = \frac{1}{2} + o(1). \tag{4.41}$$

We also need the following additional lemmas.

Lemma 4.3.4. *If $P_k(t) = P_k^{(\alpha,\beta)}(t)$ is a sequence of Jacobi Polynomials, $z \in \mathbb{R}$ is fixed such that $\lim_{k\to\infty} P_k(\cos\frac{z}{k}) = c$, and β_k is a sequence satisfying*

$$\lim_{k\to\infty} k\cos^{-1}(\beta_k) = z, \tag{4.42}$$

then

$$\lim_{k\to\infty} P_{k+j}(\beta_k) = c, \tag{4.43}$$

for any fixed $j \in \mathbb{Z}$.

Proof. First, since $\lim_{k\to\infty}(k+j)\cos^{-1}(\beta_k) = \lim_{k\to\infty} k\cos^{-1}(\beta_k)$, by making the substitution $k = k+j$ it suffices to show equation (4.43) for the case $j = 0$. From (4.42), we have that

$$\varepsilon_k := |\beta_k - \cos\frac{z}{k}| = o\left(\frac{1}{k^2}\right).$$

From the mean value theorem, equation (4.39), and using the fact that P_k is uniformly bounded in k on $[-1,1]$ (see for example [44])

$$|P_k(\beta_k) - P_k(\cos\frac{z}{k})| = P_k'(\xi)\varepsilon_k = k^2\tilde{c}P_k^{1,1}(\xi)\varepsilon_k = o(1),$$

for some $\xi \in B(\cos(\frac{z}{k}), \varepsilon_k)$ and $\tilde{c} > 0$. □

We have a stronger version of Lemma 4.3.4 when $c = 0$.

Lemma 4.3.5. *Let $-1 \le \gamma_{k,k} < \cdots < \gamma_{k,1} \le 1$ be the zeros of $P_k(t) = P_k^{(\alpha,\beta)}(t)$, and denote z_i as the i^{th} smallest positive zero of the Bessel function $J_\alpha(z)$. Then for all $i = 1, 2, \ldots$,*

$$\lim_{k\to\infty} kP_{k-1}(\gamma_{k,i}) = 2\Gamma(\alpha+1)\left(\frac{z_i}{2}\right)^{-\alpha+1} J_{\alpha+1}(z_i)$$

Proof. By Corollary 4.3.2,

$$\gamma_{k,i} = 1 - \frac{z_i^2}{2k^2} + o\left(\frac{1}{k^2}\right)$$

which implies

$$\delta_k := |\gamma_{k,i} - \gamma_{k-1,i}| = \frac{z_i^2}{k^3} + o\left(\frac{1}{k^3}\right)$$

By the interlacing properties of the zeros of Jacobi polynomials, we see that $\gamma_{k,i} > \gamma_{k-1,i}$ and we can drop the absolute value in δ_k. Expanding the Taylor series for $P_{k-1}(t)$ around the zero $\gamma_{k-1,i}$, we have

$$kP_{k-1}(\gamma_{k,i}) = k\delta_k P'_{k-1}(\gamma_{k-1,i}) + \frac{k\delta_k^2 P''_{k-1}(\gamma_{k-1,i})}{2} + \cdots$$

Each successive derivative term beyond the first has order $o(1)$ since by repeated application of (4.39) and Lemma 4.3.4, $P_k^{(j)}(t) = O(k^{2j})P_{k-j}^{j,j}(t) = O(k^{2j})$ while on the other hand $\delta_k^j = O(1/k^{3j})$. Thus,

$$kP_{k-1}(\gamma_{k,i}) = \frac{z_i^2}{2(\alpha+1)} P_{k-2}^{1,1}(\gamma_{k-1,i}) + o(1).$$

Now by Theorem 4.3.1 and Lemma 4.3.4, we obtain the result. □

We are now ready to prove the main theorem.

Proof of Theorem 4.1.3. In the case of Riesz energy, we have

$$K_s(x,y) = h_s(\langle x,y\rangle) = (2 - 2\langle x,y\rangle)^{-s/2}$$

We consider the subsequence

$$N_k := D(d,2k) = \binom{d+k}{d} + \binom{d+k-1}{d} = \frac{2}{\Gamma(d+1)}k^d + o(k^d). \tag{4.44}$$

By Theorem 1.2.4 it suffices to prove

$$\lim_{k\to\infty} \frac{\mathcal{E}_s(N_k,\mathbb{S}^d)}{N_k^{1+s/d}} \geq \frac{A_{s,d}}{\mathcal{H}_d(\mathbb{S}^d)^{s/d}} \tag{4.45}$$

where

$$\mathcal{H}_d(\mathbb{S}^d) = \frac{2\pi^{\frac{d+1}{2}}}{\Gamma\left(\frac{d+1}{2}\right)}.$$

Along the subsequence N_k, from (4.22), $\alpha_1 = \gamma_{k,1}^{1,0}$, where $\gamma_{k,i}^{1,0}$ is the i^{th} largest zero of $P_k^{1,0}(t)$ and

$$\begin{aligned}(t-\alpha_1)Q_{k-1}^{1,0}(t,\alpha_1) &= r_{k-1}m_{k-1}(P_k^{1,0}(t)P_{k-1}^{1,0}(\alpha_1) - P_{k-1}^{1,0}(t)P_k^{1,0}(\alpha_1)) \\ &= r_{k-1}m_{k-1}(P_k^{1,0}(t)P_{k-1}^{1,0}(\alpha_1))\end{aligned}$$

and thus the quadrature nodes

$$\alpha_i = \gamma_{k,i}^{1,0}, \qquad i = 1,2,\ldots,k.$$

For a fixed m and all $k \geq m$ we have by Theorem 4.2.7

$$\frac{\mathcal{E}_s(N_k)}{N_k^{1+s/d}} \geq \frac{\sum_{i=1}^k \rho_i h_s(\alpha_i)}{N_k^{-1+s/d}} \geq \frac{\sum_{i=1}^m \rho_i h_s(\alpha_i)}{N_k^{-1+s/d}}.$$

For a fixed $i \leq m$, we have the following asymptotics for $\rho_i h(\alpha_i)$: By Corollary 4.3.2 we have

$$\lim_{k\to\infty}\frac{h_s(\alpha_i)}{k^s}=\lim_{k\to\infty}\frac{(2-2\alpha_i)^{-s/2}}{k^s}=(z_i)^{-s} \tag{4.46}$$

By (4.36) and Lemma 4.3.4,

$$\lim_{k\to\infty}\frac{P_k^{1,0'}(\alpha_i)}{k^2}=\frac{\Gamma(d/2+2)}{d+2}\left(\frac{z_i}{2}\right)^{-\frac{d+2}{2}}J_{d/2+1}(z_i) \tag{4.47}$$

By Lemma 4.3.5,

$$\lim_{k\to\infty}kP_{k-1}^{1,0}(\alpha_i)=2\Gamma(d/2+1)\left(\frac{z_i}{2}\right)^{-\frac{d-2}{2}}J_{d/2+1}(z_i) \tag{4.48}$$

From the weight formula given in equation (4.27) the Cristoffel-Darboux formula (4.25) we have,

$$\lim_{k\to\infty}k^d\rho_i=\lim_{k\to\infty}k^d(\lambda_d(1-\alpha_i)r_{k-1}^{1,0}m_{k-1}^{1,0}P_k^{1,0'}(\alpha_i)P_{k-1}^{1,0}(\alpha_i))^{-1} \tag{4.49}$$

and combining equations, (4.35),(4.37),(4.38),(4.47), and (4.48), this yields

$$\begin{aligned}\lim_{k\to\infty}k^d\rho_i=&\\ \left[\lambda_d\left(\frac{z_i^2}{2}\right)\left(\frac{1}{2^{d-1}\Gamma(d/2+1)^2}\right)\frac{1}{2}\left(\frac{\Gamma(d/2+2)}{d+2}\left(\frac{z_i}{2}\right)^{-d/2-1}J_{d/2+1}(z_i)\right)\right.&\\ \left.\cdot\ 2\Gamma(d/2+1)\left(\frac{z_i}{2}\right)^{-d/2+1}J_{d/2+1}(z_i)\right]^{-1}&\end{aligned} \tag{4.50}$$

Simplifying gives,

$$\lim_{k\to\infty}k^d\rho_i=\frac{2}{\lambda_d z_i^{2-d}\left(J_{d/2+1}(z_i)\right)^2} \tag{4.51}$$

Finally, combining the asymptotics for N_k, $h_s(\alpha_i)$, and ρ_i, equations (4.44), (4.46), and (4.51) respectively, we obtain

$$\lim_{k\to\infty}\frac{\rho_i h(\alpha_i)}{N_k^{s/d-1}} = \frac{2}{\lambda_d\big(\frac{2}{\Gamma(d+1)}\big)^{s/d-1} z_i^{2-d+s}\big(J_{d/2+1}(z_i)\big)^2} \tag{4.52}$$

Thus,

$$\frac{C_{s,d}}{\mathcal{H}_d(\mathbb{S}^d)^{s/d}} = \lim_{k\to\infty}\frac{\mathcal{E}_s(N_k,\mathbb{S}^d)}{N_k^{1+s/d}} \geq \sum_{i=1}^{m}\frac{2}{\lambda_d\big(\frac{2}{\Gamma(d+1)}\big)^{s/d-1} z_i^{2-d+s}\big(J_{d/2+1}(z_i)\big)^2}$$

Multiplying by $\mathcal{H}_d(\mathbb{S}^d)^{s/d}$ and letting $m\to\infty$ gives (4.45) and hence (4.1) □

Proof of Theorem 4.1.4. It is known from number theory [34, Chapter X, Section 7] that $\zeta_{\Lambda_2}(s)$ admits the factorization

$$\zeta_{\Lambda_2}(s) = 6\zeta(s/2)\mathrm{L}_{-3}(s/2), \qquad s>2, \tag{4.53}$$

where

$$\mathrm{L}_{-3}(s) := 1-\frac{1}{2^s}+\frac{1}{4^s}-\frac{1}{5^s}+\frac{1}{7^s}-\cdots, \qquad s>1,$$

is the Dirichlet L-series which is continuous at $s=1$ with $L_{-3}(1)=\pi/3\sqrt{3}$.

We also have asymptotically for the Bessel function [97], as $z\to\infty$,

$$J_2(z) = -\sqrt{\frac{2}{\pi z}}\big(\cos\big(z-\frac{\pi}{4}\big)+O\big(z^{-3/2}\big)\big) \tag{4.54}$$

and z_n the n^{th} zero of the $J_2(z)$ is given by [102]

$$z_n = n\pi+\frac{\pi}{4}+O(n^{-1}). \tag{4.55}$$

Thus for s sufficiently small,

$$\sum_{n=1}^{\infty}\frac{1}{z_n^s J_2(z_n)^2} = \frac{\pi}{2}\sum_{n=1}^{\infty}\frac{1}{z_n^{s-1}+a_n} = \frac{1}{2\pi^{s-2}}\sum_{n=1}^{\infty}\frac{1}{(n+1/4+b_n)^{s-1}+a_n}$$

where $a_n, b_n = o(1)$. As $s\to 2^+$, this sum approaches the Hurwitz-zeta function, $\zeta(s-1,5/4)$

where

$$\zeta(s,q) := \sum_{n=0}^{\infty} \frac{1}{(n+q)^s} \tag{4.56}$$

That is,

$$\lim_{s\to 2^+} \frac{\sum_{n=1}^{\infty}((n+1/4+b_n)^{s-1}+a_n)^{-1}}{\zeta(s-1,5/4)} = 1 \tag{4.57}$$

Indeed, suppose $a = \sup|a_n|$ and $b = \sup|b_n|$. Then,

$$\begin{aligned}
&\sum_{n=1}^{\infty} \frac{1}{(n+1/4+b_n)^{s-1}+a_n} \geq \sum_{n=1}^{\infty} \frac{1}{(n+1/4+b)^{s-1}+a} \\
&\geq \sum_{n=1}^{\infty} \frac{1}{(n+1/4+b+a)^{s-1}} = \sum_{n=0}^{\infty} \frac{1}{(n+5/4+b_n)^{s-1}+a_n} = \zeta(s-1,5/4+a+b),
\end{aligned}$$

and similarly

$$\sum_{n=1}^{\infty} \frac{1}{(n+1/4+b_n)^{s-1}+a_n} \leq \zeta(s-1,5/4-a-b).$$

Thus (4.57) follows since $\zeta(s,q)$ has a simple pole of residue 1 at $s=1$ for all q. Finally,

$$A_{s,2} = 2^s \pi^{s/2} \sum_{n=1}^{\infty} \frac{1}{z_n^s J_2(z_n)^2},$$

and thus we have

$$\lim_{s\to 1^+} \frac{(\sqrt{3}/2)^{s/2}\zeta_{\Lambda_2}(s)}{A_{s,2}} = \lim_{s\to 1^+} \frac{\zeta(s/2)}{2\zeta(s-1,5/4)} = 1.$$

Since $A_{s,d} \leq C_{s,d} \leq (\sqrt{3}/2)^{s/2}\zeta_{\Lambda_2}(s)$, the result follows.

□

Proof of Theorem 4.1.6. For a fixed ρ and a Gaussian potential $f(\|x-y\|) = h(\langle x,y\rangle) = e^{-\alpha(2-2\langle x,y\rangle)}$, let $c := (\rho\beta_d)^{1/d}$ where

$$\beta_d := \frac{(d+1)\pi^{\frac{d+1}{2}}}{\Gamma(1+\frac{d+1}{2})}$$

is the area of $\mathbb{S}^d$, and let

$$f_N(\|x-y\|) = h_N(\langle x,y\rangle) := e^{-\alpha\frac{2-2\langle x,y\rangle}{(cN^{-1/d})^2}}.$$

For each N, h_N is absolutely monotone, and so Theorem 4.2.7 holds. We apply the same asymptotic argument as in the proof of Theorem 4.1.3 to $h_N(t)$. In particular we sample along the subsequence

$$N_k := D(d,2k)$$

where the nodes α_i are given by the zeros of $P_k^{1,0}(t)$. Using the asymptotic formulas for N_k, the quadrature nodes α_i, and the weights ρ_i given by (4.44), Corollary 4.3.2, and (4.51), respectively, we obtain

$$\liminf_{N\to\infty}\frac{\mathcal{E}_{h_N}(N,\mathbb{S}^d)}{N} \geq \frac{4}{\lambda_d\Gamma(d+1)}\sum_{i=1}^{\infty}\frac{z_i^{d-2}}{(J_{d/2+1}(z_i))^2}e^{-\alpha\left(\frac{z_i}{c(2/\Gamma(d+1))^{1/d}}\right)^2}. \tag{4.58}$$

Now fix $r>0$ and consider a spherical cap $\mathcal{D}$ of radius r. Let $\omega_N \subset \mathbb{S}^d$ be an arbitrary sequence of uniformly distributed configurations. That is, the counting measures of ω_N converge in the weak* sense to the normalized surface area measure on $\mathbb{S}^d$. Let r_N be an increasing sequence such that $\lim_{N\to\infty} r_N = r$ and

$$r - r_N = O(N^{-1/2d})$$

Let $\mathcal{D}_{r_N}$ be the cap of radius r_N with the same center as $\mathcal{D}$. For $x\in\mathbb{S}^d$, denote the point energy of x with respect to ω_N by

$$E_{h_N}(x,\omega_N) := \sum_{\substack{x_i\in\omega_N,\\ x_i\neq x}} h_N(\langle x,x_i\rangle).$$

Note that since ω_N is uniformly distributed and the potentials h_N are continuous, $E_{h_N}(x,\omega_N)$

converges uniformly to a constant as $N \to \infty$ and thus

$$\sum_{x_i \in \omega_N \cap \mathcal{D}} E_{h_N}(x_i, \omega_N) = \frac{\#\omega_N \cap \mathcal{D}}{N} E_{h_N}(\omega_N) + o(1).$$

Now,

$$\begin{aligned} \frac{E_{h_N}(\omega_N \cap \mathcal{D})}{\#\omega_N \cap \mathcal{D}} &= \frac{1}{\#\omega_N \cap \mathcal{D}} \left(\sum_{x_i \in \mathcal{D}_{r_N}} E_{h_N}(x_i, \omega_N \cap \mathcal{D}) + \sum_{x_i \in \mathcal{D} \setminus \mathcal{D}_{r_N}} E_{h_N}(x_i, \omega_N \cap \mathcal{D}) \right) \\ &= \frac{1}{\#\omega_N \cap \mathcal{D}} \left(\sum_{x_i \in \mathcal{D}_{r_N}} E_{h_N}(x_i, \omega_N \cap \mathcal{D}) \right) + o(1) \end{aligned} \tag{4.59}$$

Furthermore, for a point $x_i \in \omega_N$, the total contribution to the point energy of charges outside a ball of radius $r - r_N$, denoted $B(x_i, r - r_N)$ is negligible:

$$\begin{aligned} \sum_{x_j \notin B(x_i, r - r_N)} h_N(\langle x_i, x_j \rangle) &\leq \sum_{x_j \notin B(x_i, r - r_N)} f_N(r - r_N) \leq N f_N(r - r_N) \\ &= N e^{-\alpha (\frac{r - r_N}{c N^{-1/d}})^2} \to 0 \end{aligned} \tag{4.60}$$

as $N \to \infty$. Thus,

$$\begin{aligned} \frac{E_{h_N}(\omega_N \cap \mathcal{D})}{\#\omega_N \cap \mathcal{D}} &= \frac{1}{\#\omega_N \cap \mathcal{D}} \left(\sum_{x_i \in \mathcal{D}_{r_N}} \sum_{x_j \in B(x_i, r - r_N)} h_N(\langle x_i, x_j \rangle) \right) + o(1) \\ &= \frac{1}{\#\omega_N \cap \mathcal{D}} \left(\sum_{x_i \in \mathcal{D}_{r_N}} E_{h_N}(x_i, \omega_N) \right) + o(1) \\ &= \frac{E_{h_N}(\omega_N)}{N} + o(1) \end{aligned} \tag{4.61}$$

and so the asymptotic bound in (4.58) holds for $E_{h_N}(\omega_N \cap \mathcal{D}) / \#\omega_N \cap \mathcal{D}$ as $N \to \infty$. Now project $\mathcal{D}$ to its tangent plane and denote by $\widetilde{\omega}_N$ the resulting planar configuration. Then

$$\frac{E_{h_N}(\widetilde{\omega}_N)}{\#\omega_N \cap \mathcal{D}} = \frac{E_{h_N}(\omega_N \cap \mathcal{D})}{\#\omega_N \cap \mathcal{D}} + \varepsilon_r$$

for some ε_r which goes to 0 as $r \to 0$. Now scale $\widetilde{\omega}_N$ by $N^{1/d}/c$ to obtain a configuration

$\mathcal{C}_N$ such that

$$\frac{\#\mathcal{C}_N \cap B(rN^{1/d}/c)}{\mathrm{Vol}(B(rN^{1/d}/c))} = \frac{\#\omega_N \cap \mathcal{D}}{\mathrm{Vol}(B(rN^{1/d}/c))} = \frac{N\mathrm{Vol}(B(r))}{\beta_d \mathrm{Vol}(B(rN^{1/d}/c))} = \frac{c^d}{\beta_d} = \rho$$

and

$$\frac{E_f(\mathcal{C}_N)}{\#\omega_N \cap \mathcal{D}} = \frac{E_{h_N}(\omega_N \cap \mathcal{D})}{\#\omega_N \cap \mathcal{D}} + \varepsilon_r \tag{4.62}$$

Now for any infinite configuration $\mathcal{C} \subset \mathbb{R}^d$ of density ρ whose energy is well defined, and for a fixed N, we can find a configuration $\omega_N \subset \mathbb{S}^d$ such that under inverse scaling and mapping from the tangent plane, $\mathcal{C} \cap B(rN^{1/d}/c)$ is mapped to $\omega_N \cap \mathcal{D}$. Thus,

$$\begin{aligned} E_f(\mathcal{C}) &\geq \liminf_{N\to\infty} \frac{E_{h_N}(\omega_N)}{N} + \varepsilon_r \\ &\geq \frac{4}{\lambda_d \Gamma(d+1)} \sum_{i=1}^{\infty} \frac{z_i^{d-2}}{(J_{d/2+1}(z_i))^2} e^{-\alpha\left(\frac{z_i}{c(2/\Gamma(d+1))^{1/d}}\right)^2} + \varepsilon_r. \end{aligned} \tag{4.63}$$

We now note that $r > 0$ was arbitrary, and that if R is such that $\mathrm{vol}(B(R/2)) = \rho$, then

$$\pi R = c\left(\frac{2}{\Gamma(d+1)}\right)^{1/d}$$

and (4.5) is obtained. □

4.4 Numerics

Translated into packing density and using 4.3.2, Corollary 4.2.10 provides an alternate proof of Levenshtein's second best packing bound [66]:

Corollary 4.4.1.

$$\Delta_d \leq \frac{z_1^d}{\Gamma(d/2+1)4^d} =: L_d$$

As $s \to \infty$, the series in $A_{s,d}$ is dominated by the first term z_1^{-s} and using the asymptotics of $C_{s,d}$ in (1.16), we see that

$$\lim_{s\to\infty}\left[\frac{C_{s,d}}{A_{s,d}}\right]^{1/s} = \left[\frac{L_d}{\Delta_d}\right]^{1/d} =: B_d \geq 1 \tag{4.64}$$

The following table shows the values of B_d in dimensions $d = 1,2,3,8$, and 24 where Δ_d is known precisely. For $d = 4,5,6,7$ where Δ_d is conjectured to be given by lattice packings, the table provides an upper bound for B_d.

Table 4.1: Upper Bounds on B_d

d	B_d
1	1
2	1.00589479
3	1.02703993
4	1.02440844
5	1.03861371
6	1.03461793
7	1.03156355
8	1.01742074
24	1.02403055

For $d = 2,4,8$, and 24, where $\widetilde{C}_{s,d}$ is given in Conjecture 1.3.2 we plot

$$f(s) := \left[\frac{\widetilde{C}_{s,d}}{A_{s,d}}\right]^{1/s}.$$

The Epstein-Zeta functions for the D_4, E_8, and Leech lattices are calculated using known formulas for the theta functions (see [36, Ch. 4])

$$\Theta_\Lambda(z) = \sum_{x\in\Lambda} e^{i\pi z\|x\|^2} \qquad \operatorname{Im} z > 0.$$

Since these three lattices have vectors whose squared norms are even integers, we let $q = e^{i\pi z}$

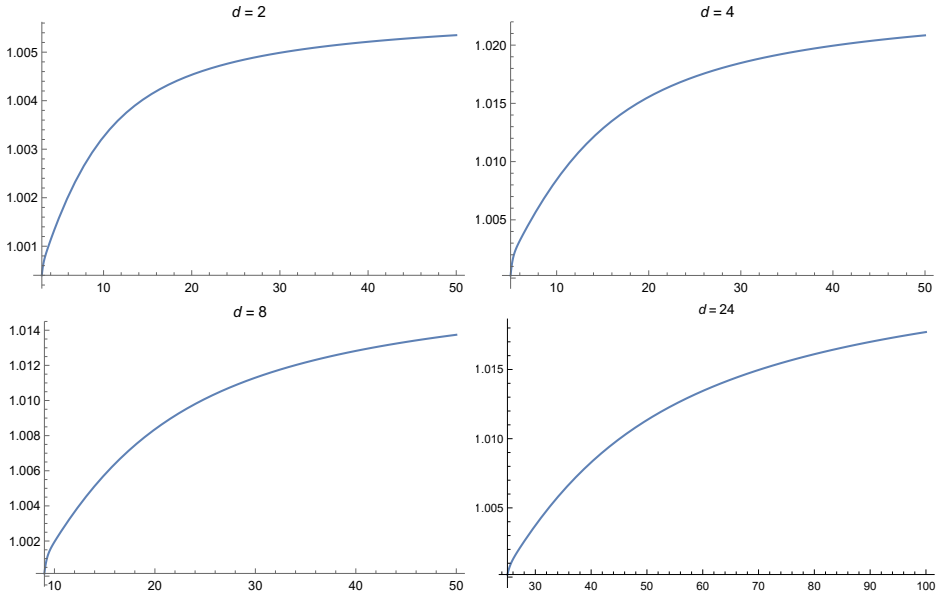

Figure 4.1: Graphs of $f(s) = (\widetilde{C}_{s,d}/A_{s,d})^{1/s}$ for $d = 2, 4, 8$ and 24.

and write

$$\Theta_{\Lambda_d}(z) = \sum_{m=1}^{\infty} N_d(m) q^{2m}$$

where $N_d(m)$ counts the number of vectors in Λ_d, $d = 4, 8, 24$ of squared norm $2m$. Thus the Epstein-Zeta function

$$\zeta_{\Lambda_d}(s) = \sum_{m=1}^{\infty} \frac{N_d(m)}{(2m)^{s/2}}.$$

For the D_4 lattice, a classical result from number theory gives

$$N_4(m) = 24 \sum_{\substack{d|2m, \\ d \text{ odd}}} d.$$

For the E_8 lattice, we have

$$N_8(m) = 240\sigma_3(m)$$

where

$$\sigma_k(m) = \sum_{d|m} d^k$$

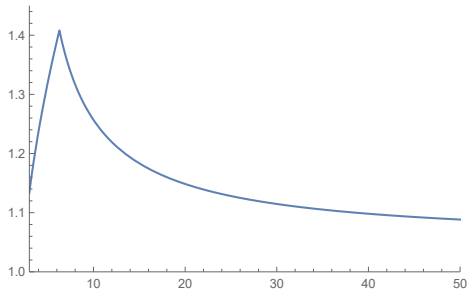

Figure 4.2: Graph of $g(s) = (\widetilde{C}_{s,d}/\max\{\Theta_{s,d}, \xi_{s,d}\})^{1/s}$ for $d = 2$, $3 \leq s \leq 50$.

is the divisor function. Finally for the Leech lattice, it is known that

$$N_{24}(m) = \frac{65520}{691}(\sigma_{11}(m) - \tau(m))$$

where $\tau(m)$ is the Ramanujan tau function defined in [82].

Figure 4.1 plots $f(s)$ for $d = 2, 4, 8$ and 24. In these dimensions the graphs monotonically increase to the limit B_d as $s \to \infty$ and decrease to 1 as $s \to d^+$, demonstrating Theorem 4.1.4 for $d = 2$, and suggesting that $A_{s,d}$ also gives a tight bound as $s \to d^+$ for $d = 4, 8$, and 24. However, as $s \to d^+$, both $\widetilde{C}_{s,d}$ and $A_{s,d}$ approach ∞, so precise numerical calculations are sensitive to the number of terms taken in each sum. Ten thousand terms were used in the sum for the plots, but more precise calculations are needed.

We also show a corresponding graph for the bounds $\Theta_{s,d}$ and $\xi_{s,d}$ from Propositions 4.1.1 and 4.1.2. As $s \to d^+$, $\Theta_{s,d} \nrightarrow \infty$, so $\xi_{s,d}$ is clearly a better bound for s near d. On the other hand, as $s \to \infty$, it is straightforward to show that $\xi_{s,d} \to 0$, so $\Theta_{s,d} > \xi_{s,d}$ for large s. Figure 4.2 plots

$$g(s) := \left[\frac{\widetilde{C}_{s,d}}{\max\{\Theta_{s,d}, \xi_{s,d}\}}\right]^{1/s}$$

for $d = 2$. As $s \to \infty$, $g(s) \searrow 1.0501...$, as $s \to d^+$, it is possible that $g(s) \to 1$, but it converges slower than $f(s)$. Again, in this range, the exact values are sensitive to the number of terms taken in $\widetilde{C}_{s,d}$ and more precision is needed. The cusp at $s \approx 6.2789...$ is where $\Theta_{s,d}$ and $\xi_{s,d}$ switch.

Given Theorem 4.1.4 and Figure 4.1, we have the following natural conjecture.

Conjecture 4.4.2. *For $d = 4, 8,$ and 24,*

$$\lim_{s \to d^+} \frac{|\Lambda_d|^{s/d} \zeta_{\Lambda_d}(s)}{C_{s,d}} = 1. \tag{4.65}$$

where $\Lambda_4 = D_4$, $\Lambda_8 = E_8$, and Λ_{24} is the Leech lattice.

A proof of Conjecture 4.4.2 would follow from an appropriate factoring of $\zeta_{\Lambda_d}(s)$ analogous to (4.53) for $d = 2$.

In high dimensions, lattice packings are no longer optimal and less is known or conjectured about $C_{s,d}$. As $d \to \infty$, the Levenshtein packing bound from Corollary 4.4.1 becomes

$$\Delta_d \leq 2^{-0.5573d} \tag{4.66}$$

and thus

$$B_d = O\left(\frac{2^{-0.5573}}{\Delta_d^{1/d}}\right).$$

BIBLIOGRAPHY

[1] C. Aistleitner, J.S. Brauchart, and J. Dick. Point sets on the sphere $\mathbb{S}^2$ with small spherical cap discrepancy. *Discrete Comput. Geom.*, 48(4):990–1024, 2012.

[2] C. Amante and B. W. Eakins. ETOPO1 1 Arc-Minute Global Relief Model: Procedures, Data Sources and Analysis, 2009.

[3] Richard Askey. *Orthogonal polynomials and special functions*. SIAM, Philadelphia, Pennsylvania., 1975.

[4] R. Bauer. Distribution of points on a sphere with application to star catalogs. *J. Guid. Cont. Dyn.*, 23(1):130–137, 2000.

[5] J. Beck. Sums of distances between points on a sphere-an application of the theory of irregularities of distribution to discrete geometry. *Mathematika*, 31(1):33–41, 1984.

[6] R. Berman, S. Boucksom, and D. Nystrom. Fekete points and convergence towards equilibrium measures on complex manifolds. *Acta Math.*, 207(1):1–27, 2011.

[7] L. Bétermin and E. Sandier. Renormalized energy and asymptotic expansion of optimal logarithmic energy on the sphere. To appear, ArXiv preprint: http://arxiv.org/abs/1404.4485.

[8] D. Bilyk. The L^2 discrepancy of irrational lattices. In *Monte Carlo and Quasi-Monte Carlo Methods 2012*, pages 289–296. Springer, 2013.

[9] D. Bilyk, V. N. Temlyakov, and R. Yu. The L^2 Discrepancy of Two-Dimensional Lattices. In *Springer Proc. Math. Stat.*, volume 25, pages 63–77. 2012.

[10] D. Bilyk, V.N. Temlyakov, and R. Yu. Fibonacci sets and symmetrization in discrepancy theory. *J. Complexity*, 28(1):18–36, 2013.

[11] A. Bondarenko, D. Radchenko, and M. Viazovska. Well separated spherical designs. *Constructive Approximation*, 41(1):93–112, 2014.

[12] A.V. Bondarenko, D.P. Hardin, and E.B. Saff. Mesh ratios for best-packing and limits of minimal energy configurations. *Acta Math. Hungar.*, 142(1):118–131, 2012.

[13] S.V. Boradachov, D.P. Hardin, and E.B. Saff. *Minimal discrete energy on rectifiable sets*. Springer, to appear.

[14] S. V. Borodachov, D. P. Hardin, and E. B. Saff. Asymptotics of best-packing on rectifiable sets. *Proc. Amer. Math. Soc.*, 135(8):2369–2380, 2007.

[15] S. V. Borodachov, D. P. Hardin, and E. B. Saff. Asymptotics for discrete weighted minimal Riesz energy problems on rectifiable sets. *Trans. Amer. Math. Soc.*, 360(3):1559–1580, 2008.

[16] S. V. Borodachov, D. P. Hardin, and E. B. Saff. Low Complexity Methods For Discretizing Manifolds Via Riesz Energy Minimization. *Found. Comput. Math.*, 14(6):1173–1208, 2014.

[17] S. Boumova. *Applications of polynomials to spherical codes and designs*. PhD thesis, Eindhoven University of Technology, 2002.

[18] M.J. Bowick, A. Cacciuto, D.R. Nelson, and A. Travesset. Crystalline order on a sphere and the generalized Thomson problem. *Phys. Rev. Lett.*, 89, 2002.

[19] M.J. Bowick and L. Giomi. Two-dimensional matter: Order, curvature and defects. *Adv. Phys.*, 58:449–563, 2009.

[20] P. Boyvalenkov, P. Dragnev, D. P. Hardin, E. B. Saff, and M. Stoyanova. Universal lower bounds for potential energy of spherical codes. *Contr. Approx.*, 44(3):385–415, 2016.

[21] J. S. Brauchart, D. P. Hardin, and E. B. Saff. The next-order term for optimal Riesz and logarithmic energy asymptotics on the sphere. In *Recent advances in orthogonal polynomials, special functions, and their applications*, volume 578 of *Contemp. Math.*, pages 31–61. Amer. Math. Soc., Providence, RI, 2012.

[22] J. S. Brauchart, A. B. Reznikov, E. B. Saff, I. H. Sloan, Y. G. Wang, and R. S. Womersley. Random point sets on the sphere—hole radii, covering, and separation. *Experimental Mathematics*, pages 1–20, 2016.

[23] J.S. Brauchart, J. Dick, and L. Fang. Spatial low discrepancy sequences, spherical cone discrepancy, and applications in financial modeling. *J. Comput. Appl. Math.*, 286:28–53, 2015.

[24] J.S. Brauchart, E.B. Saff, I.H. Sloan, Y.G. Wang, and R.S. Womersley. Random point sets on the sphere – hole radii, covering, and separation. *Experimental Math.*, To appear.

[25] D. Broomhead, D. S. and Lowe. Multivariable Functional Interpolation and Adaptive Networks. *Complex Syst.*, 2:321– 355, 1988.

[26] R. E. Caflisch. Monte Carlo and quasi-Monte Carlo methods. *Acta Numerica*, 7:1, 1998.

[27] M. Calef. *Theoretical and computational investigations of minimal energy problems*. PhD thesis, Vanderbilt University, 2009.

[28] D.L.D. Caspar and A. Klug. Physical principles in the construction of regular viruses. *Cold Springs Harb. Symp. Quant. Biol.*, 27, 1962.

[29] C. Chang and C. Lin. LIBSVM. *ACM Trans. Intell. Syst. Technol.*, 2(3):1–27, 2011.

[30] Clawpack Development Team. Clawpack software, 2017. Version 5.4.0.

[31] H. Cohn and M. De Courcy-Ireland. The gaussian core model in high dimensions. Preprint, ArXiv: 1603.09684.

[32] H. Cohn and N. Elkies. New upper bounds on sphere packings. I. *Ann. of Math. (2)*, 157(2):689–714, 2003.

[33] H. Cohn, A. Kumar, S. Miller, D. Radchecnko, and M. Viazovska. The sphere packing problem in dimension 24. Preprint, arXiv:1603.06518.

[34] Harvey Cohn. *Advanced number theory*. Dover Publications, Inc., New York, 1980. Reprint of ıt A second course in number theory, 1962, Dover Books on Advanced Mathematics.

[35] Henry Cohn and Abhinav Kumar. Universally optimal distribution of points on spheres. *J. Amer. Math. Soc.*, 20(1):99–148, 2007.

[36] J. H. Conway and N. J. A. Sloane. *Sphere packings, lattices and groups*, volume 290 of *Grundlehren der Mathematischen Wissenschaften [Fundamental Principles of Mathematical Sciences]*. Springer-Verlag, New York, third edition, 1999. With additional contributions by E. Bannai, R. E. Borcherds, J. Leech, S. P. Norton, A. M. Odlyzko, R. A. Parker, L. Queen and B. B. Venkov.

[37] H.S.M Coxeter. The role of intermediate convergents in Tait's explanation for phyllotaxis. *J Algebra*, 20:167–175, 1972.

[38] J. Cui and W. Freeden. Equidistribution on the sphere. *SIAM J. Sci. Comput.*, 18(2):595–609, 1997.

[39] B. Dahlberg. On the distribution of Fekete points. *Duke Math. J.*, 45(3):537–542, 1978.

[40] P. Delsarte. Bounds for unrestricted codes, by linear programming. *Philips Res. Rep.*, 27:272–289, 1972.

[41] P. Delsarte, J. M. Goethals, and J. J. Seidel. Spherical codes and designs. *Geom. Dedicata*, 6(3):363–388, 1977.

[42] R. Dixon. Spiral phyllotaxis. *Comput. Math. Appl.*, 17:535–538, 1992.

[43] P.D. Dragnev. On the separation of logarithmic points on the sphere. In *Approx. Theory X*, pages 137–144. Vanderbilt University Press, Nashville, TN, 2002.

[44] T. Erdelyi, A. P. Magnus, and P. Nevai. Generalized Jacobi weights, Cristoffel functions, and Jacobi polynomials. *SIAM J. Math. Anal.*, 25:602–614, 1994.

[45] L. Fejes. über die dichteste Kugellagerung. *Math. Z.*, 48:676–684, 1943.

[46] B. Fornberg. *A practical guide to pseudospectral methods*. Cambridge University Press, 1996.

[47] B. Fornberg and N. Flyer. *A Primer on Radial Basis Functions with Applications to the Geosciences*. Society for Industrial and Applied Mathematics, Philadelphia, PA, 2015.

[48] B. Fornberg and N. Flyer. Fast generation of 2-D node distributions for mesh-free PDE discretizations. *Comput. Math. Appl.*, 69(7):531–544, 2015.

[49] B. Fornberg and N. Flyer. Solving PDEs with radial basis functions. *Acta Numerica*, 24:215–258, 2015.

[50] E.J. Fuselier and G.B. Wright. Stability and error estimates for vector field interpolation and decomposition on the sphere with RBFs. *SIAM J. Numer. Anal.*, 47(5):3213–39, 2009.

[51] F.X. Giraldo, J.S. Hesthave, and T. Warburton. Nodal high-order discontinuous galerkin methods for the spherical shallow water equations. *J. Comput. Phys.*, 181(2):499–525, 2002.

[52] M. Goldberg. A class of multi-symmetric polyhedron. *Tohoku Math. J.*, 43:104–108, 1937.

[53] K.M. Gorski, E. Hivon, A.J. Banday, B.D. Wandelt, F.K. Hansen, M. Reinecke, and M. Bartelman. HEALPix-a framework for high resolution discretization, and fast analysis of data distributed on the sphere. *Astophys. J.*, 622:759–771, 2005.

[54] Thomas Hales, Mark Adams, Gertrud Bauer, Tat Dat Dang, John Harrison, Le Truong Hoang, Cezary Kaliszyk, Victor Magron, Sean Mclaughlin, Tat Thang Nguyen, and et al. A Formal proof of the Kepler conjecture. *Forum Math. Pi*, 5:e2, 29, 2017.

[55] D. P. Hardin and E. B. Saff. Minimal Riesz Energy Point Configurations for Rectifiable d-Dimensional Manifolds. *Adv. Math.*, 193(1):174–204, 2003.

[56] D.P. Hardin, T. Michaels, and E.B. Saff. A comparison of popular point configurations on $\mathbb{S}^2$. *Dolomites Res. Notes Approx.*, 9:16–49, 2016.

[57] D.P. Hardin and E.B. Saff. Minimal riesz energy point configurations for rectifiable d-dimensional manifolds. *Adv. Math.*, 193(1):174–204, 2005.

[58] A. Holhoş and D. Roşca. An octahedral equal area partition of the sphere and near optimal configurations of points. *Comput. Math. Appl.*, 67:1092–1107, 2014.

[59] A. Holhoş and D. Roşca. Area preserving maps and volume preserving maps between a class of polyhedrons and a sphere. *Adv. Comp. Math.*, 43(4):677–697, 2017.

[60] A. A. Kolpakov, A. D. Mednykh, and M. G. Pashkevich. A volume formula for the $\mathbb{Z}_2$-symmetric spherical tetrahedron. *Sibirsk. Mat. Zh.*, 52(3):582–599, 2011.

[61] L. Kuipers and H. Niederreiter. *Uniform distribution of sequences*. Dover Publications, Mineola, N.Y, 2006.

[62] C. Lemieux. *Monte Carlo and Quasi-Monte Carlo Sampling*. Springer Series in Statistics. Springer New York, New York, NY, 2009.

[63] P. Leopardi. A partition of the unit sphere into regions of equal area and small diameter. *Electron. Trans. on Numer. Anal.*, 25:309–327, 2006.

[64] P. Leopardi. Diameter bounds for equal area partitions of the unit sphere. *Electron. Trans. Numer. Anal.*, 35:1–16, 2009.

[65] P. Leopardi. Discrepancy, separation, and Riesz energy of finite point sets on the unit sphere. *Adv. Comput. Math.*, 39(1):27–43, 2013.

[66] V. I. Levenshtein. Bounds for packings in n-dimensional euclidean space. *Soviet Math. Dokl.*, 20:417–421, 1979.

[67] V. I. Levenshtein. Designs as maximum codes in polynomial metric spaces. *Acta Appl. Math.*, 29(1-2):1–82, 1992.

[68] V. I. Levenshtein. Universal bounds for codes and designs. *Chapter 6 in Handbook of Coding Theory, Eds. V.Pless and W.C.Huffman, Elsevier Science B.V.*, pages 499–648, 1998.

[69] W. LeVeque. *Topics in Number Theory, Volume 2*. Addison-Wesley, Reading, Massachusetts, 1956.

[70] G. Marsaglia. Random numbers fall mainly in the planes. *Proc. Natl. Acad. Sci.*, 61(1):25–28, 1968.

[71] A. Martínez-Finkelshtein, V. Maymeskul, E. A. Rakhmanov, and E. B. Saff. Asymptotics for minimal discrete Riesz energy on curves in $\mathbb{R}^d$. *Canad. J. Math.*, 56(3):529–552, 2004.

[72] H.M. Mhaskar, F.J. Narcowich, J. Prestin, and J.D. Ward. l^p Bernstein estimates and approximation by spherical basis functions. *Math. Comp.*, 79(271):1647–49, 2010.

[73] T. Michaels. Equidistributed icosahedral configurations on $\mathbb{S}^2$. *Comput. Math. Appl.*, 74(4):605–612, 2017.

[74] J. J. Monaghan. Why particle methods work. *SIAM J. Sci. Statist. Comput.*, 3(4):422–433, 1982.

[75] C. Müller. *Spherical harmonics*, volume 17 of *Lecture Notes in Mathematics*. Springer-Verlag, Berlin-New York, 1966.

[76] R.D. Nair, S.J. Thomas, and R.D. Loft. A discontinuous galerkin transport scheme on the cubed sphere. *Mon. Weather Rev.*, 135:814–828, 2005.

[77] H. Niederreiter. *Random number generation and quasi-Monte Carlo methods*. Soc. Ind. Appl. Math., Philadelphia, Pennsylvania, 1992.

[78] A. Okabe, B. Boots, K. Sugihara, and S.N. Chiu. *Spatial tessellations: concepts and applications of Voronoi diagrams*. Wiley, Chichester, 1992.

[79] O.Vlasiuk, T. Michaels, N. Flyer, and B. Fornberg. Fast high-dimensional node generation with variable density. In preparation.

[80] F. P. Preparata and M. I. Shamos. *Computational Geometry*. Springer New York, 1985.

[81] E.A. Rakhmanov, E.B. Saff, and Y.M. Zhou. Minimal discrete energy on the sphere. *Math. Res. Lett.*, 1:647–662, 1994.

[82] S. Ramanujan. On certain arithmetical functions [Trans. Cambridge Philos. Soc. **22** (1916), no. 9, 159–184]. In *Collected papers of Srinivasa Ramanujan*, pages 136–162. AMS Chelsea Publ., Providence, RI, 2000.

[83] M. Reimer. Quadrature rules for the surface integral of the unit sphere based on extremal fundamental systems. *Math. Nachr.*, 169:235–241, 1994.

[84] M. Reimer. Spherical polynomial approximation: a survey. In *Adv. Multivar. Aprox.*, pages 231–252. Wiley, Berlin, 1999.

[85] A. Reznikov and E.B. Saff. The covering radius of randomly distributed points on a manifold. *Internat. Math. Res. Notices*, To appear.

[86] W.M. Schmidt. Irregularities of distribution VI. *Compos. Math.*, 24:63–74, 1972.

[87] V. Shankar, G. B. Wright, R. M. Kirby, and A. L. Fogelson. A radial basis function (RBF)-finite difference (FD) method for diffusion and reaction–diffusion equations on surfaces. *Journal of Scientific Computing*, 63(3):745–768, 2014.

[88] Claude E. Shannon. Probability of error for optimal codes in a Gaussian channel. *Bell System Tech. J.*, 38:611–656, 1959.

[89] I.H. Sloan and R.S. Womersley. Extremal systems of points and numerical integration on the sphere. *Adv. Comput. Math.*, 21:107–125, 2004.

[90] S. Smale. Mathematical problems for the next century. *Math. Intelligencer*, 20:7–15, Spring 1998.

[91] J.P. Snyder. An equal-area map projection for polyhedral globes. *Cartographica*, 29(1):10–21, 1992.

[92] J.P. Snyder. *Flattening the Earth*. University of Chicago Press, Chicago, 1993.

[93] L. Song, A.J. Kimerling, and K. Sahr. Developing an equal area global grid by small circle subdivision. In M. Goodchild and A.J. Kimerling, editors, *Discrete global grids: a web book*. University of California, Santa Barbera, 2002.

[94] I. Soprounov. A short proof of the prime number theorem for arithmetic progressions, available online at http://www.math.umass.edu/ isoprou/pdf/primes.pdf.

[95] S.L. Svensson. Finite elements on the sphere. *J. Approx. Theory*, 40:246–260, 1984.

[96] R. Swinbank and R.J. Purser. Fibonacci grids: A novel approach to global modeling. *Roy. Meteorol. Soc.*, 132(619):1769–1793, 2006.

[97] G. Szegő. *Orthogonal polynomials*. American Mathematical Society, Providence, R.I., fourth edition, 1975. American Mathematical Society, Colloquium Publications, Vol. XXIII.

[98] N.A. Teanby. An icosahedron-based method for even binning of globally distributed remote sensing data. *Comput. Geosci.*, 32:1442–1450, 2006.

[99] M. Tegmark. An icosahedron-based method for pixelizing the celestial sphere. *Astrophys. J.*, 470:L81–L84, 1996.

[100] J.J. Thomson. On the structure of the atom: an investigation of the stability and periods of oscillation of a number of corpuscles arranged at equal intervals around the circumference of a circle; with application of the results to the theory of atomic structure. *Philos. Mag. Ser.*, 7(39):237–265, 1904.

[101] M. Viazovska. The sphere packing problem in dimension 8. Preprint, arXiv:1603.04246.

[102] G. N. Watson. *A treatise on the theory of Bessel functions*. Cambridge Mathematical Library. Cambridge University Press, Cambridge, 1995. Reprint of the second (1944) edition.

[103] H. Wendland. *Scattered Data Approximation*. Cambridge University Press, 2004.

[104] T.T. Wong, W.S. Luk, and P.A. Heng. Sampling with Hammersley and Halton points. *J. Graph. Tools*, 2(2):9–24, 1997.

[105] G. Wright. Notes/grids/meshes on the sphere. Unpublished notes.

[106] V. A. Yudin. Minimum potential energy of a point system of charges. *Diskret. Mat.*, 4(2):115–121, 1992.

[107] Y.M. Zhou. *Arrangements of points on the sphere*. PhD thesis, University of South Florida, 1995.